



HAL
open science

Structural controls and metallogenic model of polyphase uranium mineralization in the Kiggavik area (Nunavut, Canada)

Alexis Grare, Antonio Benedicto, Julien Mercadier, Olivier Lacombe, Anna Trave, Marie Guilcher, Antonin Richard, Patrick Ledru, Mario Blain, John Robbins, et al.

► To cite this version:

Alexis Grare, Antonio Benedicto, Julien Mercadier, Olivier Lacombe, Anna Trave, et al.. Structural controls and metallogenic model of polyphase uranium mineralization in the Kiggavik area (Nunavut, Canada). *Mineralium Deposita*, 2021, 56, pp.1263-1296. 10.1007/s00126-020-00957-x . hal-02911793

HAL Id: hal-02911793

<https://brgm.hal.science/hal-02911793>

Submitted on 29 Feb 2024

HAL is a multi-disciplinary open access archive for the deposit and dissemination of scientific research documents, whether they are published or not. The documents may come from teaching and research institutions in France or abroad, or from public or private research centers.

L'archive ouverte pluridisciplinaire **HAL**, est destinée au dépôt et à la diffusion de documents scientifiques de niveau recherche, publiés ou non, émanant des établissements d'enseignement et de recherche français ou étrangers, des laboratoires publics ou privés.

Mineralium Deposita

Structural controls and metallogenic model of polyphase uranium mineralization in the Kiggavik area (Nunavut, Canada)

--Manuscript Draft--

Manuscript Number:	
Full Title:	Structural controls and metallogenic model of polyphase uranium mineralization in the Kiggavik area (Nunavut, Canada)
Article Type:	Regular Articles
Corresponding Author:	Alexis Grare, Ph.D Sorbonne Universite Paris, FRANCE
Corresponding Author Secondary Information:	
Corresponding Author's Institution:	Sorbonne Universite
Corresponding Author's Secondary Institution:	
First Author:	Alexis Grare, Ph.D
First Author Secondary Information:	
Order of Authors:	Alexis Grare, Ph.D Antonio Benedicto Julien Mercadier Olivier Lacombe Anna Trave Marie Guilcher Antonin Richard Patrick Ledru Mario Blain John Robbins Philippe Lach
Order of Authors Secondary Information:	
Funding Information:	
Abstract:	<p>The Kiggavik area is located on the eastern border of the Paleo- to Mesoproterozoic Thelon Basin (Nunavut, Canada) and hosts major uranium mineralization in Archean basement rocks. These mineralizations display a strong structural control and share many similarities with the world-class unconformity-related U deposits of the coeval Athabasca Basin (Saskatchewan, Canada). An innovative cross-disciplinary study combining macro- to micro-scale characterization was applied to define the uranium mineral system in the Kiggavik area: observation, characterization and measurement of fractures in the field and from drillcores, petrographic and cathodoluminescence identification of fracture cements, analysis of fluid inclusions, and analysis of uranium oxides and related mineral phases through SEM, LA ICP-MS and SIMS. The analysis of fluid inclusions coupled with oriented measurements of fluid inclusions planes they constitute allow allows to link fluid circulation to a tectonic stress and therefore to bridge the gap between the micro and the macro-scales. Our results show that the first order fault/fracture network in the Kiggavik area is mainly oriented ENE-WSW and NE-SW and consists of polyphased fault zones initiated during the Thelon and Trans-Hudsonian orogenies (ca. 1900-1800 Ma). These faults were subsequently U mineralized in four stages referred to as U0, U1, U2 and U3. These different U stages,</p>

	<p>yield distinctive fracture, alteration and mineralization patterns, indicating different conditions of formation. U0, inferred to be of magmatic-volcanic origin, likely occurred at ca. 1830 Ma and is related to micro-brecciation and weak clay-alteration under a WSW-ENE compressional stress. This event predates intense quartz brecciation, iron oxidation and veining at ca. 1750 Ma. This silicifying event, called Quartz Breccia (QB), predates the deposition of the Thelon Basin and is of magmatic-epithermal origin, associated with anorogenic rifting and emplacement of the Kivalliq igneous suite. Circulation of Si-bearing magmatic derived fluids caused pervasive silicification of former fault zones, which in turn controlled subsequent fracture development and behaved as barriers for later U mineralizing fluids (U1 to U3). Both the U0 mineralization and the subsequent QB silicifying event reflect the importance of pre-Thelon Basin fracturing and fluid circulation events in controlling the development and location of later U mineralizing stages. U1, U2 and U3 postdate deposition of the Thelon Basin. U1 is characterized by polymetallic mineralization in reduced narrow fault zones and U2 is characterized by monometallic mineralization in oxidized wider fault zones. These two mineralization episodes are characterized by illite and sudoite crystallization and occurred under a regional strike-slip stress regime, with the direction of σ_1 evolving from WNW-ESE (U1) to NE-SW /ENE-WSW (U2); both formed between ~1500-1330 Ma and are related to circulations of Thelon-derived U-bearing basinal brines similar to the mineralizing brines at the origin of the 1600-1270 Ma unconformity-related U deposits in the Athabasca Basin. A post U2, but pre-Mackenzie dikes, NE-SW extensional stress caused normal-dextral offset of the orebodies by reactivating NNW-SSE and E-W faults. This fracturing event triggered circulation of hot (~300°C), probably acidic fluids, dequartzifying, illitizing and bleaching the host-rock. U3 is a redistribution/reconcentration of the previous U mineralization along redox fronts, postdating MacKenzie dike (ca. 1270 Ma) and occurred through weak reopening of the pre-existing fracture network enhancing percolation of low temperature meteoric fluids during two main events at ca. 550 and 350 Ma.</p> <p>Our study shows that U deposits and prospects in the Kiggavik area are of mixed type: a pre-basin magmatic-volcanic U stock (U0) remobilized by post-basin basinal brines to form unconformity-related mineralization (U1 and U2), which were lately altered and remobilized by massive percolations of meteoric waters (U3). This zone demonstrates thus a mobility of U during more than 1.5 billion years and had an evolution similar to that of the world-class U district of the Athabasca Basin. A significant difference with the Athabasca Basin is however that the strongest clay alteration event, formed by illite and linked to the MacKenzie dike intrusions, postdates the main stages of mineralization (U0 to U2).</p>
<p>Suggested Reviewers:</p>	<p>Eric Potter, Doctor Research scientist, Geological survey of canada, Ottawa eric.potter@canada.ca His research interest is focused on the formation of uranium-bearing ore deposits in Canada</p> <p>Charlie Jefferson Section Head, Research Scientist, Natural Resources Canada charlie.jefferson@canada.ca Charlie Jefferson is interested about mineral resources system and spent a lot of time working on the Kiggavik area and around the Thelon basin dealing with cartographic, structural and geochemical data.</p> <p>Guoxiang Chi, Professor University of Regina guoxiang.chi@uregina.ca His research interest is focused on Mineral Deposits Geology and Geochemistry. He is specifically specialised on fluid inclusions and he worked on the Kiggavik area.</p>

1 **STRUCTURAL CONTROLS AND METALLOGENIC MODEL OF**
2 **POLYPHASE URANIUM MINERALIZATION IN THE KIGGAVIK AREA**
3 **(NUNAVUT, CANADA)**

4
5 **Alexis Grare^{a,b}, Antonio Benedicto^c, Julien Mercadier^d, Olivier Lacombe^a, Anna Trave^e, Marie**
6 **Guilcher^d, Antonin Richard^d, Patrick Ledru^b, Mario Blain^b, John Robbins^b, Philippe Lach^f**

7 ^a Sorbonne Université, CNRS-INSU, Institut des Sciences de la Terre de Paris, IStEP UMR 7193, F-
8 75005 Paris, France

9 ^b AREVA Resources Canada Inc. 817-45th St West Saskatoon. SK S7L 5X2. Canada

10 ^c Université Paris Sud, UMR GEOPS, 91405 Orsay. France

11 ^d Université de Lorraine, CNRS, CREGU, GeoRessources lab, Campus Aiguillettes, Faculté des Sciences
12 et Technologies, rue Jacques Callot, Vandoeuvre-lès-Nancy, 54506 France

13 ^e Universitat de Barcelona, Departament de Mineralogia, Petrologia i Geologia Aplicada, Facultat de
14 Ciències de la Terra. 08028 Barcelona. Spain

15 ^f BRGM French Geological Survey, 3 avenue Claude Guillemin, BP 36009, 45060 Orléans Cedex 2, France

16

17 **Abstract**

18 The Kiggavik area is located on the eastern border of the Paleo- to Mesoproterozoic Thelon Basin (Nunavut,
19 Canada) and hosts major uranium mineralization in Archean basement rocks. These mineralizations display a strong
20 structural control and share many similarities with the world-class unconformity-related U deposits of the coeval
21 Athabasca Basin (Saskatchewan, Canada). An innovative cross-disciplinary study combining macro- to micro-scale
22 characterization was applied to define the uranium mineral system in the Kiggavik area: observation, characterization
23 and measurement of fractures in the field and from drillcores, petrographic and cathodoluminescence identification
24 of fracture cements, analysis of fluid inclusions, and analysis of uranium oxides and related mineral phases through
25 SEM, LA ICP-MS and SIMS. The analysis of fluid inclusions coupled with oriented measurements of fluid
26 inclusions planes they constitute allow allows to link fluid circulation to a tectonic stress and therefore to bridge the

27 gap between the micro and the macro-scales. Our results show that the first order fault/fracture network in the
28 Kiggavik area is mainly oriented ENE-WSW and NE-SW and consists of polyphased fault zones initiated during the
29 Thelon and Trans-Hudsonian orogenies (ca. 1900-1800 Ma). These faults were subsequently U mineralized in four
30 stages referred to as U0, U1, U2 and U3. These different U stages, yield distinctive fracture, alteration and
31 mineralization patterns, indicating different conditions of formation. U0, inferred to be of magmatic-volcanic origin,
32 likely occurred at ca. 1830 Ma and is related to micro-brecciation and weak clay-alteration under a WSW-ENE
33 compressional stress. This event predates intense quartz brecciation, iron oxidation and veining at ca. 1750 Ma. This
34 silicifying event, called Quartz Breccia (QB), predates the deposition of the Thelon Basin and is of magmatic-
35 epithermal origin, associated with anorogenic rifting and emplacement of the Kivalliq igneous suite. Circulation of
36 Si-bearing magmatic derived fluids caused pervasive silicification of former fault zones, which in turn controlled
37 subsequent fracture development and behaved as barriers for later U mineralizing fluids (U1 to U3). Both the U0
38 mineralization and the subsequent QB silicifying event reflect the importance of pre-Thelon Basin fracturing and
39 fluid circulation events in controlling the development and location of later U mineralizing stages. U1, U2 and U3
40 postdate deposition of the Thelon Basin. U1 is characterized by polymetallic mineralization in reduced narrow fault
41 zones and U2 is characterized by monometallic mineralization in oxidized wider fault zones. These two
42 mineralization episodes are characterized by illite and sudoite crystallization and occurred under a regional strike-
43 slip stress regime, with the direction of σ_1 evolving from WNW-ESE (U1) to NE-SW /ENE-WSW (U2); both
44 formed between ~1500-1330 Ma and are related to circulations of Thelon-derived U-bearing basinal brines similar to
45 the mineralizing brines at the origin of the 1600-1270 Ma unconformity-related U deposits in the Athabasca Basin. A
46 post U2, but pre-Mackenzie dikes, NE-SW extensional stress caused normal-dextral offset of the orebodies by
47 reactivating NNW-SSE and E-W faults. This fracturing event triggered circulation of hot (~300°C), probably acidic
48 fluids, dequartzifying, illitizing and bleaching the host-rock. U3 is a redistribution/reconcentration of the previous U
49 mineralization along redox fronts, postdating MacKenzie dike (ca. 1270 Ma) and occurred through weak reopening
50 of the pre-existing fracture network enhancing percolation of low temperature meteoric fluids during two main
51 events at ca. 550 and 350 Ma.

52 Our study shows that U deposits and prospects in the Kiggavik area are of mixed type: a pre-basin magmatic-
53 volcanic U stock (U0) remobilized by post-basin basinal brines to form unconformity-related mineralization (U1 and
54 U2), which were lately altered and remobilized by massive percolations of meteoric waters (U3). This zone

55 demonstrates thus a mobility of U during more than 1.5 billion years and had an evolution similar to that of the
56 world-class U district of the Athabasca Basin. A significant difference with the Athabasca Basin is however that the
57 strongest clay alteration event, formed by illite and linked to the MacKenzie dike intrusions, postdates the main
58 stages of mineralization (U0 to U2).

59 **Keywords**

60 Uranium; deposit; structural control; uranium dating; clay alteration; fracture; Thelon Basin; Kiggavik;
61 unconformity-related; brines

62 **1. introduction**

63 Numerous uranium (U) occurrences have been discovered since the 1970s in the Thelon-Baker Lake area in the
64 Nunavut Territory, northern Canada (Curtis and Miller 1980; Miller 1980, 1982, 1995; Miller and LeCheminant
65 1985; Miller et al. 1986). In this area, the Paleo- to Mesoproterozoic Thelon Basin presents direct similarities
66 whether in term of sedimentology, geology, structural evolution, and diagenetic history with the Athabasca Basin
67 (Saskatchewan, Canada), located further south and which hosts the largest number of high grade unconformity-
68 related uranium (URU) deposits in the world (Miller and LeCheminant 1985; Fuchs et al. 1986; Weyer et al. 1987;
69 Friedrich et al. 1989; Fuchs and Hilger 1989; W Jefferson et al. 2007). Based on this knowledge, the Thelon Basin
70 and its related basement have been considered as prospective for the discovery of URU deposits and thus have been
71 explored since the 80s. Among the different prospective zones, the Kiggavik area, located on the eastern border of
72 the Thelon's Aberdeen sub-basin (Fig. 1), has been explored since the 1980s and several uranium orebodies of
73 economic interest were discovered: Kiggavik (Main Zone, Center Zone, East Zone), Bong, Andrew Lake, End,
74 which are deposits, and Granite grid, 85W, Sleek, Jane and Contact, which are prospects (Fig. 2; Fuchs et al. 1986;
75 Riegler et al. 2014; Chi et al. 2017; Roy et al. 2017).

76 Various scientific studies have been carried out on these orebodies to characterize the specific key parameters
77 which controlled the formation of these U mineralization, with the objective to compare them with those controlling
78 the formation of the world-class URU deposits in the Athabasca Basin (Jefferson et al. 2007; Cuney and Kyser
79 2009). Previous studies about the Kiggavik area mainly focused on the characterization of mineralizing fluids and
80 their alteration products throughout analysis of fluid inclusions and geochemical analysis and age-dating of U oxides
81 and related clay minerals (Farkas 1984; Riegler et al. 2014; Sharpe et al. 2015; Chi et al. 2017; Shabaga et al. 2017).
82 The tectonic history, the related structural controls and the relative timing of the deposits have not been studied in

83 detail and are consequently weakly understood although they are key parameters for the URU deposits in the
84 Athabasca Basin. A recent work on the Contact prospect (Grare et al. 2018a), has provided the first detailed picture
85 of the successive pre- and syn/post-Thelon fracturing/faulting events at different scales and their role in the
86 formation of U mineralization within this prospect. A major difference, in contrast to the Athabasca Basin where
87 ductile to brittle tectonics involving Hudsonian graphitic-rich shear zones reactivated exerted a major structural and
88 metallogenic control on the formation of the deposits (Polito et al. 2005; Pascal et al. 2015; Martz et al. 2017), is that
89 the tectonic style of deformation and mineralization in the Kiggavik area is dominantly brittle, as exemplified by
90 prevailing cataclastic to ultracataclastic fault rocks (Grare et al. 2018a). Graphite is almost absent from the basement
91 lithologies and faults within the Kiggavik area.

92 Based on the study of fluid inclusions in quartz-carbonate veins spatially associated with U mineralization at
93 End deposit, Chi et al. (2017) proposed that a ca. 1300 Ma U mineralization initially formed from high-salinity (> 30
94 wt% NaCl), 80-200°C Na- to Ca-rich basinal brines derived from the Thelon Basin, which is slightly higher in
95 salinity than original Na-dominated diagenetic fluids defined within the Thelon Basin (Renac et al. 2002). These Na-
96 to Ca-rich basinal brines are similar in terms of P-T of circulations and chemistry to the mineralizing fluids in the
97 URU deposits of the Athabasca Basin (Pagel 1975; Derome et al. 2005; Richard et al. 2010, 2016; Chu and Chi
98 2016; Martz et al. 2018). For Bong deposit, Sharpe et al. (2015) proposed a five-stage metallogenic model with
99 primary U mineralization occurring at ca. 1500 Ma, followed by different U mineralizing stages/remobilizations
100 almost until the present time, for which the structural parameters are poorly known. The nature of the mineralizing
101 fluids are unconstrained for the first stage and those related to the second stage of mineralization (at 1100 Ma) are
102 isotopically closer to meteoric fluids rather than to basinal brines. Shabaga et al. (2017) proposed, based on chemical
103 characterization and age-dating study of alteration products and U mineralization, that three events of mineralizing
104 fluids (ca. 1030 Ma, 530 Ma and <1 Ma) were active at Andrew Lake and dominantly meteoric and oxidizing then
105 acidic, meteoric and oxidizing. Illite-chlorite-U oxide association is commonly observed (Riegler et al. 2014; Sharpe
106 et al. 2015; Chi et al. 2017; Shabaga et al. 2017) for the primary stage of mineralization in the whole Kiggavik area.
107 The hydrothermal chlorite has a dominant sudoitic composition, as observed for the hydrothermal chlorite linked to
108 U mineralization in the Athabasca Basin (Hoeve and Quirt 1984; Kotzer and Kyser 1995).

109 Anand and Jefferson (2017) recently released a structural synthesis for the Kiggavik area, based on satellite and
110 geophysical map interpretation, and on field data. This model presents a district-scale structural evolution from ca.

111 2760 to 447 Ma and emphasizes multiple reactivation of a Riedel shear system. Their approach contrasts with the
112 detailed sequence of fracturing/faulting events published by Grare et al. (2018a) for the Contact prospect that was
113 reconstructed on the basis of both macroscopic (drill core and field data) and microscopic (optical microscopy,
114 cathodoluminescence and SEM) paragenetic observations, and on a precise appraisal of chronological constrains.

115 This review of previous works highlights that the nature of the U mineralization at Kiggavik and their controls
116 (structural, fluid, timing and physico-chemical) are still under debate. Despite the work by Anand and Jefferson
117 (2017) that provides insights into the succession of regional tectonic events, the link between the macroscale and the
118 microscale fractures and U mineralization, and the 3D architecture of faults zones in the Kiggavik area remains also
119 unconstrained. These points need however to be carefully addressed for building a complete metallogenic model of
120 U mineralization in the Kiggavik area. For this purpose, we propose here a specific and innovative work combining
121 (1) the evolution of the structural framework controlling the U mineralization in the Kiggavik area with (2)
122 mineralogical, geochemical and dating observations and measurements to fully depict the U system in this zone.
123 Such work will facilitate the comparison with the world-class URU mineralization from the Athabasca Basin.

124 The aims of this contribution are therefore:

125 (1) to depict the brittle tectonic stages leading to the formation of the fault/fracture network that controls the U
126 mineralization in the Kiggavik area and to determine its spatial-temporal evolution on the basis of multi-
127 scale observations: review of the existing drill core information, coupled with structural analysis of oriented
128 data from both outcrops and drill core, integrating samples from new drill holes from various deposits and
129 prospects. Our work uses as a starting point the characterization of the sequence of brittle structural events
130 established at the Contact prospect (Grare et al. 2018a). Oriented measures of fluid inclusions planes were
131 also used to constrain the related tectonic stress at the time of fluid circulations.

132 (2) to establish the nature of the paleo-fluids and their conditions and timings of circulation through the
133 identified fracture networks and tectonic episodes by the analysis of the resulting fluid-rock interactions, i.e.
134 the fluid inclusions, the fracture infill products (cements, clays, ore minerals), and U mineralization. For this
135 purpose, new mineralogical observations have been made, coupled with chemical characterization of fluid
136 inclusions, alteration products and U oxides. New U/Pb isotopic and geochemical measurements on U
137 oxides were also performed to define the physico-chemical conditions and ages of formation/alteration.

138 They are compared with published data for the Kiggavik area to better constrain the timing and conditions
139 of the mineralizing events.

140 As an outcome of this multi-faceted approach, we finally propose an integrated structural and metallogenic model for
141 the formation of the U deposits and prospects in the Kiggavik area. This model includes both pre-Thelon and post-
142 Thelon Basin U ore formation, and for the first time fully illustrates the genesis and evolution of U mineralization of
143 the prospective Kiggavik area and related Thelon Basin.

144

145 **2. Geological setting**

146 **2.1 Regional setting**

147

148 The Thelon Basin (ca. 1670–1540 Ma, [Hiatt et al. 2003](#); [Davis et al. 2011](#)) and the Athabasca Basin (1740–
149 1540 Ma, [Ramaekers et al. 2007](#)) are Proterozoic intracratonic basins ([Gall et al. 1992](#)) hosted by the Churchill
150 Province, which resulted from the collisional amalgamation of the Rae and Hearne cratons along the Snowbird
151 Tectonic Zone (STZ), either in the Neoproterozoic or during the Snowbird orogenesis at ~1.9 Ga ([Hoffman 1988](#);
152 [Corrigan et al. 2009](#); Fig. 1). These basins are located between the eroded remnants of the Trans-Hudson orogenic
153 belt to the Southeast (ca. 2070–1800 Ma, overall NW-SE shortening) and the Thelon-Taltson orogenic belt to the
154 west (ca. 2020–1900 Ma, overall E-W shortening). The Thelon Basin mainly consists of the Thelon Formation, an
155 1800-meter-thick sedimentary pile of conglomerates and coarse-grained sandstones, overlain by the ca. 1540 Ma
156 shoshonitic basalts of the Kuungmi Formation ([Chamberlain et al. 2010](#)) and marine dolomites of the Lookout Point
157 Formation ([Gall et al. 1992](#)) of the Barrenland Group (Fig. 1).

158 The Thelon Formation unconformably overlies a complex set of sedimentary and bi-modal volcanic-sedimentary
159 rocks that filled up the Baker Lake Basin which developed between 1850 Ma and 1750 Ma ([Rainbird et al. 2006](#);
160 [Rainbird and Davis 2007](#)). The Baker Lake Basin formed as a result of (retro-arc) extensional to transtensional
161 rifting tectonics related to the pre/syn-collision between the Churchill province and the Superior province (the Trans-
162 Hudsonian orogeny). It was followed by uplifting, extensive erosional peneplanation and regolith formation, over
163 which deposited the Thelon formation, linked to thermal subsidence ([Rainbird et al. 2003](#); [Rainbird and Davis 2007](#);
164 [Hadlari and Rainbird 2011](#)). The Barrenland, Wharton and Baker Lake groups are parts of the Dubawnt Supergroup
165 ([Peterson, 2006](#)) (Fig. 1) which overlies the metamorphosed Archean basement : the latter comprises ca. 2870 Ma

166 granitic gneisses (Davis et al. 2006), 2730–2680 Ma supracrustal rocks of the Woodburn Lake Group (Pehrsson et al.
167 2013) and a distinctive package of 2620–2580 Ma felsic volcanic and related hypabyssal rocks known as the Snow
168 Island suite (Jefferson et al. 2011; Peterson 2015; Johnstone, 2016). They are overlain by the Paleoproterozoic
169 (2300–2150 Ma, Rainbird et al. 2010) orthoquartzite of the Ketyet River Group (Fig. 2). These rocks, especially the
170 Woodburn Lake Group, host the uranium mineralization in the Kiggavik area (Fig. 2).

171 The Archean to Paleoproterozoic rocks of the Churchill province were intruded by three intrusive suites: (i) the
172 late syn-orogenic (ca. 1830 Ma) Hudson suite (Peterson et al. 2002), (ii) the Dubawnt minette suite
173 (contemporaneous of the Hudson suite), with ultrapotassic rocks, minette dikes and lamprophyres, and (iii) the
174 rapakivi-style Nueltin granite of the anorogenic (ca. 1750 Ma) Kivalliq igneous suite (Hoffman 1988; Breemen et al.
175 2005; Peterson et al. 2015; Scott et al. 2015). Minor uranium mineralization are hosted in fractures and faults
176 developed in Hudson granitoids at the 85W prospect. Dikes of the giant Mackenzie diabase swarm (1267±2 Ma;
177 LeCheminant and Heaman 1989; Heaman and LeCheminant 1993) form prominent linear aeromagnetic features
178 trending NNW-SSE (Tschirhart et al. 2013, 2017); they cut across all of the previous rocks and represent the last
179 magmatic-tectonic event in the region.

180

181 **2.2 Local setting, main fault structures and tectonic evolution**

182

183 In the Kiggavik area, the previously described basement rocks are intruded by the Schultz Lake Intrusive
184 Complex (SLIC) (Scott et al. 2015). The SLIC comprises rocks from the two intrusive suites previously described
185 (Scott et al. 2015): (i) the “Hudson granite” consists of non-foliated granitoid sills, syenites and lamprophyre dikes of
186 the late syn-orogenic Hudson suite. (ii) The “Nueltin granite” comprises anorogenic granite to rhyolite of the
187 Kivalliq igneous suite (Peterson et al. 2015). Uranium and thorium primary enrichment were described to be
188 associated with bostonite dikes (Peterson et al. 2011) and pegmatites attributed to emplacement of the Dubawnt
189 minette (ca. 1830 Ma) and Kivalliq igneous suite, respectively. Such bostonite dikes were observed near the
190 Kiggavik Main Zone (Anand and Jefferson 2017). These rocks are unconformably overlain by the Thelon Formation,
191 which crops out in the Northern part of the Kiggavik property (Fig. 2). Several dikes of the Mackenzie swarm form
192 NNW-SSE lineaments observed in the area.

193 The main structural features in the Kiggavik area are the ENE-trending Thelon fault (TF) and the Main Zone
194 fault (MZF) in the northern part of the property, the ENE-trending Judge Sissons fault (JSF) in the central part, and
195 the NE-trending Andrew Lake Fault (ALF) in the southwestern part (Fig. 2). The MZF hosts 85W, Granite grid and
196 Kiggavik (Main, Central and East Zones). End is hosted by the JSF, while Andrew Lake, Jane and Contact occur
197 along the ALF (Fig. 2) (see also [Grare et al. 2018a](#)).

198 Tectonic initiation of these faults likely dates back to the convergence of cratonic blocks during the latest stage
199 of Trans-Hudsonian orogeny. The TF constitutes the boundary between the siliciclastic sedimentary rocks of the
200 Thelon Formation to the north and the metamorphosed basement rocks to the south (Fig. 2). South of the TF,
201 magnetic maps show that the SLIC is crosscut by numerous ENE-trending parallel and sub-parallel faults with
202 apparent right-lateral displacement ([Tschirhart et al. 2017](#)). It has been observed on discontinuous outcrops and in
203 drill holes that the JSF dips steeply to the north. The ALF constitutes the mapped boundary between the Hudson
204 granite to the west and the metamorphosed basement rocks to the east (Fig. 2). The ALF is delineated from
205 interpretation of aeromagnetic and ground gravity maps (Fig.2) ([Roy et al. 2017](#); [Tschirhart et al. 2017](#)), as outcrops
206 are almost absent.

207 The recent study of the Contact prospect ([Grare et al. 2018a](#)) gave new insights into the structural evolution of
208 the ALF, an evolution which also included a post-Thelon U mineralizing event. Grare et al. (2018a) highlighted the
209 presence of an extensive silicification event along the ALF, characterized by a quartz-healed breccia, termed the
210 Quartz Breccia (QB) in the literature ([Grare et al. 2018b](#)). This structure is a main feature of both the JSF and the
211 ALF: it is observable on outcrops ([Anand and Jefferson 2017](#)) and is systematically intersected by drill holes ([Grare
212 et al. 2018b](#)). Finally, the main stages of fracturing/ mineralization recognized by Grare et al. (2017; 2018a,
213 summarized in Fig. 3) at Contact include brittle tectonic activity along the Andrew Lake fault (fracturing stage 1 or
214 f1), development of the quartz-cemented breccia (QB, f2), the first stage of U mineralization (f5), the second stage of
215 U mineralization (f6), faulting associated with strong clay alteration and bleaching of the host rock (f8), and late U
216 mineralization remobilization linked to the circulation of meteoric fluids (f9).

217

218 **3. Methodology**

219 **3.1 Collection of data from field and drill cores**

220 One hundred and forty samples were collected from drill cores obtained during 2014 and 2015 exploration
221 campaigns done by Areva Resources Canada (ARC, now Orano Canada); 28 samples come from Andrew Lake, 5
222 from End, 14 from Kiggavik Center Zone, 66 from Contact and 27 from 85W (see location of deposits and prospects
223 in Fig. 2). In addition to classical drilling realized during the exploration campaigns, two double tubing exploration
224 drill holes (named CZ-15-01 and AND-15-01) allowing for a better preservation of the drill cores were done and
225 studied. One was drilled at the Andrew Lake deposit and one at Kiggavik Center Zone deposit. Several drill holes
226 (~50) from previous exploration campaigns were also re-observed in detail (fracture orientations, crosscutting
227 relationships, cements and associated alteration and mineralization).

228 Field observations of faults, joints and veins were also made on outcrops and, when possible, compared and
229 combined with previous field observations made by ARC geologists. Fault zones were characterized in drill cores by
230 the identification of fault cores with occurrence of fault rocks such as breccias or gouges. Fault damage zones
231 (Chester and Logan 1986; Wibberley et al. 2008; Faulkner et al. 2010) were documented by the associated veins
232 (mode I or mixed mode I-mode II), joints (mode I) and undifferentiated fractures; an “undifferentiated fracture” in
233 this case relates to a fracture plane which cannot be unambiguously classified as vein, joint or fault/micro-fault (no
234 kinematic indicator). Fracture corridors and isolated veins, joints and undifferentiated fractures were also
235 systematically reported.

236 Oriented data from the complete Kiggavik area’s ARC database were collected and processed. Orientations of
237 ~2,000 fractures and foliation planes were measured from oriented drill cores. Drill cores were oriented using a
238 Reflex ACT III digital core orientation tool (Bright et al. 2014), and then a protractor was used to measure angles
239 between fractures and the core axis (alpha angle). The angle between the bottom of the hole and the inflection line
240 (beta angle) was also measured for calculation of true dip/dip direction data. Acoustic televiewer probing ABI40
241 (Williams and Johnson 2004) was run through several holes providing accurate oriented data in faulted core
242 intervals. The mesostructural data were processed to their true orientation and plotted with Dips 6.0 software by
243 Rocscience. Uncertainty on orientation measurements is usually about 10° as estimated from the comparison
244 between oriented core-measurements and acoustic televiewer data.

245

246 3.2 Optical microscopy observations and scanning electron microscope (SEM) analysis

247 Microscopic observations were carried out to compare with and complete the mineralogical observations made
248 by previous authors on the deposits of the Kiggavik area but also to bring new insights into the genetic link between
249 fractures, alterations and U mineralization. Thin sections made on veins and fault rocks were studied under a Motic
250 BA310 POL Trinocular, using transmitted and reflected lights, and a HIROX SH-3000 Scanning electron
251 microscope (SEM) equipped with a back-scattered electron detector and a nitrogen free Energy Dispersive
252 Spectrometer (EDS) BRK D351-10 with digital mapping capabilities at Orano la Defense site. The SEM was
253 operated at low accelerating voltage (10 kV), 100 nA filaments current and 600 Å beam width for a working distance
254 between 8 and 39 mm. Complementary observations on mineralogical observations and U mineralization were
255 performed at Service Commun de Microscopie Electronique et de Microanalyses (SCMEM) of GeoRessources lab
256 (Vandoeuvre-lès-Nancy, France), using a JEOL J7600F Scanning electron microscope equipped with an energy
257 dispersive spectrometer.

258

259 **3.3 Cathodoluminescence**

260 The different generations of carbonate vein cements were characterized using a Technosyn Cold
261 Cathodoluminescence device (model 8200 MkII), operating between 10 and 12 kV gun potential and between 150
262 and 350 µA beam current. Observations were carried out at the University of Barcelona, Spain (Departament de
263 Mineralogia, Petrologia i Geologia Aplicada, Facultat de Ciències de la Terra).

264

265 **3.4 Electron microprobe analysis (EMPA) and geothermometry of clay minerals**

266 The chemical composition for major elements in U oxides and clay minerals (mainly chlorites and illite) were
267 measured using a CAMECA SX-100 Electron Microprobe Analyser also at SCMEM. The analytical conditions were
268 an accelerating voltage of 15 kV and 10 nA current. The calibration used natural and synthetic oxides and/or alloys
269 (orthoclase, albite, LaPO₄, CePO₄, wollastonite, UO₂, PbCrO₄, olivine, DyRu₂). The counting times were 10s (K, Na,
270 Ca), 20s (Ce, U, Si), 40s (Dy), 50s for Pb, and 60s for La. Complementary measurements on U oxides and clay
271 minerals were made on 6 thin sections with a CAMECA SX-50 electron microprobe and conducted at the Camparis
272 service in Sorbonne Université (Paris), based on the same analytical conditions as used at SCMEM.

273 In the Kiggavik area, clay minerals such as chlorite and illite are a common product of host-rock alteration. They
274 are also found in fractures as neo-formed minerals. Variations in the chemical composition (Tschermak, di-tri-

275 octahedral, Fe-Mg exchange, $\text{Fe}^{3+}/\text{Fe}^{2+}$ ratio) of chlorites are a powerful tool for estimating the crystallization
276 temperature of the clay minerals, which is referred to as chlorite geothermometry. Temperatures were calculated
277 following the equation of Cathelineau (1988), Zang and Fyfe (1995) and Kranidiotis and McLean (1987). White
278 mica crystals were selected from the main altering and/or mineralizing stages for electron microprobe analysis, and
279 the determined major element compositions (site occupancy and end-member mineral data) were used to calculate
280 the precipitation temperatures. Temperatures were calculated following the equation of Cathelineau (1988). Micas
281 coating or cementing fractures and filling pores were selected rather than replacement micas in order to minimize the
282 influence of precursor minerals, hence to ensure their representativity of the selected fracturing stages.

283

284 **3.5 Secondary ion mass spectrometry (SIMS) and LA-ICP-MS for U-Pb dating and geochemical** 285 **tracing of U oxides**

286 The Pb/Pb and U-Pb isotopic compositions of U oxides was determined using a CAMECA ims 1280-HR
287 Secondary Ion Mass Spectrometer (SIMS) at CRPG-CNRS (Nancy, France). The O^- primary ion beam was
288 accelerated at 13 kV, with an intensity ranging between 3.5 and 5 nA, and focused on a spot of ca. 15 μm diameter.
289 The primary beam was set in Gaussian mode with a raster of 10 μm . The field aperture was set to 2,000 μm and the
290 transfer optic magnification was adjusted to 80. Rectangular lenses were activated in the secondary ion optics to
291 increase the transmission at high mass resolution. The energy window was opened at 30 eV, and centred on the low
292 energy side, 5 eV before the maximum value. An offset of 50 eV was applied during the analyses in order to avoid
293 matrix effects due to mixtures of uraninite and silicate in natural samples. Ions were measured by peak jumping in
294 monocollection mode using the axial Faraday cup (FC) for ^{238}U and ^{238}UO and the axial electron multiplier (EM) for
295 ^{204}Pb , ^{206}Pb , ^{207}Pb , ^{208}Pb , and ^{248}ThO . Each analysis consisted of 8 successive cycles. Each cycle began with
296 measurement at masses 203.5 and 203.6 to obtain the background measurements for the FC and EM. Counting times
297 were 4 s for 203.5, 203.6, ^{208}Pb and ^{238}U ; 3 s for ^{248}ThO and ^{238}UO ; 6 s for ^{206}Pb ; 10 s for ^{204}Pb ; and 20 s for ^{207}Pb
298 (waiting time of 1 s). The standard used was an uraninite sample from Zambia (concordant age of 540 ± 4 Ma;
299 Cathelineau et al. 1990), analysed before and after each sample for sample bracketing calibration. The error on the
300 calibration curve is reported in the error given for each analysis. The $^{204}\text{Pb}/^{206}\text{Pb}$ ratio were low (<0.00001) for
301 standard and unknowns, indicating that common lead was not incorporated at the time of crystallization, except for
302 sample 9850 (0.000019-0.004619). A correction for common lead was however made for each analytical spot for all

303 samples by precisely measuring the ^{204}Pb amount and by calculating the composition of the common lead at the time
304 of crystallization, based on the $^{207}\text{Pb}/^{206}\text{Pb}$ measured age and using the Pb isotopic composition calculated from
305 Stacey and Kramers (1975) model. Ages and error correlations were calculated using the ISOPLOT flowsheet of
306 Ludwig (Ludwig 2007). Uncertainties in the ages are reported at the 1σ level.

307 The Rare Earth Elements-REE (La, Ce, Pr, Nd, Sm, Eu, Gd, Tb, Dy, Ho, Er, Tm, Yb, Lu) concentrations in the
308 different U oxides were quantified using a LA-ICP-MS system (GeoLas excimer laser (ArF, 193 nm, Microlas)
309 coupled to Agilent 7500c quadrupole ICP-MS at GeoRessources lab) with a 16-24 μm spot size. The detailed
310 instrumentation and methodology are described in Lach et al. (Lach et al. 2013).

311

312 **3.6 Fluid inclusions (FI) and fluid inclusion planes (FIP)**

313 Secondary FIs (trapped after the formation of the quartz host crystals) organized in FIP were studied in primary
314 magmatic quartz, to define the properties of fluids and the tectonic stress under which they circulated, as FIPs are
315 considered as mode I fractures containing fluid inclusions, FIPs being supposed to have formed perpendicular to the
316 least principal stress axis σ_3 , i.e. in the plane that favours the maximal decrease of the total energy of the system
317 (Lespinasse and Pêcher 1986; Gueguen et al. 1995; Lespinasse 1999; Lespinasse et al. 2005). In our study, directions
318 of the different FIPs were measured, FIPs being mainly subvertical fractures. The work focused on FIPs rather than
319 on primary FIs in order to link a fluid circulation to a tectonic stress and therefore to bridge the gap between the
320 micro and the macro-scales. Sampling for FI studies was carried out from drill core obtained during the 2014 and
321 2015 summer field campaigns. A selection of four oriented samples was collected at 85W and Contact (only
322 locations where oriented samples were available) and attention was paid to take samples not too close to fault zones,
323 when possible, in order to avoid local perturbation of the stress field. A thin section and a wafer were prepared on a
324 horizontal plane from selected zone of the oriented drill core in order to have a “map view” of the subvertical FIPs.
325 FIP orientations were measured under transmitted light microscope using the AnIma software (Lespinasse et al.
326 2005). More than 100 orientation measurements were done per sample, on a restrained zone ($\sim 25\text{ mm}^2$), to provide a
327 statistical representativity of the data proposed.

328 Microthermometry was carried out on fluid inclusions (FI) from the FIPs using a Linkam® MDS600 heating-
329 cooling stage, adapted to an Olympus® microscope at the GeoRessources lab. A total of 99 secondary fluid
330 inclusions from FIPs were studied for microthermometry. The following microthermometric parameters were

331 measured for liquid-dominated FIs: First melting temperature (T_e), melting temperatures of ice and hydrohalite (T_m
332 ice and $T_{m\text{hyd}}$), halite dissolution ($T_s\text{NaCl}$), and homogenization temperature (T_h) (Liq. + Vap. \rightarrow Liq. or Liq. +
333 Vap. + NaCl \rightarrow Liq. + NaCl or Liq. + Vap. + NaCl \rightarrow Liq. + Vap. \rightarrow Liq.). The temperatures of phase changes have
334 a precision of about $\pm 5\text{ }^\circ\text{C}$ for T_e , $\pm 0.1\text{ }^\circ\text{C}$ for $T_{m\text{ice}}$, $T_{m\text{hyd}}$ and $\pm 1\text{ }^\circ\text{C}$ for $T_s\text{NaCl}$ and T_h . Fluid inclusions (FIs)
335 were classified following Derome et al. (2005), the nomenclature based on both the T_m ice ranges ($T_m\text{ ice} < -30^\circ\text{C}$:
336 Lw' and Lwh' ; $-30^\circ\text{C} < T_m\text{ ice} < -15^\circ\text{C}$: $Lw1$, $Lw2$ and Lwh ; $-15^\circ\text{C} < T_m\text{ ice}$: Lw''), the last observed phase to melt
337 at low temperature upon heating (ice: $Lw1$, Lw' and Lw'' ; hydrohalite: $Lw2$, Lwh), and the homogenisation sequence
338 of halite-bearing inclusions (Liq. + Vap. + NaCl \rightarrow Liq. + NaCl \rightarrow Liq. : Lwh' ; Liq. + Vap. + NaCl \rightarrow Liq. + Vap.
339 \rightarrow Liq.: Lwh). FIs that do not nucleate any ice even at -190°C were assigned to Lw' type (Derome et al. 2005).
340 Salinity is estimated from microthermometry (in wt.% NaCl equiv.).

341 Gas species in the vapor phase of fluid inclusions were determined at room temperature with a Labram Raman
342 microspectrometer equipped with a Edge filter, a holographic grating with 1800 grooves per millimetre and a liquid
343 nitrogen cooled CCD detector at GeoRessources (Nancy, France) (Dubessy et al. 1989). The exciting radiation at
344 514.5nm provided by an ionized Argon laser (Spectra physics) was focused on the vapor phase of the fluid inclusions
345 using a X80 objective (Olympus). Using this setup, neither limits of detection nor absolute concentrations of trace
346 gases, can be determined. However the relative proportions of the different gas species at room temperature can be
347 estimated qualitatively (Dubessy et al. 1989). The targeted gas species were those commonly found in FIs from URU
348 deposits (H_2 , O_2 , CO_2 , CH_4 , N_2 , C_2H_6) (Richard 2017).

349 The quantification of the chemical composition (major, minor and trace elements) of water dominated FIs was
350 tempted using the LA-ICP-MS system composed of a GeoLas excimer laser (ArF, 193 nm, Microlas) coupled to an
351 Agilent 7500c quadrupole ICP-MS at GeoRessources lab (Leisen et al. 2012). The isotopes analysed were: ^{23}Na , ^{11}B ,
352 ^{24}Mg , ^{39}K , ^{44}Ca , ^{55}Mn , ^{57}Fe , ^{63}Cu , ^{66}Zn , ^{88}Sr , ^{55}Cs , ^{137}Ba , ^{208}Pb , and ^{238}U , using an integration time of 0.01 s per mass
353 channel for a total cycle time of 0.22 s. The laser was run at 5 Hz with a fluence of $\sim 10\text{ J/cm}^2$. The diameters for
354 ablation vary from 16 to 32 μm . The reference materials NIST SRM610 and 612 were used for the standardization
355 and calibration of the instruments. The instrument was tuned to have the maximum sensitivity for the whole mass
356 range, keeping $\text{Th/U} \sim 1$ and $\text{ThO/Th} < 0.5\%$. The signal integration and data calculation were performed using the
357 Matlab®-based SILLS program using a charge-balance approach (Guillong et al. 2008). The analytical precision for

358 most elements is within 20-30% RSD (Allan et al. 2005). LOD are different for each element measured, however a
359 LOD of ~1ppm is a reasonable approximation for elements with a mass to charge ratio superior to 60.

360

361 **4. Results**

362 **4.1 Characterization of fracturing/faulting events**

363 **4.1.1 Macro/mesoscopic observations**

364 The approach and methods adopted in the present work are similar to those of Grare et al. (2018a) and for
365 the sake of clarity, the presentation of the results follows the sequence of fracturing events defined by these authors
366 (Fig.3). The aim is to establish whether or not the events and timing recognized at Contact can be also recognized in
367 the other deposits and prospects and whether the chronology of events remains the same. Grare et al. (2018a)
368 recognized 10 fracturing events at Contact among which 3 resulted in fracture-controlled U mineralization (Fig.3).

369 *Fracture stage 0 (f0) and oldest stage of U mineralization (U0, Fig. 3).* This stage is named f0 and U0 in
370 order to respect the annotation from f1 to f10 presented in Grare et al. (2018a). This stage f0 predates the stage f1/U1
371 observed at Contact. Indeed, a first fracturing event, unrecognized at Contact was identified at End, Andrew Lake,
372 Kiggavik Main Zone and Bong. This fracturing event is characterized by U-mineralized microbreccia usually
373 displaying a dense network of millimetre-wide greenish microfractures (Fig. 4A), in breccia zones up to a 10m-thick
374 (e.g. in End). U mineralization is observed within the microfractures and is weakly disseminated within the host
375 rock. The mineralization is usually weak but can reach several thousands of counts per second (CPS, AREVA
376 SPPy®) in some breccia zones displaying stronger brecciation. Whatever the grade, the brecciated and mineralized
377 host rock is barely clay altered (Fig. 4B). This mineralized event is crosscut and partially overprinted by the QB (Fig.
378 4A).

379 *Stage f1, pre-Thelon fracturing event (Fig. 3).* At Contact, this stage is marked by faults with proto- to ultra-
380 cataclastic fault rocks along the ALF (Grare et al. 2018a), showing later silicification and crosscut by white quartz
381 veins and mosaic breccia of to the QB.

382 *Stage f2 (Fig. 3):* This stage is characterized in all deposits and prospects by the QB (Grare et al. 2018b)
383 with its characteristic mosaic white quartz-sealed veins and breccia, along major fault zones: at Bong and Kiggavik
384 Main Zone along the ENE-WSW trending MZF, at Jane along the NE-SW trending ALF and at End along the ENE-
385 WSW trending JSF. U mineralization (all stages) is always found in the hanging wall and footwall of the QB but not

386 within the breccia core. F1 and f2 fracturing stages, and the structural control exerted by the QB on later U
387 mineralization were described in details by Grare et al. (2018a, b).

388 *Stage f3 (Fig. 3):* This stage is represented by cm-thick dolomite veins and micro-breccias, and was
389 observed in all deposits and prospects of the Kiggavik area.

390 *Stage f4 (Fig. 3):* This stage is represented by calcite veins that crosscut, thus postdate emplacement of the
391 QB. Described by Grare et al (2018a) as mixed mode-I mode-II shear fractures; they are observed at each deposit of
392 the Kiggavik area, sometimes close to U-mineralized fault zones (f5), and may exhibit calcite-cemented steps and
393 proto-breccia textures.

394 *Stage f5 (Fig. 3):* This mineralizing event is an U mineralizing event (also called U1, Fig. 4C) that postdates
395 deposition of the Thelon Basin. It is characterized by grey-greenish coloured, clay-altered (illite mainly and chlorite)
396 narrow fault zones (Fig. 4C-Andrew Lake) which were also observed in all deposits and prospects of the Kiggavik
397 area. This fracturing event shows strongly mineralized fault zones with protocataclastic to cataclastic fault rocks
398 (Fig. 4C-Bong and Kiggavik MZ) and re-opened, micro-fractured quartz veins from which the mineralization leaks
399 into the foliation (Fig. 4C-End deposit; see also Chi et al. 2017). At 85W, the U mineralization is completely hosted
400 in Hudson granitoids, mainly granites. As a consequence of the absence of foliation and of coarser size of the
401 minerals there, the control by fractures is stronger and easier to observe. In strongly mineralized fault zones, where
402 the mineralization is disseminated in the host rock, biotite is coated with U, which expands along the mineral
403 cleavage (Fig. 4D). Like at Contact (Grare et al. 2018a), clay alteration (illitization mainly, but also chloritization) of
404 the host rock is weak to moderate.

405 *Stage f6 (Fig. 3):* This stage is represented by deep red hematized fault zones and the second stage of U
406 mineralization (U2, Fig. 5A-D). It has been recognized in all deposits of the Kiggavik area. Cataclastic, strongly clay
407 altered (illite and chlorite) fault cores (Fig. 5B-top) and tectonic breccias are usually not mineralized. Hematite veins
408 (Fig. 5B-bottom), millimetre-thick calcite veins (Fig. 5C-top) and microfaults host the mineralization which spreads
409 out into the host rock as blebs surrounded by a rim of bleaching (Fig. 5A, Fig. 5C-top and bottom) in wide fracture
410 networks of bright red oxidized damage zones (Fig. 5D). Alteration of the host rock is stronger compared to the
411 previous stage of uranium mineralization.

412 *Stages f7-f8 (Fig. 3):* These stages represent the strongest clay alteration events in the Kiggavik area,
413 characterized by illitization, de-quartzification and bleaching of the host rock. They are observed in all deposits and

414 prospects. Multiple, un-mineralized, illitized faults were observed at Kiggavik Main Zone (Fig. 5E). These faults
415 crosscut mineralized fault zones (Fig. 5F) and reworked clasts bearing U oxides are observed within cataclastic fault
416 rocks (Fig. 5G-top and bottom). This fracturing stage, recognized for each deposit and prospect but with variable
417 intensity, has been extensively observed at Bong. The greenish colour of some fault zones is due to the presence of
418 retrograde metamorphic chlorite and therefore does not reflect a different fracturing process; additionally, white clay
419 fault zones (f8) are much more frequent compared to greenish clay fault zones (f7); on the basis of these new
420 observations, we propose to group these two fracturing events that were presented separated in Grare et al., (2018a).
421 The strongest clay alteration event is definitively termed f7.

422 The Mackenzie dikes (Fig. 5H) were observed only at Kiggavik Main Zone but these dikes provide strong
423 constraints on the timing of the fracturing events. Indeed, diabase dikes crosscut the altered and mineralized fault
424 zones and are barely fractured and altered, and can therefore be considered as sealing the main tectonic and
425 mineralizing history.

426 *Stage f9 (Fig. 3):* This stage is represented by weak reactivation of the fracture network and U redox fronts
427 (U3) as described at Bong (Sharpe et al. 2015), Andrew Lake (Shabaga et al. 2017) and Contact (Grare et al. 2018a);
428 they have also been recognized at End, Kiggavik Main Zone and 85W (Fig. 6). These remobilization fronts display
429 the typical succession with an oxidized (goethite), un-mineralized zone, a thin black layer where uranium oxides are
430 concentrated and a grey, non-oxidized (reduced) and mineralized zone. These redox fronts are sometime bleached by
431 a later event described at the Contact prospect (f10) which removed iron oxides from the goethite-rich zone and
432 therefore modified the visual aspect of the redox front.

433 Macroscopic re-examination of deposits and prospects in the Kiggavik area therefore confirm the structural
434 stages previously defined by Grare et al. (2018a) at Contact, so that the sequence of fracturing events can be
435 considered as representative of the whole Kiggavik area, although changes in lithologies may have induced
436 differences in the mineralogy of fault rock cements between deposits and prospects. In addition, our approach has
437 allowed for the identification of a new stage of deformation and mineralization (f0 and U0) that predates all those
438 described in Contact and therefore also the formation of the QB, inferred to be a pre-Thelon fracturing event. This
439 initial mineralizing stage is hereinafter characterized more in detail with microscopic observations and geochemical
440 data.

441 To summarize, the fracture/mineralization history of the Kiggavik area is as follows:

- 442 - f0/U0, f1, followed by the brecciation-silicification event, the so-called Quartz Breccia (QB-f2), predate
443 formation of the Thelon Basin.
- 444 - f3 to f7, including two stages of U mineralization (U1-f5 and U2-f6), are syn to post/post-Thelon Basin
445 events. These fracturing/mineralization events predate emplacement of the late NNW-SSE trending
446 Mackenzie dikes swarm that crosscut orebodies, display little to no alteration and show no offset on
447 geophysical maps (Percival and Tschirhart 2017).
- 448 - Late events of U remobilization-reconcentration (U3) along redox fronts postdate the Mackenzie dikes in
449 the Kiggavik area. Even though these events may have had a significant economic impact in terms of ore
450 redistribution, they were likely linked to (weak) fracturing, and do not correspond to a main fracturing stage
451 that significantly alter the structural architecture of deposits and prospects.

452

453 **4.1.2 Geometry and kinematics of fault zones from fracture orientation measurements and** 454 **kinematic data**

455 Figure 3 shows the oriented mesostructural data collected in the prospects/deposits of the Kiggavik area (except
456 for Jane and Sleek). The sequence of faulting/fracturing events and crosscutting relationships are displayed on the
457 first and second columns for reference. The qualitative frequency of the fracture sets for each deposit and prospect is
458 shown by coloured symbols; for example f7 (white clay altered fault zones) is dominant at Bong. Together with
459 orientation data, a statistically significant number of kinematic indicators on veins and faults were also gathered
460 mainly from outcrops located in different parts of the Kiggavik area, usually close to a known deposit or prospect,
461 and also from drill core; they are synthesized in the last column of Fig. 3.

462 Oriented data for the mineralized microbreccia (f0, Fig. 3 row 0) are rare; however, data from major fractures
463 from End collected within the mineralized microbreccia display a NE-SW trend and a steep dip to the NW. The
464 numerous solution seams observed at the micro-scale display a NW-SE to NNW-SSE orientation (data not displayed
465 in Fig. 3). Similarly, microstructures from the pre-QB brittle fracturing event (f1, Fig. 3-row 1), although still
466 observable, are usually strongly silicified and overprinted by the quartz breccia (f2) precluding any reliable
467 collection of oriented data. ENE-WSW striking faults, steeply dipping to the N (mimicking the orientation of the QB,
468 like at Contact) would be expected for this fracturing stage that characterize the primary orientations of the JSF and
469 the MZF, e.g., at Contact (f1, Fig. 3-row 1).

470 Because QB (f2, Fig. 3-row 2) has reused pre-existing main fault zones (e.g. ENE-WSW trending JSF) in the
471 Kiggavik area (Grare et al. 2018b), the related faults/fractures display variable orientation. QB shows a NE-SW trend
472 at Contact and Andrew Lake. Secondary ENE-WSW fracture directions are also observed at Jane and Andrew Lake.
473 The QB displays a main ENE-WSW trend with a steep dip to the North at End and Kiggavik Main Zone. At Bong,
474 the QB is characterized by a NNE-SSW direction and a steep dip mainly to the W and a secondary E-W direction
475 with a steep dip to the N. At 85W, mainly small white quartz veins were observed, displaying dominant E-W
476 directions with steep dip to the N. Quartz veins (from QB, f2) display stepped veins, associated with (Fig. 7A) or
477 without (Fig. 7B) U oxides and arrays of mode I opening fractures (Fig. 7C). Stepped veins are usually trending
478 WSW-ENE and NW-SE (Fig. 7D, 85W, Kiggavik and St-Tropez), while mode I opening veins display a dominant
479 WNW-ESE direction (Fig. 7D, 85W).

480 Like at Contact, measurements of oriented data from calcite veins (f4) were mainly taken from Ca1 veins, as the
481 Ca2 (Fig. 3-row 6b, no oriented data) usually displays veins too thin to be measured or to be unambiguously
482 differentiated from those of the first stage calcite veins. Two directions are observed: E-W and NW-SE, with
483 conjugate dip-directions. Stepped veins cemented with Ca1 (f4) and synchronous U oxides (U1) were observed only
484 in drill core (Fig. 8A). Veins displaying kinematic indicators are rare but some stepped veins were observed and
485 measured; they display ENE-WSW and NW-SE directions (Fig. 8B).

486 F5/U1 fractures (Fig. 3-row 5) follows ENE-WSW to ESE-WNW faults at Contact, dipping to the N. At Andrew
487 Lake, mineralization is found within N-S and E-W faults, but also within reopened and/or microfractured quartz
488 veins trending NE-SW (f2, QB stage, like at Contact). At 85W, faults and minor fractures show an ESE-WNW
489 direction, steeply dipping mainly to the N.

490 F6/U2 fractures (Fig. 3-row 6a) are well observed throughout the Kiggavik area. At Contact, and Andrew Lake,
491 they display N-S to NE-SW directions (i.e., the direction of the ALF). Contact is located on a W-dipping segment of
492 the ALF, while Jane and Andrew Lake are located on an E-dipping segment of the ALF. Looking at the map
493 organisation (Fig. 2), End is likely hosted within an important relay zone of the JSF; there, oxidized fault zones are
494 trending mainly NNW-SSE to NE-SW (Fig. 3-row 6a). At Sleek, the three main faults trends are N-S, E-W and NW-
495 SE, the latter two being visible on maps. At Bong, 85W and Kiggavik Main Zone, the fault trends are similar to those
496 of the QB, however at Kiggavik Main Zone, like for in Contact, an E-W trend with a shallow dip to the S is also
497 recognized. F6 is also characterized by tectono-hydraulic breccia and strongly clay altered fault zones which are both

498 usually not mineralized (Fig. 4G). F6 fractures were observed in the field associated with radioactive anomalies.
499 Study of relay zones allowed for the interpretation of the kinematics of the fault zone (Fig. 9A-B). Kinematic
500 indicators were observed in the field and in drill core and are presented in Fig. 9C; faults with dominant E-W to
501 ENE-WSW orientation show evidence for reverse and/or sinistral motion. Other faults with dextral indicators were
502 also observed in the St-Tropez area (Fig. 9A and C), which is located 20 km to the NNE of Kiggavik Main Zone.
503 The JSF, trending ENE-WSW, displays a reverse-sinistral slip component (Fig. 9C), which postdates the main
504 dextral normal slip component responsible of the Hudsonian granite offset (SLIC, Fig. 2, see also [Anand and](#)
505 [Jefferson 2017](#)).

506
507 Mineralized fractures f6c, as presented in Fig. 3-row 6c, were also observed in other deposits and prospects; they
508 are better represented at Contact, Andrew Lake and Kiggavik Main Zone. At Andrew Lake, the third stage of U
509 mineralization is characterized by ESE-WNW to NW-SE microfaults and by NE-SW millimetric-wide calcite veins
510 (i.e., Ca₂, measured precisely only at Andrew Lake). At End, the second stage of U mineralization is guided by NW-
511 SE to NNW-SSE faults that mainly dip to the E. At 85W, this mineralizing stage is guided mainly by W-dipping
512 NNE-SSW faults and by NW-SE faults as a second direction. At Kiggavik Main Zone, f6c faults are trending either
513 ENE-WSW or NW-SE to WNW-ESE.

514 Finally, f7 fractures were also recognized (f7, Fig. 3-row 8). They are usually associated with NW-SE and E-W
515 trending fault zones (i.e., 85W and End). This fracturing stage is widely encountered and dominant at Bong where it
516 is characterized by E-W trending, N-steeply dipping fault zones. These post-ore fractures display NNW-SSE
517 direction with evidence of strike-slip sinistral motion in End and 85W areas (Fig. 10A-C); these faults display E-W
518 to WNW-ESE orientation, steeply dipping to the N, with a dip-slip normal kinematics. At 85W, micro-faults offset
519 uranium mineralized fractures (f6, Fig. 10B) while at Bong the orebody is offset by E-W striking faults (Fig. 10D).
520 The dip-slip component displacement of the U orebodies (metric to decametric) appears to be greater than the strike-
521 slip component (centimetric to metric).

522
523 **4.2 Petrological observations, chemical compositions of clays, U oxides and fluid inclusions, and U-**

524 **Pb dating of U oxides**

525 **4.2.1 Optical microscopic and SEM observations**

526

527 Samples of the U-mineralized microbreccia (f0, U0) is characterized by the presence of multiple irregular
528 microstructures with interlocking pegs and sockets (Fig. 11A), usually surrounded by a millimetric halo of quartz
529 dissolution similar to solution seams. These microstructures connect to microbreccias, within which millimetric
530 clasts display irregular boundaries reflecting dissolution patterns (Fig. 11B). These micro-structures are cemented by
531 dark green chlorite, ore minerals and are sharply crosscut by quartz veins of the QB (Fig. 11C-E). SEM observations
532 and microprobe characterization show that microfractures are cemented with iron-rich clinocllore, pitchblende
533 (containing up to several percents of thorium), brannerite, titanium oxides and sulfide minerals (mainly pyrite).
534 These minerals are subhedral to anhedral mixed phases (Fig. 11D-F). Microprobe characterisation shows that the
535 iron-rich clinocllore is altered into an Al-rich chlorite (Fig. 11E), close to sudoite (Table 1). Subhedral crystals of
536 brannerite were observed in the same type of fractures/breccias on samples from Kiggavik Main Zone, associated
537 with pitchblende-cemented microbreccia (Fig. 11F and 12A). Rutile with micro-inclusions of U-oxide and coated
538 with anhedral U-Ti phases were observed on samples from Andrew Lake (Fig. 12B). Microfractures within
539 magmatic quartz, cemented with rutile and colloform pitchblende were observed in samples from 85W (Fig. 12C).

540 Stage f5 and associated U1 is characterized by uraninite and pitchblende in fractures often cemented by
541 calcite (Fig. 12D). U1 is spatially associated with open quartz veins displaying colloform pitchblende along the
542 edges, with U oxides “eating away” quartz crystals (e.g. 85W, Fig. 12E). Bravoite-pyrite coated with pitchblende
543 (Fig. 12F) was observed on samples from Jane, a mineralogical association also described at Contact for U1 (Grare
544 et al. 2018a). Silver, gold and selenium phases were observed on samples from Andrew Lake, End and Kiggavik
545 Main Zone. Anhedral Ag-U phases with galena were observed cementing microfractures (Fig. 12G) while gold is
546 usually present as micro-inclusions within pitchblende (Fig. 12H). Aluminum Phosphate Sulphates (APS) were
547 observed associated with pyrite and pitchblende in a grey-greenish fault zone at 85W (Fig. 12I). In the case of f6 and
548 associated U2, U oxides are associated with APS in oxidized rocks at 85W (Fig. 12J). In term of clay alteration
549 minerals, illite and sudoite were observed for U1 and U2 mineralizing stage, they are described more in detail
550 hereinafter. Anhedral pitchblende cementing anastomosing micro-fractures characteristic of this mineralizing stage,
551 was observed at Andrew Lake (Fig. 12K). These new observations confirm and complement previous observations
552 made by Chi et al. (2017), Shabaga et al. (2017), Weyer et al. (1989) and Grare et al. (2018a) at End, Andrew Lake,
553 Kiggavik Main Zone and Contact, respectively.

554 U3 is characterized by anhedral pitchblende, goethite and rare sulfurs (pyrite) cementing micro-fractures
555 and coating various minerals (Fig. 12L)

556
557 **4.2.2 Carbonate cements characterization under cathodoluminescence: link with U mineralization**

558
559 Two generations of calcite veins are observed associated with uranium oxides. The first one, Ca1 (f4), likely
560 formed by mixed mode I/mode II fracturing, synchronous with U1, and the second one, Ca2 (f6b), displays crack and
561 seal textures; it crosscuts U1 and was likely formed by mode I opening.

562 The Ca1 spatially associated with the first stage of U mineralization (U1) shows calcite with a yellowish-
563 orange luminescence and a darker tint when closer to U oxides. At Contact and 85W, colloform pitchblende occupies
564 the edge of re-opened quartz-dolomite veins: dolomite and quartz display irregular boundaries in contact with calcite
565 which separates them from U oxides (Fig. 13A). Calcite is observed cementing microbreccia on samples from 85W
566 and End; U oxides are coating the edges of calcite crystals (Fig. 13B-C) or as subhedral colloform shapes intergrown
567 with the calcite breccia (Fig. 13D), thus indicating synchronous precipitation of calcite and U oxides. A similar
568 observation was made on sample from Kiggavik Main Zone.

569 Ca2 veining occurred during f6 and is spatially associated with U2, likely synchronous with this fracturing
570 event. The millimetric-wide crack-seal calcite veins (Ca2) observed at Contact and associated with the second stage
571 of U mineralization were also observed in sample from End, crosscutting U oxides of U1 (Fig. 13E). The calcite of
572 these veins displays a dark orange luminescence (Fig. 13F). In addition to characterize two calcite cements with
573 different orientations but also luminescence and textures, thus two calcite generations, these observations also allow
574 concluding that f4 Calcite is synchronous with U1 (f5), these two fracturing events could therefore be gathered.

575
576 **4.2.3 Composition and crystallisation temperatures of chlorites and illites**

577
578 **Chlorite**

579 Chlorite in the Kiggavik area fall into three stages: retrograde metamorphic chlorite, chlorite (altered and
580 unaltered) associated with the mineralizing stage U0, and chlorite associated with mineralizing stages U1 and U2.

581 They are chemographically presented in a ternary MR3-2R3-3R2 diagram in Fig. 14A (Velde 1985). Formulae of
582 chlorite associated with U0, U1 and U2, from various locations are presented in table 1.

583 Representative compositions of analysed chlorites from U mineralized microbreccia samples (f0, U0) are
584 plotted in Fig. 14B. Analyzed chlorite cements the microbreccia (Fig. 14C). Representative compositions of fresh
585 chlorite associated with U0, with calculated temperatures, are presented in Fig. 14D, and indicate an iron-rich species
586 of trioctahedral chlorite. Their octahedral occupancy is close to 6 atoms when the structural formulae is calculated
587 with total Fe in the ferrous state and their XFe is generally close to 0.5. Structural formulae of chlorite linked to U1
588 and U2 plot toward the sudoitic pole (di-trioctahedral chlorite, Fig. 14B, complete formulae presented in table 1),
589 characterized by an Al-Mg rich composition and an octahedral occupancy close to 5 atoms. Numerous analyses of
590 chlorites associated with U0 reveal a mixture of variable amounts of iron-rich chlorite and sudoite, showing that
591 neoformed dioctahedral chlorite co-genetic of U0 were altered to di-trioctahedral chlorite. This is consistent with
592 petrographic observations showing dark green chlorite surrounded by light green chlorite (sudoite; Fig. 14C).

593 Temperature calculations were done using several methods (Fig. 14D) only for the Fe-rich chlorite variety linked to
594 U0, as the geothermometers cannot be applied on low-T° di-trioctahedral chlorites like sudoite. The Cathelineau
595 (1988) and Jowett (1991) thermometers returned temperatures ranging from 295 to 333 °C whereas Kranidiotis
596 (1987) and Zang and Fyfe (1995) thermometers returned temperatures ranging from 130 to 159 °C. The temperatures
597 differ considerably, and the estimation of the more likely temperature range needs to be done in the light of textural
598 relationships, as discussed hereafter in the interpretation section.

599

600 **Illite**

601 Selected representative compositions for white micas associated with pre-ore alteration (pre-U0), with U1-
602 f5 and U2-f6 mineralizing stages and late clay alteration micas (f7) are available as supplementary material (ESM-1)
603 and plotted on ternary diagrams representing the average compositional fields of dioctahedral mica-like phases
604 (Dubacq et al. 2010) (Fig. 15A). Pre-ore (pre-U1) alteration (Fig. 15B-C) is characterized by interlayered
605 illite/smectite and smectite. Most of the white mica characterizing the alteration of U1 (Fig. 15B) is illite, as for late
606 ore clay alteration (Fig. 15D). White mica characterizing U2 (Fig. 15C) is represented by illite and interlayered
607 illite/smectite. The distribution of the data points in the diagram likely indicates inheritance of illite from
608 muscovite/sericite.

609 Temperatures calculated using the equation of Cathelineau (1988) return an average of 224°C for pre-ore alteration,
610 289°C for U1, 282°C for U2 and 305°C for f7 (Fig. 15E). The method of calculation of Battaglia (2004) returns
611 similar temperatures.

612

613 **4.2.4 Composition and age of U oxides**

614

615 **REE signatures of uranium oxides**

616 The REEs concentrations for U1, U2 and U3 are available as supplementary material (ESM-2). Fig. 16
617 displays the chondrite-normalized patterns for samples from Andrew Lake and End. Structural and macroscopic
618 characteristics, and mineralogical associations allow defining that they represent U1 (samples 9850, 9568-38, 9568-
619 39 and 9568-08), U2 (samples 9851, And-15-01-05), and U3 (sample And-15-01-04). U0 uranium oxides could not
620 be analyzed by LA-ICP-MS due to their small size, anhedral shapes and mixing with Ti-U phases. Both U1 and U2
621 samples display bell-shaped chondrite-normalized patterns centered on Tb with a small anomaly in Eu (Fig. 16).
622 Samples are enriched in intermediate REE (Sm to Dy) compared with light REE (LREE) and heavy REE (HREE),
623 except for sample 9850 which is enriched in LREE compared to HREE. Samples of U1 are characterized by an
624 HREE/LREE ratio around 1 (9568-38 and 39) or higher (sample 9568-08). Samples of U2 are slightly depleted in
625 LREE and their HREE/LREE ratio is therefore higher. Sample AND-15-01-05 (U2) is enriched in REE compared to
626 the other samples. Sample And-15-01-04 (U3) displays a stronger negative anomaly in Eu, higher concentrations in
627 La compared to other LREE and a high LREE/HREE ratio (~2), comparable to sample 9850.

628 Sample 85W-10-04 displays a different pattern compared to the other samples of the Kiggavik area with the
629 total concentration of REE much higher (up to a factor 10 for each element). The pattern displays a positive trend
630 from La to Sm, centered on Sm and displays a negative pattern from Sm to Lu, this type of trend is observed only for
631 this sample and is described for the first time in the Kiggavik area.

632

633 **Age dating on U oxides**

634 U oxides studied for REEs were also analyzed by SIMS for Pb/Pb and U-Pb isotopic dating. The dated
635 samples come from Andrew Lake (4), End (1) and from 85W (1). Data from 9568-38 and 9568-39 are from Lach

636 (2012). Based on macroscopic characteristics and mineralogical associations, samples 9850, 9568-39, 9809 and
637 85W-10-04 are interpreted to be of U1, samples 9851, And-15-01-05 of U2 and sample And-15-01-04 of U3.
638 Data plot along or below the Discordia in the $^{206}\text{Pb}/^{238}\text{U}$ - $^{207}\text{Pb}/^{235}\text{U}$ Concordia diagrams (Fig. 17), which suggests
639 that most of the samples lost Pb after their crystallization. Electron microprobe analysis shows that studied uraninite
640 and pitchblende display relatively high U contents (~75-86 wt%) but low Pb contents (0-5 wt% usually, ~10 wt% for
641 one sample) especially for U1 and U2, indicating also a loss of Pb which confirms the Pb/U isotopic data. Three
642 samples from Andrew Lake yielded upper intercept ages at 347 ± 58 Ma (sample 9850) and 344 ± 19 Ma (9851) for
643 U1, 565 ± 38 Ma (And-15-01-05, anchored at 0 ± 10 Ma) for U2 and 547 ± 13 Ma (And-15-01-04) for U3. The sample
644 from 85W yields an upper intercept age at 1073 ± 5 Ma (85W-10-04). The samples from End yields upper intercept
645 ages at 1277 ± 10 Ma (9568-38), 1175 ± 23 Ma (9568-39) and 1257 ± 58 Ma (9809). The scattering of the data for
646 sample 9850 is linked to the presence of common lead which was corrected to calculate the upper intercept (black
647 circles are data not considered).

648

649 **4.2.5 Fluids inclusions and fluid inclusion planes characterization**

650 **Fluid inclusions composition**

651 Different types of secondary fluid inclusions were observed as FIPs in quartz, magmatic in origin (primary
652 quartz, in granite and granitic gneiss, predating all other quartz generations) from 85W and Contact.. Two types of
653 FIPs were identified based on the FIs that constitute them: Type 1 and type 2 FIPs (Fig. 18A).

654 Type 1 FIPs are represented by monophasic, vapour-only and dark fluid inclusions (rounded and sometimes
655 “negative crystal” shape; Fig. 18B). Their size varies from 3 to 10 μm . No phase change was observed for these FIs
656 even when they were cooled to -190°C . Analysis of the gas phase by Raman spectroscopy indicates that the FIs are
657 filled with H_2O vapour only.

658 Type 2 FIPs are represented by biphasic and triphasic FIs. Biphasic aqueous FIs are characterized by a dominant
659 liquid phase with a vapour phase representing 10 to 20% of the FI by volume (Fig. 18C, liquid phase is H_2O). They
660 have variable shapes with a size varying from 3 to 20 μm . They comprise three types; Lw', Lw'' and Lw1. Gases
661 other than H_2 and O_2 (CH_4 , N_2) were detected very punctually and only as traces through Raman spectroscopy.
662 Triphasic aqueous FIs display a cube of halite (Fig. 18D, indicating oversaturation in NaCl), and belong to the Lwh'
663 type. They have variable shapes and their size range from 6 to 20 μm . Liquid and vapour phases were analyzed under

664 Raman spectroscopy and like biphasic aqueous FIs, only H₂ and O₂ were detected in the inclusions. Type 1 FIPs are
665 crosscut by type 2 FIPs (Fig. 18E). This indicates the occurrence of at least two episodes of fluid circulation and that
666 type 2 FIPs post-date type 1 FIPs.

667 A summary of microthermometric data obtained for the analysis of biphasic and triphasic FIs (99 FIs studied) is
668 presented in table 2. Inclusions free of halite cube, for which the last phase to melt is ice, are referred to as Lw' (32
669 FIs; -45.4 °C < T_m ice < -31.4 °C), Lw1 (2 FIs; -28.9 °C < T_m ice < -25.9 °C) or Lw'' (17 FIs; -23.9 °C < T_m ice
670 < -1.4 °C). Except for Lw'' inclusions, the observed T_e range from -85 to -60 °C, which indicates a complex
671 composition, possibly H₂O-NaCl-CaCl₂ ± MgCl₂ - KCl. For Lw'' inclusions, the observed T_e range from -65 to
672 -38 °C and may be related to the H₂O-NaCl ± CaCl₂ ± MgCl₂ - KCl as major constituents. Considering all Lw' and
673 Lw1 inclusions, T_m ice display a continuous trend from -45 to -26 °C. T_m ice of Lw'' inclusions range from -24 to
674 -1 °C. T_h varies from 62 to 245 °C and T_s NaCl range from 121 to 222 °C for Lw' inclusions.

675
676 The concentrations of several major, minor and trace elements in aqueous fluid inclusions (mainly Lw' inclusions)
677 were measured through LA-ICP-MS, and the proportions of fluid inclusions with element concentrations
678 above the LOD (usually ~1ppm) are as follows: Na (100%), B (0%), Mg (100%), K (100%), Ca (100%), Mn
679 (100%), Fe (38%), Cu (61%), Zn (54%), Rb (61%), Sr (100%), Cs (23%), Ba (85%), La (85%), Pb (100%), U
680 (77%). The absolute content of every analyzed elements displays a great range of value, the highest being
681 represented by Ca (31 000 to 80 000ppm), Na (5600 to 38 000 ppm), K (3500 to 17 000 ppm), Mg (1200 to 14 000
682 ppm), Fe (from LOD up to 79 000 ppm) and Sr (1000 to 6700 ppm). Metals such as Ba (LOD to 14 000 ppm), and
683 Pb (270 to 11 000ppm) display moderate concentrations. Zn (LOD to 800 ppm), U (LOD to 1000 ppm), Cu (LOD to
684 400 ppm), Rb (LOD to 140 ppm), and Cs (LOD to 40 ppm), display lower concentrations compared to other
685 elements. FIs are characterized by high concentration in Ca compared to Na, indicating that FIs studied are
686 dominated by a CaCl₂-rich brines.

687

688 **Fluid inclusion planes orientation (FIPs)**

689 FIPs of each type were counted and the results plotted in rose diagrams as a function of plane strike (Fig.
690 20). FIPs at 85W are mainly type 1 (186 FIP measurements out of 240). In drill hole 85W-09 (samples 85W-09-07
691 and 85W-09-04), type 1 FIPs display main directions of N100-110. Secondary directions are N10-30 and N120-140.

692 For type 2 FIPs, studied samples returned a main direction of N110-120 and secondary directions around N120-130
693 and N40-60. For drill hole 85W-10 (sample 85W-10-04B), type 1 FIPs display main directions around N350-10,
694 N140-160 and N110-130. Type 2 FIPs have main directions around N60-80 and N120-140. At the scale of 85W (Fig.
695 20, bottom part), there are therefore one main directions for type 1 FIPs: N100-110, and two minor directions: N350-
696 10, and N140-160. Some sub-horizontal FIPs were observed at 85W; they are mainly composed by triphase FIs.
697 Type 2 FIPs show two directions: N110-140 and N40-80.

698 At Contact, type 1 FIPs were also the most represented type (75 FIP measurements out of 96), these FIPs display
699 a main N130-150 direction and secondary N110-130 direction. N0-20 is observed as a minor direction. Aqueous
700 biphasic and triphasic FIPs overprint type 1 FIPs like at 85W. Type 2 FIPs display two directions: N110-120 and N80-
701 N100. FIPs directions were also compared with reference to the orientation of the foliation of the granitic gneiss,
702 which is sub-constant at Contact (N10/10° E).

703

704 **5. Interpretation of the results and discussion**

705 **5.1 Main fracturing/mineralization events in the Kiggavik area**

706 The fracturing events observed at Contact ([Grare et al. 2018a](#)) have been recognized in the other deposits
707 and prospects in the Kiggavik area, confirming that the sequence of events established for this prospect can be
708 extrapolated to the whole Kiggavik area. In addition, the present work has determined a first fracturing and
709 magmatic-volcanic U mineralizing stage (U0). Macro- to micro-scale observations made for the Kiggavik area on
710 outcrops and drill cores coupled to results from the multi-method approach developed are gathered and interpreted to
711 propose for the first time a complete and global metallogenic model for this area.

712

713 **Pre-Thelon fracturing and mineralization events in the Kiggavik area**

714 **Stage U0/f0**

715 U0 is characterized macroscopically by microbrecciation (f0) of the host rock, better preserved at depth.
716 Solution seams characteristics of this fracturing stage are traditionally observed in sedimentary environments (e.g.
717 [Rutter 1983](#); [Benedicto and Schultz 2010](#)) but have also been described in igneous rocks, for example in rhyolite and
718 welded tuffs ([Donald Bloss 1954](#); [Burma and Riley 1955](#); [Golding and Conolly 1962](#)). Oriented data are poor for this
719 fracturing event, making difficult to proper determine of the orientations of the associated structural features.

720 Fractures strike NE-SW to ENE-WSW, and dip NW, reflecting the orientation of the JSF at this location. This
721 mineralizing stage is more represented in deposits and prospects controlled by major ENE trending faults, which
722 highlights the role played by the major fault zones in focusing both fracturing events and fluid circulations through
723 time for the Kiggavik area. Affected basement rocks are only weakly to non clay-altered, with Fe-rich chlorite
724 precipitated at relatively high temperature (>300°C). Such features have not been previously depicted for U
725 mineralization in the Kiggavik area, where mineralization are considered as associated with moderate to strongly
726 clay-altered host rocks (Fuchs and Hilger 1989; Riegler et al. 2014; Sharpe et al. 2015; Shabaga et al. 2017)
727 characterized by lower temperature chlorite (sudoite).

728 Microfracture cement is characterized, among others, by pitchblende and brannerite with Th contents of up
729 to 7%. This mineralogy and the high Th content of U-bearing minerals is not of URU type, for which all analyzed U
730 oxides have Th contents < 1% (Frimmel et al. 2014; Alexandre et al. 2015). This indicates that U₀ is most probably
731 related to magmatic-volcanic-related U ore systems, like those in the Beaverlodge area (Dieng et al. 2013), or the
732 Poços de Caldas peralkaline complex (Schorscher and Shea 1992). These deposits are all related to relatively higher
733 temperatures (>350°C) than the URU deposits (100-220°C) and with fluids with strongly different chemistries and
734 origins. The f₀ mineralized microbreccias predate veins of the QB event (ca. 1750 Ma) and is thus inferred to predate
735 deposition of the Thelon Formation (older than 1667 Ma, Davis et al. 2011). The U₀ mineralization is consequently
736 considered to have occurred before the deposition of the Thelon Basin, at relatively high-T conditions.

737

738 **QB/f₂**

739 The QB event is characterized by breccias present throughout the Kiggavik area in close association with
740 the main fault trends (MZF, JSF, ALF). Emplacement of the QB occurred ca. 1750 Ma before the deposition of the
741 Thelon Basin, associated with emplacement of intrusions of the Kivalliq Igneous suite (Grare et al. 2018b). QB
742 crosscuts and postdates U₀ (Fig. 4A). Main fault trends were the locus of polyphase brittle tectonic activity; they
743 were likely first active before the QB event, and subsequently focused the circulation of Si-rich fluids (meteoric-
744 derived fluids interacting with magmatic-derived fluids, see Grare et al. 2018b) that caused hydraulic fracturing and
745 facilitated repeated fault reactivation. The inner zones of the breccia, much more silicified, are usually less fractured
746 and altered compared to its outer zones; U orebodies are observed within the hangingwalls or footwalls, always out
747 of the inner breccia zone. In addition, the clear spatial association between quartz veins of the QB (in its outer zone)

748 and U mineralization suggests that the most silicified parts of the QB (i.e., the breccia core) was a transverse barrier
749 for fluids but enhanced along-strike migration and entrapment through re-opening of veins in its outer zone. The QB
750 played therefore a major role in partitioning fracturing and fluid flow through time for the different later U
751 mineralization stages (Grare et al. 2018a, b).

752

753 **Syn to post-Thelon fracturing events in the Kiggavik area and related U mineralization**

754 U1 is hosted by relatively narrow fault zones (f5) (thickness of 5 to 20 m, damage core zones included)
755 characterized by grey-greenish altered fault rocks (mainly illite, but sudoite was also characterized in this study and
756 by XRD by Pacquet 1993a, b, c). Oriented data are scarce and except at Contact, they reflect the orientation of the
757 main fault zone in which they are hosted (NE-SW trend of the ALF for the Andrew Lake deposit, WNW-ESE trend
758 of the MZF for the 85W prospect).

759 U1 is usually of high grade and is not the most commonly described mineralization at Kiggavik, contrary to
760 U2 (Sharpe et al. 2015; Shabaga et al. 2017). It can be mono and polymetallic. When monometallic, it is
761 characterized by pitchblende and sulfide minerals (pyrite, chalcopyrite, bravoite, sometime intergrown with
762 pitchblende), as observed at Contact. When polymetallic, it is characterized by pitchblende, sulfide minerals and Mo-
763 Ni-As-Co-Ag-Au mineralized fault zones, as observed at Contact, Andrew Lake and Kiggavik Main Zone.
764 Polymetallic U1 mineralization are rarer compared to monometallic mineralization. U1 is also characterized by the
765 presence of illite and sudoite.

766 U2 is hosted in wider, reddish oxidized f6 fault zones associated with stronger clay alteration of the host
767 rock, formed of illite and sudoite. This type of wide oxidized fault zones was well observed at Contact and Andrew
768 Lake, and also recognized at End and Kiggavik Main Zone. As already observed by Grare et al. (2018a) at Contact,
769 these oxidized faults are not always mineralized and fault cores that display strong clay alteration are usually not
770 mineralized. U mineralization is stronger in well-developed, moderately clay-altered damage zones. These
771 observations are in line with the classical view of fault zones (Chester and Logan 1986; Kim et al. 2004; Faulkner et
772 al. 2010) where fracturing and fluid flow are more important in damage zones than in core zones (Caine et al. 1996).

773 Mineralization U2 is mineralogically characterized by pitchblende and is monometallic. Rare sulfide
774 minerals (pyrite coated by pitchblende) are observed and relicts of ore minerals from previous stages can be
775 observed where U1 fault zones are reworked by U2 faults. Along with the hematization of the host rock, these

776 mineralogical differences highlight that U-bearing fluids had a different chemistry (although still being basinal
777 brines) than those of U1, with probably slightly more elevated fO_2 and pH (see Pourbaix diagram in [Romberger](#)
778 [1984](#)). The orientations of U2 faults do not necessarily reflect the orientations of the main fault that hosts the
779 deposit/prospect and which is better shown by non-mineralized oxidized faults (for example at Contact, Andrew
780 Lake, End and Bong), whereas mineralized faults display a more complex range of orientations, sometimes with
781 antithetic dip to the main fault (for example, NNW-SSE fractures at End, NE-SW to N-S fractures at Kiggavik).
782 These variable orientations are typical within damage zones linking main faults and has been described in a variety
783 of settings ([Kim et al. 2004](#); [Rotevatn and Bastesen 2014](#); [Fossen and Rotevatn 2016](#)). Overall, the differences
784 (fracture orientations, intensity of clay-alteration, reduced vs. oxidized fault zones, polymetallic vs. monometallic)
785 between mineralizing events U1 and U2 are here interpreted as the distinctive response of pre-existing and
786 reactivated faults to a change in the regional tectonic stress field, which induced a maturation of the fault zones, thus
787 a change in the fluids pathway, hence in contrasting fluid-rock interaction.

788

789 **Main post-ore alteration event f7**

790 The main post-ore (also called “late clay alteration”) fracturing event (f7) is characterized by fault zones
791 showing numerous narrow fault cores and strongly clay altered, dequartzified and completely bleached fault rocks.
792 illite is the only clay represented, sudoite were not observed under optical microscope and SEM. Fracturing/faulting
793 is spatially and temporally dissociated of U mineralization; however this stage has a significant impact on the
794 deposit’s 3D organization because these faults offset U orebodies with a significant dip-slip and a minor strike-slip
795 component. This is observed especially at Bong where the orebody is offset by W-E to WNW-ESE nearly dip-slip
796 normal faults, but also at End where the orebody is offset by NW-SE to NNW-SSE faults. Moreover, observed U1
797 and U2 fault zones are also less mineralized when they are crosscut by white-clay altered faults, indicating
798 remobilization of the U oxides at this stage. Only punctual relicts of pitchblende were observed in f7 fault zones (Fig.
799 5G). As this event corresponds to one of the latest fracturing stages, it is difficult to process oriented data in order to
800 retrieve the “true” faults orientation, as we are facing neof ormation and re-activation of fractures in complex and
801 polyphase fault zones. An ESE-WNW to NNW-SSE trend and a steep dip to the NW appear however to be the
802 dominant orientation of these faults in the Kiggavik area. Reactivation of faults during this stage is illustrated by NE-
803 SW white clay-altered faults at Contact, initially belonging to the f6 stage ([Grare et al. 2018a](#)). This observation that

804 most of the faults for this post-ore fracturing stage are inherited is consistent with models in which reactivation of
805 faults is often easier compared to neof ormation (e.g. [Pinheiro and Holdsworth 1997](#)).

806 Concerning mineralizing stage U3, even after careful review of drill core throughout the Kiggavik area, it
807 was not possible to precisely link redox fronts to specific fault zone, this mineralizing event appearing associated
808 with a weak reactivation of the fracture network without significant faulting.

809

810 **5.2 Reconstruction of the temperature of the mineralizing fluids**

811 **Chlorite geothermometry**

812 U0 is associated with chlorite crystallizing from 130-159°C up to 295-333°C, depending on the chosen
813 geothermometer used. The evaluation of iron valence, thus the amount of Fe³⁺, directly impacts the calculation of the
814 temperature and has always been an analytical challenge. However, Bourdelle and Cathelineau (2015) demonstrated
815 that the lower the temperature, the lower the impact of Fe³⁺ and a model based solely on Fe²⁺ is suitable in terms of
816 practicability and simplicity while still giving reliable results. In our study, the high temperatures (295-333°C)
817 obtained using Cathelineau (1988) and Jowett (1991) methods for dioctahedral chlorite of this stage appear
818 consistent with the presence of brannerite and the high Th content of pitchblende observed in U0. The incorporation
819 of thorium (Th⁴⁺) into the uraninite structure is indeed correlated with the temperature and is commonly observed in
820 metamorphic or magmatic uraninite (which form at T>300°C), contrary to hydrothermal uranium oxides ([Depiné et](#)
821 [al. 2013](#); [Mercadier et al. 2013](#); [Frimmel et al. 2014](#); [Cuney et al. 2015](#)) which form at T<300°C. The pre-Thelon
822 high-temperature dioctahedral chlorites cementing f0 fractures would have likely been altered to sudoite at a later
823 point, probably after the deposition of the Thelon Formation, by the circulation of Thelon-derived basinal brines thus
824 crystallizing lower temperature di-trioctahedral chlorites (~100-200°C). Such a fluid circulation is considered as
825 related to the formation of U1 and/or U2. Calculating the temperatures of formation of sudoite is not possible due to
826 their chemistry, precluding any comparison with temperatures obtained by illite geothermometry.

827

828 **Illite geothermometry**

829 Pre-U1/f5, white mica (also called pre-ore) that crystallized at low temperatures (~200-240°C) could either
830 represent early localized alteration along fault zones (f1) during development of the earlier Baker Lake and Wharton
831 basins (i.e., brittle faulting and illitization prior to QB event, [Grare et al. 2018b](#)), or circulation of diagenetic fluids

832 from the Thelon Basin (diagenetic quartz with temperatures of homogenisation of 100-160°C, peak diagenetic illite
833 crystallized at ca. 200°C, [Renac et al. 2002](#)). White micas synchronous with U1 and U2 returned temperatures of ca.
834 280-290°C, but slightly higher in the case of U1. These temperatures are higher than those typically obtained for
835 illite in the Athabasca Basin (220-280°C, [Ng et al. 2013](#); [Chu and Chi 2016](#)), which could indicate crystallisation of
836 illite and URU oxides at greater depth and/or an abnormally higher thermal gradient for the Thelon Basin compared
837 to the Athabasca Basin. A higher thermal gradient, linked to magmatism associated with emplacement of the
838 Kuungmi lavas at 1540±30 Ma ([Chamberlain et al. 2010](#)), i.e., the age proposed for the emplacement of U1 ([Sharpe
839 et al. 2015](#)), is our preferred hypothesis, as no geological process could here explain a major increase in depth.
840 Post-ore illite alteration, observed in f7 fractures, returned slightly higher temperatures of 290-350°C; this increase in
841 temperature could be linked to the emplacement of large volumes of magmas associated with the giant dike swarm of
842 the Mackenzie event. This event could have triggered the circulation of “hot” hydrothermal fluids shortly before
843 emplacement of the diabase dikes and “sealing” of faults, which would also be consistent with illite Ar-Ar ages
844 obtained at ca. 1300 Ma at End, Andrew Lake, Kiggavik Main Zone and Bong ([Ashcroft et al. 2017](#); [Shabaga et al.
845 2017](#); and others, see Fig. 21).

846

847 **Fluid inclusions**

848 Temperatures obtained based on microthermometry on type 2 FIPs (syn-/post-Thelon event) observed in
849 magmatic quartz range from 81°C to 240°C. These temperatures are comparable to those obtained in the Athabasca
850 Basin for diagenetic-hydrothermal fluids ([Richard et al. 2011, 2013](#)), and at End (100-200°C, [Chi et al. 2017](#)) from
851 fluid inclusions in quartz spatially associated with post-Thelon uraninite and calcite in the Kiggavik area.

852 The shift of ~100°C between temperatures given by fluid inclusions and those given by illite geothermometry
853 has already been reported in the Athabasca Basin by [Chu and Chi \(2016\)](#). Such a difference could be related to the
854 fact that the T_h measured for the fluid inclusions is usually lower than the temperature at the time of entrapment (i.e.,
855 at the time of fluid circulation). This difference could support a need for pressure correction of the fluid inclusion
856 data, although it would not completely explain the shift of temperature ([Richard et al. 2016](#)).

857

858 **5.3 Typology of U mineralization in the Kiggavik area**

859 **REE signatures**

860 The REE patterns of U oxides are considered as specific to each type of U deposit, directly reflecting their
861 conditions of formation (temperature, redox conditions, fluid composition, REE source(s); [Mercadier et al. 2011](#);
862 [Frimmel et al. 2014](#); [Alexandre et al. 2015](#)). REE patterns were not obtained for the magmatic U₀ because of the
863 small size of U oxides. However their high Th contents indicate rather high T conditions and magmatic/volcanic
864 fluids. The different U oxides from End (U1) and Andrew Lake (U2) display a bell-shape REE pattern centered on
865 Tb which is only typical of URU systems ([Bonhoure et al. 2007](#); [Mercadier et al. 2011](#); [Eglinger et al. 2013](#);
866 [Alexandre et al. 2015](#)). Such pattern was also obtained by [Fayek et al. \(2017\)](#) at Kiggavik Main Zone and indicates
867 unambiguously that U1 and U2 at Kiggavik area crystallized in rather identical physico-chemical conditions than
868 typical unconformity-related U oxides in the Athabasca Basin ([Pagel 1975](#); [Derome et al. 2005](#); [Richard et al. 2010](#);
869 [Martz et al. 2018](#)). Most of the samples present modified bell-shaped REE patterns compared to URU-type U oxides
870 from the Athabasca Basin, with enrichment in LREE, while concentrations of HREE remain the same (Fig. 16). This
871 modified bell-shape REE pattern, observed for U oxides located in remobilization fronts at Kiggavik area (Fig.15A),
872 was first described by [Mercadier et al. \(2011a\)](#) for U oxides in a remobilization front at Eagle Point U deposit in the
873 Athabasca Basin, and is linked to the interaction between URU-type UO₂ and low-T (<50°C) meteoric fluids. Such
874 modified spectrum is observed for U1 and U2 from the Kiggavik area (Fig. 16) and indicates that these initial URU-
875 type UO₂ were chemically affected by meteoric water. This is consistent with their reset U/Pb isotopic ages (younger
876 than 600 Ma; Fig. 17) and with macroscopic observations of redox front with goethite (AND-15-01-04 for example),
877 inferred to have formed in low-T and low-saline conditions ([Mercadier et al. 2011a](#)). Such alteration and/or
878 remobilization of brine-related uranium oxides by late low-T meteoric waters appears as a common and widespread
879 features in the Kiggavik area, based on published and present data ([Sharpe et al. 2015](#); [Shabaga et al. 2017](#)). The
880 impact of such process is probably moreover far more developed in the Kiggavik area compared to the Athabasca
881 Basin.

882 The shape of the REE patterns for the sample 85W-10-04 (85W) is quite different compared to the
883 traditional URU bell-shaped pattern: the pattern displays comparable positive slope for LREE and negative slope for
884 HREE, but is centered on SM and the REE concentrations are increased by a factor of 10 (Fig. 15C). A similar shape
885 was only described for one uranium oxide in Zambia ([Eglinger et al. 2013](#)), which was considered as URU-type.
886 Such a pattern is however not characteristic of URU oxides, as observed for all deposits in the Athabasca basins
887 ([Mercadier et al. 2011b](#); [Alexandre et al. 2015](#)). The REE composition and the age (post-Mackenzie dike) of this U

888 oxide, indicate that the conditions for the crystallization of this mineralization were somewhat different than U1 and
889 U2 U oxides. At the moment no conclusions can be made about the origin of this uranium oxide.

890 To summarize, when unaltered by post-crystallization alteration (End), U1 and U2 display REE patterns
891 typical of URU-type uranium oxides from the Athabasca Basin. Such observation indicates that the physico-chemical
892 conditions and the mineralizing fluids for the formation of U mineralization for the two districts were similar. U1 and
893 U2 crystallized thus in URU-type conditions. These uranium oxides were strongly affected by late alteration related
894 to meteoric waters which significantly changed their initial chemical composition and reset their U/Pb isotopic age.
895 This alteration ultimately favored their dissolution and reprecipitation as U3 in redox front.

896

897 **Fluid inclusion compositions**

898 In contrast to what is observed in Athabasca basement ([Mercadier et al. 2010](#); [Potter and M. Wright 2015](#);
899 [Martz et al. 2017](#)) no carbonic fluid inclusions were observed here. Dense arrays of dark monophasic FIs are very
900 similar to trends of retro-metamorphic fluid inclusions observed in the Athabasca Basin ([Mercadier et al. 2010](#),
901 [Martz et al. 2017](#)), bearing mainly CO₂, with some other gases,. The absence of CO₂ and CH₄ in our case could be
902 explained either by the lack of graphite-rich lithologies and fault zones in the Kiggavik area, which are sources of
903 CO₂ and CH₄ observed in retro-metamorphic FIs and in some aqueous FIs in Athabasca ([Martz et al. 2017](#)); or by a
904 demixion at great depth that would have induced trapping of CO₂-rich liquid phase. This last hypotheses could be
905 linked to an epithermal event, which has been characterized in/close to the Kiggavik area ([Turner et al. 2001](#); [Grare
906 et al. 2018a, b](#)). Such event, considered to be linked to the QB has not been described in the vicinity of the Athabasca
907 Basin. Therefore, considering that type 1 FIPs are crosscut by type 2 FIPs, it is much more likely that these trends of
908 vapor rich FIs characterize the QB event.

909

910 Aqueous biphasic and triphasic fluid inclusions observed at 85W and Contact display salinity between 24 to
911 39wt.% NaCl, and homogenization temperatures between 81 and 240°C. Temperatures and salinity obtained for
912 aqueous fluid inclusions are comparable to those obtained by [Chi et al. \(2017\)](#) at End. Temperatures and salinity are
913 higher compared to those obtained by [Renac et al., \(2002\)](#) in the Thelon sandstone out of mineralized zones: 100-
914 160°C, ca. 17wt.% NaCl. [Chi et al. \(2017\)](#) also observed the absence of gases other than H₂O, H₂ or O₂, for primary
915 monophasic fluid inclusions in hydrothermal quartz. These observations, along with melting temperature of NaCl

916 higher than homogenization temperatures and the fact that most of FIs do not freeze, indicate that aqueous biphasic
917 and triphase fluid inclusions are representative of a high salinity Ca-rich brines (Bodnar 2003; Derome et al. 2005).
918 Such brines have been observed throughout the Athabasca Basin for all the studied U deposits. They are thought to
919 be primarily derived from evaporated seawater and have variably mixed with with sodic brines of similar origin
920 (Richard et al. 2011a, 2013, 2014). Ca-rich brines are supposed to derive from interaction with the basement
921 (Derome et al. 2005; Mercadier et al. 2010; Richard et al. 2010, 2016; Martz et al. 2018). In this study, we observed
922 only calcic brines in FIPs, while Chi et al., (2017) observed sodic and calcic brines in hydrothermal quartz veins. The
923 sole occurrence of calcic brines and the absence of the sodic brines in some parts of the Kiggavik area would reflect
924 a significantly long interaction of the brine with basement rocks. The slightly higher temperatures measured for the
925 calcic brines in the Thelon Basin compared to the Athabasca Basin, in line with the temperatures calculated for the
926 illite, could indicate a higher thermal gradient or a deeper percolation of brines within the basement. This could have
927 well been the case in the Kiggavik area where the studied mineralized samples were located at a still unconstrained
928 depth in the basement rocks, at the time of brine circulations (1500-1267 Ma), below a formerly overlying and now
929 eroded cover of unknown thickness (Baker Lake and Thelon sediments).

930 Water-dominated fluid inclusions display similar concentrations compared to Ca-rich aqueous FIs from the
931 McArthur River and Cigar Lake U deposits in the Athabasca Basin (Richard et al. 2010, 2012, 2016; Martz et al.
932 2018), being extremely rich in metals like U, Zn, Rb, Sr, Cs, Ba, Pb. Boron was not detected in FIs of the Kiggavik
933 area which could be linked to the lack of Mg-tourmaline in this zone compared to the Athabasca Basin. The present
934 data indicate therefore that metal-rich (in particular U-rich) and highly-saline basinal brines circulated in the
935 basement rocks of the Kiggavik area and were at the origin of the formation of U1 and U2 at ca. 1500-1275 Ma.
936 These brines are rather identical to those linked to the formation of URU-type deposits in the Athabasca Basin. H₂O
937 vapour, H₂ and O₂ were observed in some monophasic and aqueous fluid, indicating radiolysis of H₂O in presence of
938 U (Dubessy et al. 1988; Richard 2017).

939

940 **5.4 Timing of mineralizing events**

941 The pre-Thelon mineralizing event U0 is likely associated with peralkaline magmatism of the Dubawnt
942 minette suite. Absolute age-dating was not possible on our samples due to the small size of U-oxides, but ages of ca.

943 1830 Ma were obtained on pitchblende within the Baker Lake Basin by (Miller and LeCheminant 1985) and Bridge
944 et al. (2009) (Fig. 21).

945 Observations on U1 show that fractures associated with this mineralizing event (f5) crosscut dolomite veins
946 formed by basinal brines derived from the Thelon Basin (Riegler et al., 2013). F6 faults constraining U2 crosscut
947 sandstones of the Thelon Formation (Grare et al. 2018a). Absolute ages obtained for U1 are between 1293 ± 08 Ma
948 and 1187 ± 20 Ma for End deposit and 354 ± 47 Ma at Andrew Lake. The dated U2 samples display ages at 565 ± 38 Ma
949 and 345 ± 19 Ma at Andrew Lake. However cross-cutting relationships indicate that these two stages occurred prior to
950 the emplacement of the Mackenzie diabase dikes at 1267 ± 2 Ma (LeCheminant and Heaman 1989; Heaman and
951 LeCheminant 1993). U1 and U2 mineralization probably occurred between 1530 and 1267 Ma, interval previously
952 proposed for the crystallization of hydrothermal UO_2 in the area (Sharpe et al. 2015; Chi et al. 2017). As previously
953 proposed, the younger ages obtained at Andrew Lake (ca. 550 and 350 Ma) do reflect a reset of the U-Pb system of
954 U oxides at these periods of time. This would have occurred through renewed circulation of meteoric and oxidizing
955 fluids during two distinct events precisely dated at 550 Ma and 300 Ma. Such alteration of U0/U1/U2 and alteration
956 by low-T meteoric fluids led ultimately to crystallization of U3 oxides (U3) along redox fronts at the same periods.
957 A specific but unconstrained event of crystallization of a uranium oxide was active at End at ca. 1073 Ma. The
958 compilation of the isotopic U-Pb ages and trace element concentrations for the different mineralization observed in
959 the Kiggavik area indicate that the U system was polyphase and that U was mobilized during more than 1.5 billion
960 years. Such extremely long duration of U events is similar to what has been observed in the Athabasca Basin.
961 Additionally, these similarities between the Athabasca and Thelon Basins demonstrate that they had rather close
962 evolution through time in terms of U systems, moving from relatively high-T magmatic/metamorphic conditions
963 (U0) before 1750 Ma, to moderate-T hydrothermal conditions with basinal brines (U1 and U2) between 1530 to 1270
964 Ma to low-T meteoric mineralization (U3) after.

965

966 **5.5 Tectonic stresses driving fracturing events in the Kiggavik area**

967 Fig. 22 displays a synthesis of all oriented mesostructural data that exhibit kinematic indicators. Data are
968 separated into macro/meso-scale observations (field, drill core, Fig. 22A) and micro-scale observations (solution
969 seams and FIPs, Fig. 22B). This allowed to tentatively derive the local tectonic stress prevailing during
970 fracturing/faulting events.

971 Kinematic indicators associated with f0/U0 are represented by the solution seams oriented NNW-SSE (Fig.
972 22B). This likely indicates a WSW-ENE trending σ_1 consistent with what was proposed by Hadlari and Rainbird
973 (2011). However, the number of oriented data is very low which makes it hard to conclude on the tectonic stress
974 even if the result obtained makes sense.

975
976 F2 stepped quartz veins and mode-I quartz veins related to U1 indicate a WNW-ESE trending σ_1 . This direction
977 is also consistent when considering the supposed post-Thelon quartz veins described by Chi et al. (2017). This
978 observation would mean that a regional strike-slip stress regime with a WNW-ESE trending σ_1 and NNE-SSW
979 trending σ_3 possibly prevailed from the pre-Thelon stage (i.e., when the main Thelon fault developed) to a post-
980 Thelon stage, ultimately until precipitation of U1 from basinal brines, as stepped calcite veins displaying W-E to
981 NW-SE directions would have developed under a similar tectonic stress. Such a stress regime is consistent with type
982 1 FIPs and type 2 FIPs that display dominant WNW-ESE trends indicating a NNE-SSW to NE-SW trending σ_3
983 during the emplacement of the QB (Fig.23). This WNW-ESE trending σ_1 is further consistent with the dextral slip
984 component along E-W to ENE-WSW trending fault relay zones in the QB. This is in agreement with the
985 observations made by Anand and Jefferson (2017) who concluded that re-activation of ENE-WSW, N-dipping
986 extensional faults (such as the TF or the JSF), formed initially during the deposition of the Baker Lake and Wharton
987 Groups, occurred under a \sim N110-140° trending σ_1 . We propose that this local tectonic stress is related to the Thelon-
988 Taltson (2100-1930 Ma) and Trans-Hudsonian orogenies (1900-1800 Ma), when the whole Churchill craton was
989 under roughly E-W compression; however at 1500-1300 Ma (U1 mineralizing stage), the Racklan orogeny (ca. 1600-
990 1380 Ma; Cook 1992; Cook and MacLean 1995; Thorkelson 2000), to the west of the Kiggavik area) would be at the
991 origin of the WNW-ESE shortening, as proposed by Anand and Jefferson (2017).

992 F6 neoformed and reactivated hematized fault zones underwent either sinistral and/or reverse movements
993 (Fig. 22A). Sinistral reactivation of the ENE-WSW JSF overprinted the dextral motion on this fault that offsets the
994 Schultz Lake Intrusive Complex (map scale observation, Fig. 2). These observations, together with the NE-SW
995 crack-seal calcite (Ca2) veins (f6) coated with U2 spherulitic pitchblende support a local stress regime with NE-SW
996 to ENE-WSW trending σ_1 and NW-SE to NNW-SSE trending σ_3 for the tectonic event associated with U2. This
997 stress regime accounts for the secondary NE-SW to ENE-WSW trends of type 2 FIPs (Fig. 22B) within magmatic

998 quartz from 85W associated to a second episode of circulation of basinal brines. The regional meaning of this stress
999 regime still remains poorly understood.

1000 Finally, the post-U1 and U2 faults (f7) which drove hot (~300°C), likely acidic fluids that strongly clay
1001 altered host rocks and offset U mineralisation, display two main trends: WNW-ESE with dextral to dextral-normal
1002 slip component and NNW-SSE with sinistral slip component. Combined with the dominant dip-slip component
1003 observed on some WNW-ESE faults observed at Bong, we infer a transtensional stress regime with σ_1 trending NW-
1004 SE and σ_3 trending NE-SW. This faulting event would be responsible for down-drop offset of the U orebodies at
1005 Bong, End and Kiggavik Main Zones (example in Fig. 13D). The NW-SE trending σ_1 and NE-SW trending σ_3
1006 would also account for the latest sinistral offset of the Judge Sisson fault and Thelon fault by NNW-SSE faults,
1007 observed in the field and on aeromagnetic maps (Tschirhart et al. 2017). Such NNW-SSE faults were likely reopened
1008 during the emplacement of the Mackenzie dikes. The inferred NW-SE trending σ_1 and main NE-SW trending σ_3 is
1009 consistent with a regional-scale compressional stress active on the southeast margin of the Canadian Shield (Hou et
1010 al. 2010) at ca. 1270 Ma. Weak reactivation of the fracture network occurred at ca. 500 and 300 Ma, driving
1011 circulation of meteoric fluid, remobilizing and/or altering previously formed U oxides and precipitating U₃. Such
1012 reactivation is probably linked to a far field stress associated with the breakup of West Rodinia supercontinent
1013 (ca.500 Ma, Bond et al. 1984) and the Appalachian Orogen (ca. 350 Ma, Hatcher, 2002), and is also observed in
1014 Athabasca (Dieng et al. 2013).

1015 The structural evolution proposed in this study differs from the Riedel shear system of Anand and Jefferson
1016 (2017), although not incompatible with it. They proposed that the entire fracture network evolved mainly under a
1017 ~N110-N140 trending σ_1 from ca. 1800 Ma to 1540 Ma. In their model, the different fault zones (ENE-WSW,
1018 NNW-SSE, NS, NE-SW, E-W) are part of a Riedel system (i.e., analogue to the P, T, X, R', R shears).

1019

1020 **6. Metallogenic model of the Kiggavik area**

1021 The combination of all structural, mineralogical, fluid inclusion, dating and geochemical characteristics of the
1022 different U deposits and prospects from the Kiggavik area allows proposing for the first time a structurally-controlled
1023 metallogenic model of U mineralization in the Kiggavik area. The main fracturing events, their associated tectonic
1024 stress and fracture network evolution are presented in synthetic block diagrams (Fig. 23 to 27) for Bong, Kiggavik

1025 Main Zone (both located on ~ENE-WSW faults), Andrew Lake and Contact (both located on ~NE-SW faults),
1026 together with the associated types of fluids, conditions and timing of their circulation and related mineralization type.
1027

1028 **Pre-Thelon Basin fracturing events and the first stage of U mineralization**

1029 **(f0, U0):** the first U mineralizing event, characterized for the first time in this study, was observed in all
1030 major deposits in the Kiggavik area. Hydrothermal rutile cementing microfractures and coated with pitchblende at
1031 Contact ([Grare et al. 2018a](#)) are relicts of this first mineralizing stage. F0/U0 is crosscut by quartz veins of the QB
1032 (formed at ca. 1750 Ma) and is usually better preserved in deep-seated, less altered parts of the deposits (like in End,
1033 footwall of the QB). Major faults (ALF, JSF, MZF, probably TF) were active at that time (Fig. 23A), probably under
1034 a WSW-ENE σ_1 and NNW-SSE σ_3 (Fig. 23B), and mineralized.

1035 Analyzed U-bearing minerals for this stage under EMPA come from End only; however, the same
1036 chemistry (several percent of thorium) was also described by Weyer ([1989](#)) at Kiggavik Main Zone. Thorium content
1037 in pitchblende and brannerite characterizes a relatively high temperature fluid (>400°C), along with presence of
1038 rutile and temperatures returned by chlorite geothermometer (>350°C). Mineralized microfractures and the
1039 characteristic solution seams were also described by Miller, ([1980](#)) and Lecheminant et al. ([1979](#)) in their study of
1040 the Kazan Fall U mineralization, and like unaltered chlorite observed within the cement of the mineralized
1041 microbreccia in the Kiggavik area, the chlorite in the Kazan Fall microbreccia returned temperatures around 300-350
1042 °C.

1043 This U mineralization event likely occurred in the Thelon-Baker Lake area at the end of the Trans-
1044 Hudsonian orogeny (ca. 1830 Ma), in response to retro-arc extension with deposition of the Baker Lake formation
1045 and emplacement of U-rich peralkaline magmas of the Dubawnt igneous suite ([Cuney 2014; Cuney et al. 2015](#)).
1046 Such mineralizing event is plausible in the Kiggavik area even as located far from the formations of the Baker Lake
1047 Basin, since a breccia pipe of the Christopher Island formation (ca. 1827 Ma) was observed in the eastern part of the
1048 Kiggavik area, along with ultrapotassic minette and bostonite dikes ([Anand and Jefferson 2017](#)) of the Dubawnt
1049 igneous suite (ca. 1830 Ma). These rocks are enriched in U ([LeCheminant et al. 1987; Miller and Blackwell 1992;](#)
1050 [Peterson et al. 2011](#)) and could also represent a good source of U.

1051 This mineralizing event, that predates deposition of the Thelon Basin, is the first U mineralizing event in the
1052 Kiggavik area and is likely of magmatic/volcanic origin. Mineralisation occurred within major fault zones and form

1053 the first significant “stock” of U oxides in the Kiggavik area. This stock will be later remobilize to form the younger
1054 mineralization.

1055
1056 **(QB, f2):** Intense quartz brecciation related to the QB event occurred along major fault zones in the
1057 Kiggavik area and also South of the Kiggavik area (Baudemont and Reilly 1997; Turner et al. 2001). FIs in quartz of
1058 the QB were characterized by several authors (Pagel 1995; Turner et al. 2001; Riegler 2013; Chi et al. 2017; this
1059 study). Most of the quartz belongs to the QB event, as characterized by cathodoluminescence and textural
1060 observations on quartz by Grare et al. (2018b). They are characterized by high temperature/low salinity fluids (Pagel
1061 et al. 1995). They are also characterized by trends of monophasic FIs in concentric zones of quartz. QB crosscut
1062 Nueltin granites of the ca. 1750 Ma Kivalliq igneous suite and predates deposition of the Thelon Basin. Textural
1063 characteristics and fluid inclusion data from different locations in the Kiggavik area attest for a regional magmatic
1064 event associated with massive and likely repeated influx of silica rich fluids of likely igneous origin (Grare et al.
1065 2018b). This event is therefore likely linked to magmatism of the Kivalliq igneous suite dated at ca. 1750 Ma. Fluid
1066 circulation was focused along major faults and relay zones (Fig. 24A), silicifying/overprinting previously formed
1067 fault rocks. QB formed under a WNW-ESE trending σ_1 and NNE-SSW trending σ_3 (Fig 24B). This
1068 silicification event likely controlled, at least partly, later fracturing and fluid circulation, depending on the thickness
1069 of the quartz breccia: U mineralization is usually stronger in the hanging wall of the structure (e.g., for End and
1070 Contact).

1071

1072 **(Syn?) Post-Thelon Basin fracturing events: second and third stages of URU-type U mineralization**

1073 **(f5, U1):** this stage is characterized by monometallic to polymetallic mineralization within reduced narrow
1074 fault zones (Fig. 25A). Illite is the main alteration product but sudoite was observed in altered mineralized fault rocks
1075 at Jane (Miller 1997), End (Lida 1997), Bong, (Riegler et al. 2014; Sharpe et al. 2015) and Kiggavik Main Zone
1076 (Pacquet 1993a). APS, synchronous with U mineralization, were observed at 85W (this study), and by Riegler et al.
1077 (2016) at Bong.

1078 U1 postdates quartz veins and dolomite veins precipitated from typical basin-derived and highly saline brines
1079 (Chi et al. 2017; and Riegler, 2013; respectively), and is synchronous with the first generation of calcite veins. Fluid
1080 inclusions in calcite at End were studied by Chi et al. (2017). This calcite was not characterized under

1081 cathodoluminescence, but it is probable that Chi et al. (2017) studied fluid inclusions of the first generation of calcite
1082 (Ca1 as defined in our study) as veins of the second generation are usually too thin to study fluid inclusions. This
1083 first generation of calcite also precipitated from Thelon-derived highly saline basinal brines. This synchronicity also
1084 allows deducing that fracturing stage f5 associated with U1 formed in response to a stress regime with WNW-ESE
1085 σ_1 and NNE-SSW σ_3 (Fig. 22B).

1086 ENE-WSW, N-dipping extensional faults formed earlier during the deposition of the Baker Lake and Wharton
1087 Groups were reactivated at that stage with a dextral-normal kinematics, favoring the circulations of the NaCl-rich
1088 basinal brines from the Thelon Basin to the basement rocks and the probable formation of CaCl₂-and U-rich
1089 mineralizing brines (U1). The oldest ages were obtained by Farkas et al., (1984) and Sharpe et al., (2015) at 1403±10
1090 Ma and 1520±79 Ma respectively. Local heating and circulations of hydrothermal fluid associated with emplacement
1091 of the Kuungmi lavas at ca. 1540±30 Ma (Chamberlain et al. 2010) are described as one possible first event of URU-
1092 type mineralisation in the Kiggavik area (Sharpe et al. 2015). This age was observed throughout the Thelon-Baker
1093 Lake area ((Turner et al. 2003; Bridge et al. 2013)). Ages at 1500-1400 Ma are comparable to ages obtained on
1094 oldest URU mineralization in Athabasca (1514±18 Ma, Cumming and Krstic 1992; 1519±22 Ma, Fayek et al. 2002;
1095 1540±19 Ma, Alexandre et al. 2009). The time frame defined by age-dating studies and the reconstructed stress
1096 regime are consistent with the Racklan orogeny (ca. 1600-1380 Ma; Cook 1992; Cook and MacLean 1995;
1097 Thorkelson 2000).

1098 Minerals that fingerprint highly saline basinal brines (sidoite, APS), fluid inclusion characteristics (high salinity,
1099 Ca-rich, Th between 100 and 220°C), and the REE bell shape pattern of uranium oxides, along with the timing of the
1100 mineralizing event (post-Thelon formation), allow concluding that U1 precipitated from Thelon (or Baker Lake)-
1101 derived basinal brines, and thus is of unconformity-related type, like the U deposits in the Athabasca Basin.

1102
1103 **(f6, U2):** this stage is characterized by monometallic mineralization within oxidized wide fault zones (Fig.
1104 26A), formed under a ~NE-SW trending σ_1 and ~NW-SE trending σ_3 (Fig. 26B). This fracturing event formed new
1105 fractures while likely reactivating the complex, pre-existing fracture network of the Kiggavik area. The response of
1106 the fracture network to the tectonic stress was obviously different depending on its orientation: at Andrew Lake and
1107 Contact, hematized and mineralized damage zones of faults trending NE-SW are well developed in contrast to those
1108 associated within ENE-WSW fault zones of the Kiggavik Main Zone deposit (Fig. 26A).

1109 APS minerals were observed in oxidized fault zones at Contact (Grare et al. 2018a) and 85W (this study),
1110 and sudoite associated with illite, were described, at Contact (Grare et al. 2018a), Jane (Miller 1997), Kiggavik Main
1111 Zone (Hasegawa et al. 1990), End (Lida 1997) and Andrew Lake (Hasegawa et al. 1990; Pacquet 1994). This
1112 monometallic mineralizing stage was also described at Andrew Lake (Shabaga et al. 2017).

1113 Like U1, U2 formed in relation to the circulations of basinal brines derived from the Thelon Basin, and is of
1114 unconformity-related type. Relative chronology places the formation of U2 after the deposition of the Thelon
1115 Formation but before emplacement of the Mackenzie dikes, hence bracketed between 1500 and 1267 Ma. Note
1116 however that no available absolute age dating (ca. 1000 Ma, Shabaga et al. 2017; 550-300 Ma, Shabaga et al. 2017;
1117 this study) supports this timing. One likely explanation is related to alteration and reset/precipitation of U-oxides
1118 that accounts for the modified REE bell-shape pattern for U2 oxides (Fig. 16).

1119 Concerning URU-type mineralization in the Kiggavik area, two main differences with the Athabasca Basin
1120 are the absence of magnesio-foitite (Mg-tourmaline also called dravite, Mercadier et al. 2012) and a Mg-rich sudoite
1121 rather than a Al-Mg sudoite. The absence of Mg-foitite is consistent with the non-detection of Boron in the brines of
1122 the Kiggavik area (Fig. 19), a major difference with the brines in the Athabasca Basin (Richard et al. 2016). Potential
1123 U sources for U1 and U2 are various and could be the metamorphosed epiclastic rocks of the Puqik Lake formation
1124 (Johnstone et al., 2017), rhyolitic flows of the Wharton group (Blake 1980; Peterson et al. 2015), fluorapatite-
1125 cemented breccia at the base of the Thelon formation (Davis et al. 2011), ultrapotassic minette and bostonite dikes
1126 (LeCheminant et al. 1987; Miller and Blackwell 1992; Peterson et al. 2011) of the Dubawnt igneous suite (ca. 1830
1127 Ma), U-rich pegmatite of the Kivalliq igneous suite (Scott and Peterson 2012) but more specifically the previous U
1128 mineralizing stage (U0). U0 is observed in significantly mineralized brecciated rocks, and would have been an
1129 efficient and easily available source of U for basinal brines during their circulations in U0-mineralized basement
1130 structures. The presence of a pre-Thelon-basin source of uranium is comparable to what is described near the
1131 Athabasca basin: volcanic and metasomatic uranium in the western margin (Dieng et al. 2013, 2015) or magmatic
1132 and metamorphic uranium described in the eastern margin (Mercadier et al. 2013).

1133
1134 **(f7):** The last main fracturing event is characterized by strongly desilicified, illitized and bleached fault
1135 rocks, also reworking/offsetting previously formed ore bodies along E-W and NW-SE faults (Fig. 27A).
1136 Emplacement of a mantle plume triggered the emplacement of Mackenzie mafic dikes swarm at ca. 1267 ± 2 Ma.

1137 Such magmatism intruded the pre-existing extensional fractures which were active under a NE-SW trending σ_3 (Fig.
1138 27B). This magmatic event is likely at the origin of circulation of hot (~300°C), probably acidic, fluids during the f7
1139 fracturing stage. This timing is supported by age dating on illite (K-Ar and Ar-Ar) showing an alteration event at ca.
1140 1300 Ma (Fig. 21) at End, Andrew Lake, Bong and Kiggavik Main Zone. The circulation of fluids linked to the
1141 extensional event and to the magmatism likely occurred at ca. 1330-1265 Ma, considering age dating of uranium
1142 oxides and of MacKenzie dikes. This tectonic/magmatic event ended by the emplacement of the MacKenzie diabase
1143 dikes which crosscut orebodies and “seal” the affected faults; they are almost unaltered and fractured. Along these
1144 dikes, thermal effect would have locally remobilized and reprecipitated U oxides, resetting the U/Pb isotopic system.
1145 Such strong clay alteration has previously been described as synchronous with U alteration (Hasegawa et al. 1990;
1146 Riegler et al. 2014; Shabaga et al. 2017), but this study shows that white clay illitization post-date U0/U1/U2.

1147

1148 **Post Mackenzie dikes minor fracturing events and U mineralization/precipitation**

1149 Several ages were previously obtained at Kiggavik area on U oxides at ca. 1000 Ma and ca. 800 Ma (Fig.
1150 21). These ages, not measured in the present study, could correspond to far-field tectonic activity associated with the
1151 Grenville orogeny (Gordon and Hempton 1986) and the initial rifting event of Rodinia, for example (Badger et al.
1152 2010; McClellan and Gazel 2014). It is to date unknown whether these two events have led to the formation of new
1153 mineralization or simply caused alteration and reset of existing mineralization. Younger ages at ca. 550 Ma and ca.
1154 350 Ma correspond to reset of the U-Pb isotopic systems of U1 and U2 but also to their dissolution and precipitation
1155 of U3. The specific modified bell shape pattern marks the alteration and remobilization of the URU-type U oxides by
1156 low-T meteoric fluids, which is consistent with the observation of goethite in these mineralized samples, a low
1157 temperature iron oxide (in contrary to hematite observed for stage U2). U3 occurred at a post-Mackenzie stage and
1158 does not belong to the unconformity-related type. It likely happened when a significant thickness of Thelon Basin,
1159 Wharton Basin and/or basement rocks was definitely eroded, letting supergene, low-temperature oxidizing fluids
1160 circulating through the fracture network and remobilizing U.

1161

1162 **7. Conclusions**

1163 This paper proposes for the first time an integrated structural and metallogenic model of the Kiggavik area based on
1164 a multi-scale and multi-disciplinary approach.

1165 The main conclusions of the study are the followings:

1166 - The Kiggavik area is characterized by a polyphased fracture network that evolved in a brittle style from ca.
1167 1830 Ma until the emplacement of the Mackenzie dikes at ca. 1270 Ma. The pre-Thelon U0 mineralization and
1168 QB event (f2 at ca. 1750 Ma) highlight the importance of magmatic-related fracturing, fluid circulation and
1169 mineralisation controlling subsequent location of URU-type U deposits.

1170 - This stage of fracturing and U0 mineralization is likely linked with the peralkaline magmatism of the
1171 Dubawnt minette suite at ca. 1830 Ma. Such mineralized breccia constituted a first significant stock of U
1172 available for reconcentration through later circulation of oxidized basinal brines. This first mineralization is of
1173 magmatic-related type.

1174 - After deposition of the Thelon and Lookout Point formations, a first circulation in basement structures of
1175 highly-saline basinal brines derived from the Thelon Basin occurred under a WNW-ESE σ_1 and NNE-SSW σ_3 .
1176 This event precipitated U1 in fault relay zones (End, Kiggavik Main Zone) and/or in zones where faults were
1177 the Quartz Breccia was present (e.g., Bong, Contact, Andrew Lake, End). Fracturing and renewed circulations of
1178 basinal brines occurred under a NE-SW σ_1 and NW-SE σ_3 with transpressional reactivation of the previously
1179 formed fault/fracture network to form U2. U mineralization preferentially developed in moderately altered
1180 damage zones of fault zones. U1 and U2 mineralization belong to the unconformity-related type, as
1181 characterized in the Athabasca Basin. They formed before the MacKenzie dike event, i.e. between 1530 and
1182 1270 Ma, in relative similar conditions and timing than URU-type mineralization in the Athabasca Basin.

1183 - Circulations of basinal brines occurred through a fault/fracture network that evolved though time in
1184 response to the changing local/far-field tectonic stress. This caused changes in the fluid pathways hence in fluid-
1185 rock interaction (changing characteristics of the fluid such as fO_2 and pH) and led to slightly different U
1186 mineralization (polymetallic reduced U1 vs monometallic oxidized U2).

1187 - The initial NaCl-rich basinal brines reacted with basement rocks to form CaCl₂- and metal-rich
1188 mineralizing brines at the origin of U1 and U2. The chemistry and physico-chemical characteristics of the
1189 CaCl₂-rich brines in the Kiggavik area are similar to those measured for mineralizing CaCl₂-rich brines in the
1190 Athabasca Basin, indicating rather common processes for the two sedimentary basins and related U
1191 mineralization.

1192 - Late faulting and associated strong clay alteration and bleaching of the host rock occurred at ca. 1300 Ma
1193 in response to local NE-SW extension and regionally NW-SE far-field σ_1 . This fracturing event, barren of U
1194 mineralization, caused the offset of previously formed orebodies and accounts for the formation in the Kiggavik
1195 area of strongly altered areas disconnected of any U mineralization.
1196 - Post Mackenzie dikes weak reactivation of the fracture network induced circulation of low-T meteoric fluids,
1197 remobilizing/precipitating U oxides (U₃) and altering their geochemical signature at two different times, ca.
1198 550 and 350 Ma, presumably linked to changing far-field stress associated with continent break-up and
1199 assembly. Other events of fluid circulations likely happened at ca. 1000 and 700 Ma in relation similar process.
1200 A mineralization event with specific physico-chemical characteristics was dated at 1073 Ma, its origin and
1201 related processes remain unknown.
1202 - U mineralization in the Kiggavik area are therefore of a mixed type, combining magmatic, URU type and
1203 meteoric-related (“roll-front”) mineralization, rather than being purely of URU type, like what is actually
1204 described in the Athabasca Basin. This area demonstrates more than 1.5 billion years of uranium mobility.

1205

1206 **Acknowledgments**

1207 The authors thank Orano and Orano Canada for the full financial support and access to the Kiggavik camp and
1208 exploration data. We thank Orano for the permission to publish these results. Special thanks to Dr. Kathryn Bethune
1209 for her in-depth review, senior petrographist M. Brouand, senior geoscientist D. Quirt, ARC geologists R. Zerff, R.
1210 Hutchinson, K. Martin, and D. Hrabok for their help and enriching discussions during field work and data
1211 interpretation. Thanks to P. Martz for his help on studying fluid inclusions. We are grateful to N. Bouden, J.
1212 Villeneuve and E. Deloule at CRPG (Vandoeuvre-lès-Nancy) for SIMS analyses, and to A. Lecomte and O. Rouer at
1213 SCMEM (GeoRessources, Vandoeuvre-lès-Nancy) for data acquisition. Thanks to J.M. Vergeau and P-C. Guiollard
1214 at Bessines-sur-Gartempe Areva site for help and access to historical data and samples.

1215

1216 **References**

1217 Alexandre P, Kyser K, Layton-Matthews D, et al (2015) Chemical Compositions of Natural Uraninite. *Can Mineral*
1218 53:595–622. doi: 10.3749/canmin.1500017
1219 Alexandre P, Kyser K, Thomas D, et al (2009) Geochronology of unconformity-related uranium deposits in the

- 1220 Athabasca Basin, Saskatchewan, Canada and their integration in the evolution of the basin. *Miner Depos*
1221 44:41–59. doi: 10.1007/s00126-007-0153-3
- 1222 Allan MM, Yardley BW, Forbes LJ, et al (2005) Validation of LA-ICP-MS fluid inclusion analysis with synthetic
1223 fluid inclusions. *Am Mineral* 90:1767–1775
- 1224 Anand A, Jefferson CW (2017) Reactivated fault systems and their effects on outcrop patterns of thin-skinned early
1225 thrust imbrications in the Kiggavik uranium camp, Nunavut
- 1226 Ashcroft GS, Fayek M, Quirt D, et al (2017) The geochemistry and geochronology of the End Deposit, NE Thelon
1227 region, Nunavut Canada: An insight to the Athabasca basin's closest relative. 1
- 1228 Badger RL, Ashley KT, Cousens BL (2010) Stratigraphy and geochemistry of the Catocin volcanics: Implications
1229 for mantle evolution during the breakup of Rodinia. In: Tollo RP, Bartholomew MJ, Hibbard JP, Karabinos
1230 PM (eds) *From Rodinia to Pangea: The Lithotectonic Record of the Appalachian Region*. Geological Society
1231 of America
- 1232 Battaglia S (2004) Variations in the chemical composition of illite from five geothermal fields: a possible
1233 geothermometer. *Clay Miner* 39:501–510. doi: 10.1180/0009855043940150
- 1234 Baudemont D, Reilly B (1997) *Thelon Project - 1997: Reconnaissance Mapping and Structural Geology*. 43
- 1235 Benedicto A, Schultz RA (2010) Stylolites in limestone: Magnitude of contractional strain accommodated and
1236 scaling relationships. *J Struct Geol* 32:1250–1256. doi: <https://doi.org/10.1016/j.jsg.2009.04.020>
- 1237 Blake DH (1980) Volcanic rocks of the Paleohelikian Dubawnt Group in the Baker Lake - Angikuni Lake area,
1238 District of Keewatin, N.W.T., bulletin 3
- 1239 Bodnar RJ (2003) Introduction to aqueous-electrolyte fluid inclusions. *Fluid inclusions Anal Interpret* 32:81–100
- 1240 Bond GC, Nickeson PA, Kominz MA (1984) Breakup of a supercontinent between 625 Ma and 555 Ma: new
1241 evidence and implications for continental histories. *Earth Planet Sci Lett* 70:325–345. doi:
1242 [https://doi.org/10.1016/0012-821X\(84\)90017-7](https://doi.org/10.1016/0012-821X(84)90017-7)
- 1243 Bonhoure J, Kister P, Cuney M, Deloule E (2007) Methodology for Rare Earth Element Determinations of Uranium
1244 Oxides by Ion Microprobe. *Geostand Geoanalytical Res* 31:209–225. doi: 10.1111/j.1751-908X.2007.00865.x
- 1245 Bourdelle F, Cathelineau M (2015) Low-temperature chlorite geothermometry: a graphical representation based on a
1246 T?R2? ?Si diagram. *Eur J Mineral* 27:617–626. doi: 10.1127/ejm/2015/0027-2467
- 1247 Breemen O van, Peterson TD, Sandeman HA (2005) U– Pb zircon geochronology and Nd isotope geochemistry of

1248 Proterozoic granitoids in the western Churchill Province: intrusive age pattern and Archean source domains.
1249 Can J Earth Sci 42:339–377. doi: 10.1139/e05-007

1250 Bright S, Conner G, Turner A, Vearncombe J (2014) Drill core, structure and digital technologies. Appl Earth Sci
1251 123:47–68. doi: 10.1179/1743275814Y.0000000051

1252 Burma BH, Riley CM (1955) Two unusual occurrences of microstylonite. J Sediment Res 25:38–40. doi:
1253 10.1306/D42697EC-2B26-11D7-8648000102C1865D

1254 Caine JS, Evans JP, Forster CB (1996) Fault zone architecture and permeability structure. Geology 24:1025–1028

1255 Cathelineau M (1988) Cation Site Occupancy in Chlorites and Illites as a Function of Temperature. Clay Miner -
1256 CLAY Min 23:471–485

1257 Cathelineau M, Boiron MC, Holliger P, Poty B (1990) Metallogenesis of the French part of the Variscan orogen. Part
1258 II: Time-space relationships between U, Au and Sn–W ore deposition and geodynamic events —
1259 mineralogical and U–Pb data. Tectonophysics 177:59–79. doi: [https://doi.org/10.1016/0040-1951\(90\)90274-C](https://doi.org/10.1016/0040-1951(90)90274-C)

1260 Chamberlain KR, Schmitt AK, Swapp SM, et al (2010) In situ U–Pb SIMS (IN-SIMS) micro-baddeleyite dating of
1261 mafic rocks: Method with examples. Precambrian Res 183:379–387. doi: 10.1016/j.precamres.2010.05.004

1262 Chester FM, Logan JM (1986) Implications for mechanical properties of brittle faults from observations of the
1263 Punchbowl fault zone, California. pure Appl Geophys 124:79–106. doi: 10.1007/BF00875720

1264 Chi G, Haid T, Quirt D, et al (2017) Petrography, fluid inclusion analysis, and geochronology of the End uranium
1265 deposit, Kiggavik, Nunavut, Canada. Miner Depos 52:211–232. doi: 10.1007/s00126-016-0657-9

1266 Chu H, Chi G (2016) Thermal profiles inferred from fluid inclusion and illite geothermometry from sandstones of
1267 the Athabasca basin: Implications for fluid flow and unconformity-related uranium mineralization. Ore Geol
1268 Rev 75:284–303. doi: <https://doi.org/10.1016/j.oregeorev.2015.12.013>

1269 Cook DG, MacLean BC (1995) The intracratonic Paleoproterozoic Forward orogeny, and implications for regional
1270 correlations, Northwest Territories, Canada. Can J Earth Sci 32:1991–2008. doi: 10.1139/e95-152

1271 Cook FA (1992) Racklan Orogen. Can J Earth Sci 29:2490–2496. doi: 10.1139/e92-195

1272 Corrigan D, Pehrsson S, Wodicka N, de Kemp E (2009) The Palaeoproterozoic Trans-Hudson Orogen: a prototype
1273 of modern accretionary processes. Geol Soc London, Spec Publ 327:457–479. doi: 10.1144/SP327.19

1274 Cumming GL, Krstic D (1992) The age of unconformity-related uranium mineralization in the Athabasca Basin,
1275 northern Saskatchewan. Can J Earth Sci 29:1623–1639. doi: 10.1139/e92-128

- 1276 Cuney M (2014) Felsic magmatism and uranium deposits. *Bull la Soc Geol Fr* 185:75–92
- 1277 Cuney M, Kyser K (2009) Recent and Not-So-Recent Developments in Uranium Deposits and Implications for
1278 Exploration. *Econ Geol* 104:600–601
- 1279 Cuney M, Kyser TK, Mineralogical Association of Canada (2015) The geology and geochemistry of uranium and
1280 thorium deposits
- 1281 Curtis L, Miller AR (1980) Uranium geology in the Amer-Dubawnt-Yathkyed-Baker Lakes region, Keewatin
1282 district, NWT Canada. *Proc Int Uranium Symp Pine Creek Geosyncline* 22
- 1283 Davis WJ, Gall Q, Jefferson CW, Rainbird RH (2011) Fluorapatite in the Paleoproterozoic Thelon Basin: Structural-
1284 stratigraphic context, in situ ion microprobe U-Pb ages, and fluid-flow history. *GSA Bull* 123:1056–1073
- 1285 Davis WJ, Hanmer S, Tella S, et al (2006) U–Pb geochronology of the MacQuoid supracrustal belt and Cross Bay
1286 plutonic complex: Key components of the northwestern Hearne subdomain, western Churchill Province,
1287 Nunavut, Canada. *Precambrian Res* 145:53–80. doi: <https://doi.org/10.1016/j.precamres.2005.11.016>
- 1288 Depiné M, Frimmel HE, Emsbo P, et al (2013) Trace element distribution in uraninite from Mesoarchaeon
1289 Witwatersrand conglomerates (South Africa) supports placer model and magmatogenic source. *Miner Depos*
1290 48:423–435. doi: 10.1007/s00126-013-0458-3
- 1291 Derome D, Cathelineau M, Cuney M, et al (2005) Mixing of Sodic and Calcic Brines and Uranium Deposition at
1292 McArthur River, Saskatchewan, Canada: A Raman and Laser-Induced Breakdown Spectroscopic Study of
1293 Fluid Inclusions. *Econ Geol* 100:1529–1545. doi: 10.2113/gsecongeo.100.8.1529
- 1294 Dieng S, Kyser K, Godin L (2013) Tectonic history of the North American shield recorded in uranium deposits in the
1295 Beaverlodge area , northern Saskatchewan , Canada. *Precambrian Res* 224:316–340. doi:
1296 10.1016/j.precamres.2012.09.011
- 1297 Dieng S, Kyser K, Godin L (2015) Genesis of Multifarious Uranium Mineralization in the Beaverlodge Area,
1298 Northern Saskatchewan, Canada. *Econ Geol* 110:209–240
- 1299 Donald Bloss F (1954) Microstylolites in a Rhyolite Porphyry. *J Sediment Res - J SEDIMENT RES* Vol. 24:
- 1300 Dubacq B, Vidal O, De Andrade V (2010) Dehydration of dioctahedral aluminous phyllosilicates: Thermodynamic
1301 modelling and implications for thermobarometric estimates. *Contrib to Mineral Petrol* 159:159–174
- 1302 Dubessy J, Pagel M, Beny J, et al (1988) Radiolysis evidenced by Hz-O₂ and Hz-bearing fluid inclusions in three
1303 uranium deposits. 52:

1304 Dubessy J, Poty B, Ramboz C (1989) Advances in C-O-H-N-S fluid geochemistry based on micro-Raman
1305 spectrometric analysis of fluid inclusions. *Eur J Mineral* 1:517–534. doi: 10.1127/ejm/1/4/0517

1306 Eglinger A, André-Mayer A-S, Vanderhaeghe O, et al (2013) Geochemical signatures of uranium oxides in the
1307 Lufilian belt: From unconformity-related to syn-metamorphic uranium deposits during the Pan-African
1308 orogenic cycle. *Ore Geol Rev* 54:197–213. doi: <https://doi.org/10.1016/j.oregeorev.2013.04.003>

1309 Farkas A (1984) Lone Gull Deposit Mineralogy and Host Rock Alteration. 191

1310 Faulkner DR, Jackson CAL, Lunn RJ, et al (2010) A review of recent developments concerning the structure,
1311 mechanics and fluid flow properties of fault zones. *J Struct Geol* 32:1557–1575. doi: 10.1016/j.jsg.2010.06.009

1312 Fayek M, Kyser TK, Riciputi LR (2002) U and Pb isotope analysis of uranium minerals by ion microprobe and the
1313 geochronology of McArthur River and Sue Zone Uranium deposits, Saskatchewan, Canada. *Can Mineral*
1314 40:1553. doi: 10.2113/gscanmin.40.6.1553

1315 Fayek M, Quirt D, Jefferson CW, et al (2017) The Kiggavik-Andrew Lake structural trend uranium deposits : An
1316 overview. 4

1317 Fossen H, Rotevatn A (2016) Fault linkage and relay structures in extensional settings-A review. *Earth-Science Rev*
1318 154:14–28. doi: 10.1016/j.earscirev.2015.11.014

1319 Friedrich G, Weyer HJ, Bectel A, Ballhorn RK (1989) The Lone Gull uranium deposit - New geochemical and
1320 petrological data as evidence for the nature of the ore bearing solutions. IAEA, Tech Comm Metallog uranium
1321 Depos 293–305

1322 Frimmel HE, Schedel S, Brätz H (2014) Uraninite chemistry as forensic tool for provenance analysis. *Appl*
1323 *Geochemistry* 48:104–121. doi: <https://doi.org/10.1016/j.apgeochem.2014.07.013>

1324 Fuchs HD, Hilger W (1989) Kiggavik (Lone Gull): An unconformity related uranium deposit in the Thelon basin,
1325 northwest territories, Canada

1326 Fuchs HD, Hilger W, Prosser E (1986) Geology and Exploration History of the Lone Gull Property

1327 Gall Q, Peterson TD, Donaldson J (1992) A proposed revision of Early Proterozoic stratigraphy of the Thelon and
1328 Baker Lake basins, Northwest Territories. *Geol Surv Canada Curr Res* 92–1c:129–137

1329 Golding HG, Conolly JR (1962) Stylolites in volcanic rocks. *J Sediment Res* 32:534–538. doi: 10.1306/74D70D12-
1330 2B21-11D7-8648000102C1865D

1331 Gordon MB, Hempton MR (1986) Collision-induced rifting: The Grenville Orogeny and the Keweenawan Rift of

- 1332 North America. *Tectonophysics* 127:1–25. doi: [https://doi.org/10.1016/0040-1951\(86\)90076-4](https://doi.org/10.1016/0040-1951(86)90076-4)
- 1333 Grare A, Benedicto A, Lacombe O, et al (2018a) The Contact uranium prospect, Kiggavik project, Nunavut
1334 (Canada): Tectonic history, structural constraints and timing of mineralization. *Ore Geol Rev* 93:141–167. doi:
1335 <https://doi.org/10.1016/j.oregeorev.2017.12.015>
- 1336 Grare A, Lacombe O, Mercadier J, et al (2018b) Fault Zone Evolution and Development of a Structural and
1337 Hydrological Barrier: The Quartz Breccia in the Kiggavik Area (Nunavut, Canada) and Its Control on Uranium
1338 Mineralization. *Minerals* 8:319. doi: 10.3390/min8080319
- 1339 Gueguen Y, Palciauskas V, Jeanloz R (1995) Introduction to Physics of Rocks. *Phys Today - PHYS TODAY* 48:
- 1340 Guillong M, Meier DL, Allan MM, Yardley BWD (2008) SILLS: A MATLAB-based program for the reduction of
1341 laser ablation ICP-MS data of homogeneous materials and inclusions. In: *Laser ablation ICP-MS in the Earth*
1342 *sciences: current practices and outstanding issues*, vol 40. Mineralogical Association of Canada Short Course
1343 Series, Sylvester. Vancouver, pp 328–333
- 1344 Hadlari T, Rainbird RH (2011) Retro-arc extension and continental rifting : a model for the Paleoproterozoic Baker
1345 Lake Basin ., doi: 10.1139/E11-002
- 1346 HadlariT., RainbirdR.H. (2011) Retro-arc extension and continental rifting: a model for the Paleoproterozoic Baker
1347 Lake Basin, Nunavut1Geological Survey of Canada Contribution 20100436. *Can J Earth Sci* 48:1232–1258.
1348 doi: 10.1139/e11-002
- 1349 Hasegawa K, Davidson GI, Wollenberg P, Lida Y (1990) Geophysical Exploration for Unconformity-related
1350 uranium deposits in the Northeastern part of the Thelon basin, Northwest territories, Canada. *Kozan Chishitsu*
1351 40:83–94
- 1352 Hatcher Robert D. J (2002) Alleghanian (Appalachian) orogeny, a product of zipper tectonics: Rotational
1353 transpressive continent-continent collision and closing of ancient oceans along irregular margins. In: Catalán
1354 JRM, Hatcher Robert D. J, Arenas R, García FD (eds) *Variscan-Appalachian dynamics: The building of the*
1355 *late Paleozoic basement*. Geological Society of America
- 1356 Heaman LM, LeCheminant AN (1993) Paragenesis and U-Pb systematics of baddeleyite (ZrO₂). *Chem Geol*
1357 110:95–126. doi: [http://dx.doi.org/10.1016/0009-2541\(93\)90249-I](http://dx.doi.org/10.1016/0009-2541(93)90249-I)
- 1358 Hiatt EE, Kyser K, Dalrymple RW (2003) Relationships among sedimentology, stratigraphy, and diagenesis in the
1359 Proterozoic Thelon Basin, Nunavut, Canada: Implications for paleoquifers and sedimentary-hosted mineral

- 1360 deposits. *J Geochemical Explor* 80:221–240. doi: 10.1016/S0375-6742(03)00192-4
- 1361 Hoeve J, Quirt DH (1984) Mineralization and host rock alteration in relation to clay mineral diagenesis and evolution
1362 of the Middle-Proterozoic, Athabasca Basin, Northern Saskatchewan, Canada
- 1363 Hoffman PF (1988) United Plates of America, The Birth of a Craton: Early Proterozoic Assembly and Growth of
1364 Laurentia. *Annu Rev Earth Planet Sci* 16:543–603. doi: 10.1146/annurev.ea.16.050188.002551
- 1365 Hou G, Kusky TM, Wang C, Wang Y (2010) Mechanics of the giant radiating Mackenzie dyke swarm: A paleostress
1366 field modeling. *J Geophys Res Solid Earth* 115:n/a-n/a. doi: 10.1029/2007JB005475
- 1367 Hunt PA, Roddick JC (1988) A compilation of K-Ar ages: Report 18. In: *Radiogenic Age and Isotopic Studies:*
1368 *Report 2, Paper 88-2. Geological Survey of Canada*, pp 127–153
- 1369 Hunt PA, Roddick JC (1992a) A compilation of K-Ar ages: Report 21. In: *Radiogenic Age and Isotopic Studies:*
1370 *Report 5, Paper 91-2. Geological Survey of Canada*, pp 207–261
- 1371 Hunt PA, Roddick JC (1992b) A compilation of K-Ar and ^{40}Ar - ^{39}Ar ages: Report 22. In: *Radiogenic Age and*
1372 *Isotopic Studies: Report 6, Paper 92-2. Geological Survey of Canada*, pp 179–226
- 1373 J. Bridge N, Banerjee N, Pehrsson S, et al (2013) Lac Cinquante Uranium Deposit, Western Churchill Province,
1374 Nunavut, Canada. *Explor Min Geol* 21:27–50
- 1375 Jefferson C, Pehrsson S, Peterson T, et al (2011) Northeast Thelon region geoscience framework - new maps and
1376 data for uranium in Nunavut. 288791. doi: 10.4095/288791
- 1377 Jefferson CW, Thomas DJ, Gandhi SS, et al (2007) Unconformity-associated uranium deposits of the Athabasca
1378 Basin, Saskatchewan and Alberta. *Bull Surv Canada* 588:23
- 1379 Johnstone D Geology , tectonics and setting of uranium mineralization in the central Rae craton of Laurentia
- 1380 Jowett EC (1991) Fitting iron and magnesium into the hydrothermal chlorite geothermometer. In: *GAC/MAC/SEG*
1381 *Joint Annual Meeting, Toronto, May 27-29, 1991, Program with Abstracts* 16
- 1382 Kim Y-S, Peacock DCP, Sanderson DJ (2004) Fault damage zones. *J Struct Geol* 26:503–517. doi:
1383 <https://doi.org/10.1016/j.jsg.2003.08.002>
- 1384 Kotzer TG, Kyser TK (1995) Petrogenesis of the Proterozoic Athabasca Basin, northern Saskatchewan, Canada, and
1385 its relation to diagenesis, hydrothermal uranium mineralization and paleohydrogeology. *Chem Geol* 120:45–
1386 89. doi: [https://doi.org/10.1016/0009-2541\(94\)00114-N](https://doi.org/10.1016/0009-2541(94)00114-N)
- 1387 Kranidiotis P, MacLean WH (1987) Systematics of chlorite alteration at the Phelps Dodge massive sulfide deposit,

1388 Matagami, Quebec. *Econ Geol* 82:1898–1911. doi: 10.2113/gsecongeo.82.7.1898

1389 Lach P (2012) Signature géochimique des éléments des terres rares dans les oxydes d'uranium et minéraux associés
1390 dans les gisements d'uranium : analyse par ablation laser couplée à l'ICP-MS et étude géochronologique.
1391 Thèse de doctorat en Géosciences Sous la direction de Jean Dubessy et de Michel Cuney, Université de
1392 Lorraine, 320 p.

1393 Lach P, Mercadier J, Dubessy J, et al (2013) In Situ Quantitative Measurement of Rare Earth Elements in Uranium
1394 Oxides by Laser Ablation-Inductively Coupled Plasma-Mass Spectrometry. *Geostand Geoanalytical Res*
1395 37:277–296. doi: 10.1111/j.1751-908X.2012.00161.x

1396 LeCheminant AN, Heaman LM (1989) Mackenzie igneous events, Canada: Middle Proterozoic hotspot magmatism
1397 associated with ocean opening. *Earth Planet Sci Lett* 96:38–48. doi: [http://dx.doi.org/10.1016/0012-](http://dx.doi.org/10.1016/0012-821X(89)90122-2)
1398 821X(89)90122-2

1399 LeCheminant AN, Miller AR, Booth GW, et al (1979) Geology of the Tebesjuak lake map area - a progress report
1400 with notes on uranium and Base metal mineralization. 30

1401 LeCheminant AN, Miller AR, LeCheminant GM (1987) Early Proterozoic Alkaline Igneous Rocks, District of
1402 Keewatin, Canada: Petrogenesis and Mineralization. *Geol Soc London, Spec Publ* 33:219–240. doi:
1403 10.1144/GSL.SP.1987.033.01.16

1404 Leisen M, Boiron M-C, Richard A, Dubessy J (2012) Determination of Cl and Br concentrations in individual fluid
1405 inclusions by combining microthermometry and LA-ICPMS analysis: Implications for the origin of salinity in
1406 crustal fluids. *Chem Geol* 330–331:197–206. doi: <https://doi.org/10.1016/j.chemgeo.2012.09.003>

1407 Lespinasse M (1999) Are fluid inclusion planes useful in structural geology? *J Struct Geol* 21:1237–1243. doi:
1408 [https://doi.org/10.1016/S0191-8141\(99\)00027-9](https://doi.org/10.1016/S0191-8141(99)00027-9)

1409 Lespinasse M, Désindes L, Fratzak P, Petrov V (2005) Microfissural mapping of natural cracks in rocks:
1410 Implications for fluid transfers quantification in the crust. *Chem Geol* 223:170–178. doi:
1411 <https://doi.org/10.1016/j.chemgeo.2005.05.009>

1412 Lespinasse M, Pêcher A (1986) Microfracturing and regional stress field: a study of the preferred orientations of
1413 fluid-inclusion planes in a granite from the Massif Central, France. *J Struct Geol* 8:169–180. doi:
1414 [https://doi.org/10.1016/0191-8141\(86\)90107-0](https://doi.org/10.1016/0191-8141(86)90107-0)

1415 Lida Y (1997) Geochemical and Mineralogical studies - 1997 Sissons Project. 169

1416 Ludwig K (2007) Isoplot/Ex version 3.41b, a geochronological toolkit for Microsoft Excel. Berkeley Geochronol
1417 Cent Spec Publ

1418 Martz P, Cathelineau M, Mercadier J, et al (2017) C-O-H-N fluids circulations and graphite precipitation in
1419 reactivated Hudsonian shear zones during basement uplift of the Wollaston-Mudjatik Transition Zone:
1420 Example of the Cigar Lake U deposit. *Lithos* 294–295:222–245. doi:
1421 <https://doi.org/10.1016/j.lithos.2017.10.001>

1422 Martz P, Mercadier J, Cathelineau M, et al (2018) Formation of U-rich mineralizing fluids through basinal brine
1423 migration within basement-hosted shear zones: A large-scale study of the fluid chemistry around the
1424 unconformity-related Cigar Lake U deposit (Saskatchewan, Canada). *Chem Geol.* doi:
1425 <https://doi.org/10.1016/j.chemgeo.2018.05.042>

1426 McClellan E, Gazel E (2014) The Cryogenian intra-continental rifting of Rodinia: Evidence from the Laurentian
1427 margin in eastern North America. *Lithos* 206–207:321–337. doi: <https://doi.org/10.1016/j.lithos.2014.08.006>

1428 Mercadier J, Annesley IR, McKechnie CL, et al (2013) Magmatic and Metamorphic Uraninite Mineralization in the
1429 Western Margin of the Trans-Hudson Orogen (Saskatchewan, Canada): A Uranium Source for Unconformity-
1430 Related Uranium Deposits? *Econ Geol* 108:1037. doi: 10.2113/econgeo.108.5.1037

1431 Mercadier J, Cuney M, Cathelineau M, Lacorde M (2011a) U redox fronts and kaolinisation in basement-hosted
1432 unconformity-related U ores of the Athabasca Basin (Canada): Late U remobilisation by meteoric fluids. *Miner*
1433 *Depos* 46:105–135. doi: 10.1007/s00126-010-0314-7

1434 Mercadier J, Cuney M, Lach P, et al (2011b) Origin of uranium deposits revealed by their rare earth element
1435 signature. *Terra Nov* 23:264–269. doi: 10.1111/j.1365-3121.2011.01008.x

1436 Mercadier J, Richard A, Boiron MC, et al (2010) Migration of brines in the basement rocks of the Athabasca Basin
1437 through microfracture networks (P-Patch U deposit, Canada). *Lithos* 115:121–136. doi:
1438 [10.1016/j.lithos.2009.11.010](https://doi.org/10.1016/j.lithos.2009.11.010)

1439 Mercadier J, Richard A, Cathelineau M (2012) Boron- and magnesium-rich marine brines at the origin of giant
1440 unconformity-related uranium deposits: $\delta^{11}\text{B}$ evidence from Mg-tourmalines. *Geology* 40:231. doi:
1441 [10.1130/G32509.1](https://doi.org/10.1130/G32509.1)

1442 Miller AR (1980) Uranium geology of the eastern Baker lake basin, district of keewatin, northwest territories.
1443 Geological Survey of Canada, bulletin 330

- 1444 Miller AR (1982) Alteration and Mineralization types: Amer-Thelon Area, NTS 66G, H District of Keewatin,
1445 N.W.T. Pref to Res Doc #1 Westmin Resour Ltd
- 1446 Miller AR (1995) Polymetallic unconformity-related uranium veins in lower Proterozoic Amer Group, Pelly Lake
1447 map area, northern Thelon Basin, Churchill Province, Northwest territories. *Curr Res* 1995-C; *Geol Surv*
1448 *Canada* 151–161
- 1449 Miller AR (1997) Petrography and Mineral Chemistry of the Jane Prospect: A platinum group element-bearing
1450 basement-hosted unconformity-related uranium deposit type. 128
- 1451 Miller AR, Blackwell GW (1992) Petrology of Alkaline Rare Earth Element - Bearing Plutonic Rocks, Enekatcha
1452 Lake [65e/15] and Carey Lake [65l/7] map - Areas, District of Mackenzie. *Geol Surv Canada*, Open File 2484
1453 129–134. doi: <https://doi.org/10.4095/133336>
- 1454 Miller AR, LeCheminant AN (1985) Geology and uranium metallogeny of Proterozoic supracrustal successions,
1455 central district of Keewatin. 19
- 1456 Miller AR, Stanton RA, Cluff GR, Male MJ (1986) Uranium deposits and prospects of the Baker Lake Basin and
1457 subbasins, Central District of Keewatin, Northwest Territories. *Uranium Depos Canada*, CIM Spec Vol 33 23
- 1458 Ng R, Alexandre P, Kyser K (2013) Mineralogical and Geochemical Evolution of the Unconformity-Related
1459 McArthur River Zone 4 Orebody in the Athabasca Basin, Canada: Implications of a Silicified Zone*. *Econ*
1460 *Geol* 108:1657. doi: 10.2113/econgeo.108.7.1657
- 1461 Pacquet A (1993a) Report 8493 Canada Kiggavik Main Zone D.H. 306 (93-UGC-92-01) - Petrography and XRD
1462 analysis. 19
- 1463 Pacquet A (1993b) Report 8494 - Canada - Sissons Schultz South - End Grid DH END 42 - Petrography and XRD
1464 analysis. 14
- 1465 Pacquet A (1993c) Report 8556 - XRD - Andrew Lake Centre (Lower Lens) DH SW 78. 2
- 1466 Pacquet A (1994) Report 8549 - Canada (NWT) Andrew Lake DH SW 73 - Petrography and XRD. 12
- 1467 Pagel M (1975) Cadre géologique des gisements d'uranium dans la structure de Carswell (Saskatchewan, Canada).
1468 Etudes des phases fluides. Thèse de 3ème cycle, Université de Nancy, Nancy, France. 171
- 1469 Pagel M (1995) Etude des inclusions fluides dans les quartz des gisements U de l'Athabasca et du Thelon.pdf. 1–10
- 1470 Pascal M, Ansdell K, Annesley I (2015) Graphite-bearing and Graphite-depleted Basement Rocks in the Dufferin
1471 Lake Zone, South-central Athabasca Basin, Saskatchewan. 83–92

1472 Pehrsson SJ, Berman RG, Eglington B, Rainbird R (2013) Two Neoproterozoic supercontinents revisited : The case for a
1473 Rae family of cratons. *Precambrian Res* 232:27–43. doi: 10.1016/j.precamres.2013.02.005

1474 Percival JA, Tschirhart V (2017) Trans-Hudsonian far-field deformation effects in the Rae foreland: An integrated
1475 geological-3D magnetic model. *Tectonophysics* 699:82–92. doi: 10.1016/j.tecto.2017.01.021

1476 Peterson TD (2006) Geology of the Dubawnt Lake area, Nunavut-Northwest Territories. *Bull Geol Surv Canada* 580:

1477 Peterson TD (2015) Geological setting and geochemistry of the ca. 2.6 Ga Snow island Suite in the central Rae
1478 Domain of the Western Churchill Province, Nunavut. *Geol Surv Canada Open File* 7841:

1479 Peterson TD, Breemen O Van, Sandeman H, Cousens B (2002) Proterozoic (1.85–1.75 Ga) igneous suites of the
1480 Western Churchill Province: granitoid and ultrapotassic magmatism in a reworked Archean hinterland.
1481 *Precambrian Res* 119:73–100. doi: [https://doi.org/10.1016/S0301-9268\(02\)00118-3](https://doi.org/10.1016/S0301-9268(02)00118-3)

1482 Peterson TD, Scott MJ, Jefferson CW (2011) Uranium-rich bostonite-carbonatite dykes in Nunavut : recent
1483 observations *Geological Survey of Canada Current Research* 2011-11. 12

1484 Peterson TD, Scott MJ, LeCheminant AN, et al (2015) The Kivalliq Igneous Suite: Anorogenic bimodal magmatism
1485 at 1.75Ga in the western Churchill Province, Canada. *Precambrian Res* 262:101–119. doi:
1486 10.1016/j.precamres.2015.02.019

1487 Pinheiro RVL, Holdsworth RE (1997) Reactivation of Archaean strike-slip fault systems, Amazon region, Brazil. *J*
1488 *Geol Soc London* 154:99–103. doi: 10.1144/gsjgs.154.1.0099

1489 Polito PA, Kyser TK, Rheinberger G, Southgate PN (2005) A Paragenetic and Isotopic Study of the Proterozoic
1490 Westmoreland Uranium Deposits, Southern McArthur Basin, Northern Territory, Australia. *Econ Geol*
1491 100:1243–1260. doi: 10.2113/gsecongeo.100.6.1243

1492 Potter E, M Wright D (2015) TGI-4 Unconformity-related uranium deposits synthesis: tools to aid deep exploration
1493 and refine the genetic model. *Bull Geol Surv Canada Open File*:1–13

1494 Rainbird RH, Davis WJ (2007) U-Pb detrital zircon geochronology and provenance of the late Paleoproterozoic
1495 Dubawnt Supergroup: Linking sedimentation with tectonic reworking of the western Churchill Province,
1496 Canada. *GSA Bull* 119:314. doi: 10.1130/B25989.1

1497 Rainbird RH, Davis WJ, Pehrsson SJ, et al (2010) Early Paleoproterozoic supracrustal assemblages of the Rae
1498 domain, Nunavut, Canada: Intracratonic basin development during supercontinent break-up and assembly.
1499 *Precambrian Res* 181:167–186. doi: <https://doi.org/10.1016/j.precamres.2010.06.005>

- 1500 Rainbird RH, Davis WJ, Stern RA, et al (2006) Ar-Ar and U-Pb Geochronology of a Late Paleoproterozoic Rift
1501 Basin: Support for a Genetic Link with Hudsonian Orogenesis, Western Churchill Province, Nunavut, Canada.
1502 J Geol 114:1–17. doi: 10.1086/498097
- 1503 Rainbird RH, Hadlari T, Aspler LB, et al (2003) Sequence stratigraphy and evolution of the paleoproterozoic
1504 intracontinental Baker Lake and Thelon basins, western Churchill Province, Nunavut, Canada. Precambrian
1505 Res 125:21–53. doi: 10.1016/S0301-9268(03)00076-7
- 1506 Ramaekers P, Jefferson CW, Yeo GM, et al (2007) Revised geological map and stratigraphy of the Athabasca group,
1507 Saskatchewan and Alberta. Bull Geol Surv Canada 588:155–191
- 1508 Renac C, Kyser TK, Durocher K, et al (2002) Comparison of diagenetic fluids in the Proterozoic Thelon and
1509 Athabasca Basins, Canada: implications for protracted fluid histories in stable intracratonic basins. Can J Earth
1510 Sci 39:113–132. doi: 10.1139/e01-077
- 1511 Richard A (2017) Radiolytic (H₂, O₂) and other Trace Gases (CO₂, CH₄, C₂H₆, N₂) in Fluid Inclusions from
1512 Unconformity-related U Deposits. Procedia Earth Planet Sci 17:273–276. doi:
1513 <https://doi.org/10.1016/j.proeps.2016.12.053>
- 1514 Richard A, Banks DA, Mercadier J, et al (2011a) An evaporated seawater origin for the ore-forming brines in
1515 unconformity-related uranium deposits (Athabasca Basin, Canada): Cl/Br and $\delta^{37}\text{Cl}$ analysis of fluid
1516 inclusions. Geochim Cosmochim Acta 75:2792–2810. doi: <https://doi.org/10.1016/j.gca.2011.02.026>
- 1517 Richard A, Boulvais P, Mercadier J, et al (2013) From evaporated seawater to uranium-mineralizing brines : Isotopic
1518 and trace element study of quartz – dolomite veins in the Athabasca system. Geochim Cosmochim Acta
1519 113:38–59. doi: 10.1016/j.gca.2013.03.009
- 1520 Richard A, Cathelineau M, Boiron M-C, et al (2016) Metal-rich fluid inclusions provide new insights into
1521 unconformity-related U deposits (Athabasca Basin and Basement, Canada). Miner Depos 51:249–270
- 1522 Richard A, Cauzid J, Cathelineau M, et al (2012) Synchrotron-XRF and XANES investigation of fluid inclusions
1523 from unconformity-related uranium deposits
- 1524 Richard A, Kendrick MA, Cathelineau M (2014) Noble gases (Ar, Kr, Xe) and halogens (Cl, Br, I) in fluid inclusions
1525 from the Athabasca Basin (Canada): Implications for unconformity-related U deposits. Precambrian Res
1526 247:110–125. doi: <https://doi.org/10.1016/j.precamres.2014.03.020>
- 1527 Richard A, Pettke T, Cathelineau M, et al (2010) Brine – rock interaction in the Athabasca basement (McArthur

1528 River U deposit , Canada): consequences for fluid chemistry and uranium uptake. 303–308. doi:
1529 10.1111/j.1365-3121.2010.00947.x

1530 Richard A, Rozsypal C, Mercadier J, et al (2011b) Giant uranium deposits formed from exceptionally uranium-rich
1531 acidic brines. *Nat Geosci* 5:142–146. doi: 10.1038/ngeo1338

1532 Riegler T (2013) Système d’altération et minéralisation en uranium le long du faisceau structural Kiggavik - Andrew
1533 Lake (Nunavut, Canada) : modèle génétique et guides d’exploration. Poitiers

1534 Riegler T, Lescuyer J-L, Wollenberg P, et al (2014) Alteration related to uranium deposits in the Kiggavik-Andrew
1535 Lake structural trend, Nunavut, Canada: new insights from clay mineralogy and petrography. *Can Mineral*
1536 52:27–45. doi: 10.3749/canmin.52.1.27

1537 Riegler T, Quirt D, Beaufort D (2016) Spatial distribution and compositional variation of APS minerals related to
1538 uranium deposits in the Kiggavik-Andrew Lake structural trend, Nunavut, Canada. *Miner Depos* 51:219–236.
1539 doi: 10.1007/s00126-015-0595-y

1540 Romberger SB (1984) Transport and deposition of uranium in hydrothermal systems at temperatures up to
1541 300°C: geological implications. In: De Vivo B, Ippolito F, Capaldi G, Simpson PR (eds) *Uranium*
1542 *geochemistry, mineralogy, geology, exploration and resources*. Springer Netherlands, Dordrecht, pp 12–17

1543 Rotevatn A, Bastesen E (2014) Fault linkage and damage zone architecture in tight carbonate rocks in the Suez Rift
1544 (Egypt): implications for permeability structure along segmented normal faults. *Geol Soc London, Spec Publ*
1545 374:79–95. doi: 10.1144/SP374.12

1546 Roy R, Benedicto A, Grare A, et al (2017) Three-dimensional gravity modelling applied to the exploration of
1547 uranium unconformity-related basement-hosted deposits: the Contact prospect case study, Kiggavik, northeast
1548 Thelon region (Nunavut, Canada). *Can J Earth Sci* 54:869–882. doi: 10.1139/cjes-2016-0225

1549 Rutter EH (1983) Pressure solution in nature, theory and experiment. *J Geol Soc London* 140:725–740. doi:
1550 10.1144/gsjgs.140.5.0725

1551 Schorscher HD, Shea ME (1992) The regional geology of the Poços de Caldas alkaline complex: mineralogy and
1552 geochemistry of selected nepheline syenites and phonolites. *J Geochemical Explor* 45:25–51. doi:
1553 [https://doi.org/10.1016/0375-6742\(92\)90121-N](https://doi.org/10.1016/0375-6742(92)90121-N)

1554 Scott J, Peterson TD (2012) U, Th, and REE occurrences within Nueltin granite at Nueltin Lake, Nunavut: recent
1555 observations. *Geol Surv Canada Curr Res* 2012–1:

- 1556 Scott JMJ, Peterson TD, Jefferson CW, Cousens BL (2015) Petrology and geochronology of Paleoproterozoic
1557 intrusive rocks, Kiggavik uranium camp, Nunavut. *Can J Earth Sci* 518:1–80. doi: 10.1139/cjes-2014-0153
- 1558 Shabaga BM, Fayek M, Quirt D, et al (2017) Mineralogy, geochronology, and genesis of the Andrew Lake uranium
1559 deposit, Thelon Basin, Nunavut, Canada. *Can J Earth Sci* 54:850–868. doi: 10.1139/cjes-2017-0024
- 1560 Sharpe R, Fayek M, Quirt D, Jefferson CW (2015) Geochronology and genesis of the bong uranium deposit, Thelon
1561 Basin, Nunavut, Canada. *Econ Geol* 110:1759–1777. doi: 10.2113/econgeo.110.7.1759
- 1562 Stacey JS, Kramers JD (1975) Approximation of terrestrial lead isotope evolution by a two-stage model. *Earth Planet
1563 Sci Lett* 26:207–221. doi: [https://doi.org/10.1016/0012-821X\(75\)90088-6](https://doi.org/10.1016/0012-821X(75)90088-6)
- 1564 Thorkelson D (2000) Geology and mineral occurrences of the Slats Creek, Fairchild Lake and “Dolores Creek”
1565 areas, Wernecke Mountains, Yukon Territory (106 D/16, 106 C/13, 106 C/14). *Geol Miner Occur Slats Creek,
1566 Fairchild Lake Dolores Creek Areas 10:*
- 1567 Tschirhart P, Morris WA, Jefferson CW (2013) Geophysical modelling of the Neoproterozoic Woodburn Lake and
1568 Paleoproterozoic Ketyet River groups , and plutonic rocks in central Schultz Lake map area , Nunavut
1569 Geophysical modelling of the Neoproterozoic Woodburn Lake and Paleoproterozoic Ketyet River groups ,. *Curr
1570 Res*
- 1571 Tschirhart V, Jefferson CW, Morris WA (2017) Basement geology beneath the northeast Thelon Basin, Nunavut:
1572 insights from integrating new gravity, magnetic and geological data. *Geophys Prospect* 65:617–636. doi:
1573 10.1111/1365-2478.12430
- 1574 Turner W, Richards J, Nesbitt B, et al (2001) Proterozoic low-sulfidation epithermal Au-Ag mineralization in the
1575 Mallery Lake area, Nunavut, Canada. *Miner Depos* 36:442–457. doi: 10.1007/s001260100181
- 1576 Turner WA, Heaman LM, Creaser RA (2003) Sm–Nd fluorite dating of Proterozoic low-sulfidation epithermal Au–
1577 Ag deposits and U–Pb zircon dating of host rocks at Mallery Lake, Nunavut, Canada. *Can J Earth Sci*
1578 40:1789–1804. doi: 10.1139/e03-061
- 1579 Velde B (ed) (1985) III-General Phase Diagrams for Some Clay Mineral Assemblages. In: *Clay Minerals*. Elsevier,
1580 pp 257–357
- 1581 W Jefferson C, Thomas DJ, S Gandhi S, et al (2007) Unconformity-associated uranium deposits of the Athabasca
1582 Basin, Saskatchewan and Alberta. *Bull. Geol. Surv. Canada* 588:23–67
- 1583 Weyer HJ, Friedrich G, Bechtel A, Ballhorn RK (1987) The Lone Gull Uranium deposit - New geochemical and

1584 petrological data as evidence for the nature of the ore bearing solutions. 14
1585 Wibberley CAJ, Yielding G, Di Toro G (2008) Recent advances in the understanding of fault zone internal structure:
1586 A review. *Intern Struct Fault Zo Implic Mech Fluid-Flow Prop* 299:5–33. doi: 10.1144/SP299.2
1587 Williams JH, Johnson CD (2004) Acoustic and optical borehole-wall imaging for fractured-rock aquifer studies. *J*
1588 *Appl Geophys* 55:151–159. doi: <https://doi.org/10.1016/j.jappgeo.2003.06.009>
1589 Zang W, Fyfe WS (1995) Chloritization of the hydrothermally altered bedrock at the Igarap{é} Bahia gold deposit,
1590 Caraj{á}s, Brazil. *Miner Depos* 30:30–38. doi: 10.1007/BF00208874

1591
1592
1593
1594
1595
1596 **Fig. 1** Geological map of the Thelon-Baker Lake area (after [Curtis and Miller 1980](#); [Rainbird et al. 2003](#)). Small
1597 insert depicts the main geological units of the Churchill-Wyoming craton and the location of the Thelon Basin
1598 (cross section built and modified after [Jefferson et al. 2011](#); [Hadlari and Rainbird 2011](#); [Pehrsson et al. 2013](#)).

1599
1600 **Fig. 2** Simplified geological map of the Kiggavik area (Orano internal document) and cross section from the Thelon
1601 fault to the Judge Sissons fault. Deposits and prospects are indicated with red and yellow circles, respectively.

1602
1603 **Fig. 3** Orientations of faults and breccias for each fracturing stage and for main deposits and prospects of the
1604 Kiggavik area, where available. The presence of each fracturing stage is relative to the same fracture set or to the
1605 same deposit/prospect. The chronology of the fracturing events was presented by [Grare et al. \(2018a\)](#). Schmidt's
1606 lower hemisphere stereoplots.

1607
1608 **Fig. 4** Drill core photographs (DCP) for different U deposits and prospects of the Kiggavik area. Numbers on the
1609 core boxes quantify the radioactivity (in count per second). **a** Uranium mineralized microbreccia (U0) crosscut by a
1610 quartz vein (yellow outline) of the QB. **b** Microbrecciated, uranium mineralized (U0) and unaltered psammo-pelitic
1611 gneiss of the Woodburn Lake Grp. **c** Various examples of uranium mineralized, grey-greenish altered fault zones of
1612 U2. White arrows on the picture from End locate mineralisation in fractures and parallel to foliation. **d** Disseminated
1613 U1 mineralization in 85W granite.

1614

1615 **Fig. 5** DCP for different U deposits and prospects of the Kiggavik area. **a** Spherulitic pitchblende (U₂) in hematized,
1616 clay altered microgranite. **b** Strongly clay altered, hematized fault rock (f₆) from Sleek (top). Vein cemented with
1617 hematite and uranium oxides (second stage of uranium mineralization-U₂, bottom). **c** Spherulitic pitchblende (U₂,
1618 white arrows) leaking out from Ca₂ veinlet (top). Spherulitic pitchblende and syngenetic hematite (bottom). **d** U₂
1619 mineralized, hematized fault damage zone. **e** Strongly clay altered, bleached but unmineralized fault zones (fault core
1620 highlighted in yellow, limits of the fault zone are delimited in green). **f** white clay altered fault zone (in yellow)
1621 crosscutting a U₂ mineralized fault zone. **g** Top and bottom: White clay altered cataclastic fault rock bearing small
1622 relict of spherulitic pitchblende (white arrow, unidentified generation). **h** Mackenzie diabase dike (black outline)
1623 crosscutting a uranium mineralized fault zone (red outline). The fresh diabase dike is not mineralized and weakly
1624 fractured.

1625
1626 **Fig. 6** Three examples of redox fronts with goethite (orange) remobilizing uranium oxides (grey-black products)
1627 from End, Kiggavik Main Zone and 85W.

1628
1629 **Fig. 7 a** DCP from the 85W prospect, Kiggavik area. Stepped subvertical, ENE-WSW quartz vein coated with
1630 uranium oxides showing evidence of dextral motion. **b** Field picture (FP). Stepped subvertical, NW-SE quartz vein
1631 displaying evidence of sinistral motion. **c** FP from the 85W area, Kiggavik area. Network of Mode I quartz veins (f₂)
1632 trending ESE-WNW. **d** Oriented data and kinematic of quartz veins, collected on outcrops. The St-Tropez area is
1633 located 20 km to the NNE of Kiggavik Main Zone. Schmidt's lower hemisphere stereoplots.

1634
1635 **Fig. 8 a** DCP from the Kiggavik Main Zone, Kiggavik area. Stepped veins of the first generation of calcite (Ca₁)
1636 coated with uranium oxides (U₁, red zones). **b** Oriented data and kinematics of Ca₁ veins from drillcores. Schmidt's
1637 lower hemisphere plots.

1638
1639 **Fig. 9 a** FP. NE-SW hematized fault zone (f₆) displaying dextral kinematics. **b** FP. ENE-WSW hematized fault-relay
1640 zone (f₆) displaying evidence of sinistral strike-slip kinematics. **c** Oriented data and kinematic of faults and
1641 microfaults (f₆), mainly from field observations but also collected on drillcores (i.e. Contact, Sleek and 85W).

1642
1643 **Fig. 10 a** FP from End area, Kiggavik area: Quartz veins of the quartz breccia (QB) being crosscut and offset
1644 (senestral motion) by late NNW-SSE to NW-SE microfaults. **b** DCP (top) and interpretation (bottom) from 85W
1645 prospect, of a uranium oxides (U₂) and a clay-cemented vein (orange outline) being crosscut and offset by a NW-SE
1646 microfault. Host rock is strongly altered. **c** Oriented data and kinematic of faults and microfaults, from field
1647 observations and from drillcores (i.e. Contact and 85W). **d** Simplified NNW-SSE cross-section of the Bong deposit,
1648 depicting dip-slip offset of the ore body by E-W oriented faults also driving fluids that strongly clay altered and
1649 bleached the host rock.

1650
1651 **Fig. 11** Micro-scale observations of U0 breccia from End deposit. **a, b, c** and **e**: Optical microphotograph (OMP), **d**
1652 and **f**: SEM pictures. **a** Undulated microstructures cemented with chlorite and uranium oxides. **b** Mineralized
1653 microbreccia: corroded clasts (yellow outline) cemented by chlorite and opaque minerals (sulfide, uranium oxides
1654 and rutile indicated by white arrow). **c** Mineralized microbreccia crosscut by a quartz (qtz) vein of QB. **d** SEM
1655 microphotograph and element mapping of U-S-Ti compounds. **e** Microbreccia with chlorite (Chl, dark green)
1656 crosscut by a quartz vein of QB and altered to sudoite (Sud, light green). **f** SEM microphotograph. Anhedronal rutile
1657 (Rt), uraniferous titanate (Ti-U) and pitchblende (Pch).

1658
1659 **Fig. 12** SEM microphotographs of different U mineralization from the Kiggavik area: **a** Microbreccia cemented with
1660 uranium oxides and subhedronal brannerite and uraniferous titanate (Ti-U). **b** Anhedronal uraniferous titanate coating
1661 rutile grains with pitchblende micro-inclusions (U). **c** Magmatic quartz displaying a micro-fracture cemented with
1662 colloform pitchblende and anhedronal rutile. **d** Uraninite displaying various state of alteration, cemented by calcite. **e**
1663 Quartz vein showing traces of dissolution and colloform pitchblende. **f** Ni-bearing pyrite (bravoite) and pyrite (Py)
1664 with concentric uranium growth zone. **g** Quartz vein crosscut by Galena (Gal)-Ag-U cemented microfracture. **h**
1665 Pitchblende displaying micro-inclusions of gold. **i** Aluminum-phosphate-sulfate (APS) embedded in anhedronal
1666 pitchblende and pyrite, in f5 fault zone. **j** APS observed in altered and oxidized granite proximal to f6 fault. **k** U2-f6
1667 stage: Anhedronal pitchblende cementing anastomosing fracture. **l** U3 pitchblende coating quartz and clay minerals.

1668
1669 **Fig. 13** Cathodoluminescence microphotograph (CLMP) and OMP **a**. Dolomite (Dol) corroded and coated with
1670 pitchblende and a first generation of calcite (Ca1). The calcite (Ca1) cements a distinct area separating pitchblende
1671 (U1) and dolomite. **b** Microbreccia cemented with calcite (Ca1) and synchronous pitchblende (U1). **c** Pitchblende
1672 (U1) within a matrix of calcite (Ca1). **d** Dolomite brecciated and cemented by calcite (Ca1) and synchronous
1673 pitchblende (U1). **e** Pitchblende (U1) crosscut by calcite micro veinlet. **f** Same picture as **e** observed under
1674 cathodoluminescence, the typical crack-seal texture of the second generation of calcite Ca2 is observable.

1675
1676 **Fig. 14 a** Chemiographic representation of chlorites analysed from different locations in the Kiggavik area (Jane,
1677 Contact, 85W, Andrew Lake). **b** Chemiographic representation of chlorite grains formed during U0 mineralizing
1678 stage and their later hydrothermal alteration. Structural formulas of chlorites were plotted in a MR3-2R3-3R2
1679 diagram (Velde 1985). **c** OMP of a U0 microbreccia cemented with unaltered dioctahedral chlorite (1. dark green),
1680 altered to light green di-trioctahedral chlorite (2. sudoite). Opaque minerals are ore minerals. Numbers localize the
1681 point analysed under EMPA, which results are plotted in B. **d** Electron microprobe analysis of chlorites from the U0
1682 mineralized microbreccia, and calculated temperatures after several techniques.

1683
1684 **Fig. 15 a** Analyzed white mica plotted on a ternary diagram of the average compositional fields of dioctahedral
1685 mica-like phases, after Dubacq et al. (Dubacq et al. 2010). Pr: pyrophyllite; Cel: celadonite; Ms: muscovite; Pg:

1686 paragonite. **b** Pre-ore white mica in a fracture cemented by white mica in link with U1. **c** Pre-ore white mica in a
1687 micro-fracture reopened and cemented by white mica in link with U2. **d** Reworked clasts of ore minerals with second
1688 stage white mica, in a matrix cemented by late ore white mica. **e** Temperatures deduced from the composition of
1689 various generations of white mica (EMPA).

1690
1691 **Fig. 16** Chondrite-normalized REE patterns for pitchblende and uraninite from 8 different samples from Andrew
1692 Lake (Top left), End (Top right) and 85W (bottom right). Each curve corresponds to an *in situ* SIMS or LA-ICP-MS
1693 REE analysis in a selected U-oxide of the studied samples. Ages for the samples were obtained in this study (see also
1694 Fig. 17), except for sample 9568-38 and 9568-39, obtained by Lach (2011). The grey zones corresponds to the
1695 unconformity-related uranium oxide reference chondrite-normalised REE patterns from the Mc Arthur River and Sue
1696 deposit (Mercadier et al. 2011b), Kalongwe deposit (Eglinger et al. 2013), Centennial and Millenium deposits
1697 (Alexandre et al. 2015).

1698
1699 **Fig. 17** $^{206}\text{Pb}/^{238}\text{U}$ - $^{207}\text{Pb}/^{235}\text{U}$ Concordia diagram showing the isotopic composition of uranium oxides (pitchblende
1700 and uraninite) from six samples coming from End (9568-38), Andrew Lake (9850, 9851, And-15-01-04, And-15-01-
1701 05) and 85W (85W-10-04). Analytical data are available as complementary material.

1702
1703 **Fig. 18** Thick section pictures. **a** Magmatic quartz from the granite of 85W displaying monophase FIPs (red) crosscut
1704 by aqueous FIPs (blue). **b** Monophase fluid inclusion displaying negative crystal shape. **c** Biphase aqueous fluid
1705 inclusion. **d** Triphase aqueous fluid inclusion with halite crystal. **e** Monophase FIPs (red dotted lines) and aqueous
1706 FIP (blue dotted line). Monophase FIs are obliterated at the intersections between monophase and aqueous FIPs.

1707
1708 **Fig. 19** Concentration (ppm) in several metals for selected secondary fluid inclusions in the Kiggavik area.
1709 Comparison is made with data from the Athabaca basin (grey bars, Richard et al. 2016).

1710
1711 **Fig. 20** Directions for type 1 (red) and type 2 (blue) FIPs, for 85W (left) and Contact (right). Mean granitic gneiss
1712 foliation at Contact is given. The general dip for the FIPs is sub-vertical.

1713
1714 **Fig. 21** Scheme summarizing ages obtained within the Thelon/Baker-Lake area, through U-Pb isotopes on uranium
1715 oxides (Farkas 1984; Miller et al. 1986; J. Bridge et al. 2013; Lach et al. 2013; Sharpe et al. 2015b; Chi et al. 2017;
1716 Shabaga et al. 2017; This study), Ar-Ar ages on illite (Friedrich et al. 1989; Riegler 2013; Ashcroft et al. 2017;
1717 Shabaga et al. 2017), Ar-Ar on muscovite (Ashcroft et al. 2017; Shabaga et al. 2017), K-Ar on illite (Friedrich et al.
1718 1989) and whole rock analysis (Hunt and Roddick 1988, 1992a, b).

1719
1720 **Fig. 22** Synthesis of oriented data with kinematic indicators and derived paleostress interpretation (black arrows). **a**

1721 macro scale data. **b** micro scale data

1722

1723 **Fig. 23** Pre-Thelon basin first stage of micro-brecciation and uranium mineralization in the Kiggavik area associated
1724 with magmatism of the Kivalliq igneous suite. **a** bloc diagram. **b** Map view of the fracture network at this stage.

1725

1726 **Fig. 24** F2/QB. Pre-Thelon hydraulic quartz breccia linked to magmatism of the Kivalliq igneous suite (ca. 1750
1727 Ma). ESE-WNW oriented σ_1 and NNE-SSW oriented σ_3 . **a** bloc diagram. **b** Map view of the fracture network at this
1728 stage.

1729

1730 **Fig. 25** F5/U1. Syn-Post Thelon circulation of basinal brines. ESE-WNW oriented σ_1 and NNE-SSW oriented σ_3 . **a**
1731 bloc diagram. **b** Map view of the fracture network at this stage.

1732

1733 **Fig. 26:** F6/U2. Post-Thelon renewed circulation of basinal brines. ENE-WSW oriented σ_1 and NNW-SSE oriented
1734 σ_3 . **a** bloc diagram. **b** Map view of the fracture network at this stage.

1735

1736 **Fig. 27:** Post ore, Pre Mackenzie dikes (1267 Ma) illitization and desilicification, local remobilization and offsetting
1737 of orebodies. NNE-SSW oriented σ_3 . **a** bloc diagram. **b** Map view of the fracture network at this stage.

1738

1739 **Table 1** selected representative chlorite analysis from different deposits/prospects of the Kiggavik area.

1740

1741 **Table 2** Summary of microthermometric fluid inclusions data obtained in this study for aqueous biphasic and triphasic
1742 fluid inclusions (type 2 FIP). Te: Temperature of eutectic. Tm ice: melting temperature of the last crystal of ice. Ts
1743 NaCl: Fusion temperature of the crystal of halite. Classification of fluid inclusions (after [Derome et al. 2005](#)).

Table 1

Location	End U0	End U0*	Contact U2	Jane U1	Jane U2	End	Kiggavik MZ U2	85W U1
SiO ₂	27,05	36,33	36,97	36,02	35,23	36,49	34,59	35,29
Al ₂ O ₃	20,21	28,81	34,45	33,98	35,74	30,09	35,17	32,31
K ₂ O	0,02	0,54	0,88	0,74	0,25	0,27	1,96	0,92
CaO	0,03	0,1	0,15	0,17	0,02	0,04	0,15	0,18
FeO	26,5	4,17	0,96	0,12	0,17	2,24	0,5	0,86
MgO	15,61	16,93	12,28	14,72	15,04	17,13	13,41	15,87
MnO	0,35	0,03	0,02	0	0	0,06	0	0,03
TiO ₂	0,11	0	0	0	0	0	0	0
Na ₂ O	0,06	0,02	0,04	0	0,04	0,08	0	0,06
Total	90,08	86,96	85,81	85,75	86,49	86,46	85,78	85,52

Table 1: selected representative chlorite analysis from different deposits/prospects of the Kiggavik area.

Table 2

FI type		% vapor phase	Microthermometric data (°C)				Salinity (Wt% NaCl+CaCl ₂)	
			Te	Tm ice	Ts NaCl	Th		
85W	Lw'	10-50	-85 to -	-45,4 to -	207 to	100 to 215	25,0 to 29,3	
	Range		66	30,6	223			
	Mode		-70					
		n		5	6	2	6	6
	Lwh'	5-40	-80 to -	-45,8 to -	121 to	62 to 136	24,4 to 29,4	
	Range		60	22,8	222			
	Mode		-70	-38,5				
		n		17	19	11	8	19
	Lw''	5-90	-65 to -	-23,9 to -1,4		208 to 215	2,3 to 22,3	
Range	38							
Mode	-60							
	n		9	16			16	
Contact	Lw1	10-30	-77	-28,9 to -			23,2 to 24,4	
	Range			25,9				
	n		1	2				
	Lw'	10	-75	-31,4		92,0	25,3	
	Range							
	n		1	1				
	Lwh'	10			155 to	81,8 to		
	Range				168			
	n				3			4
Lw''	30		-16,6			19,8		
Range								
n			1				1	

Figure 1

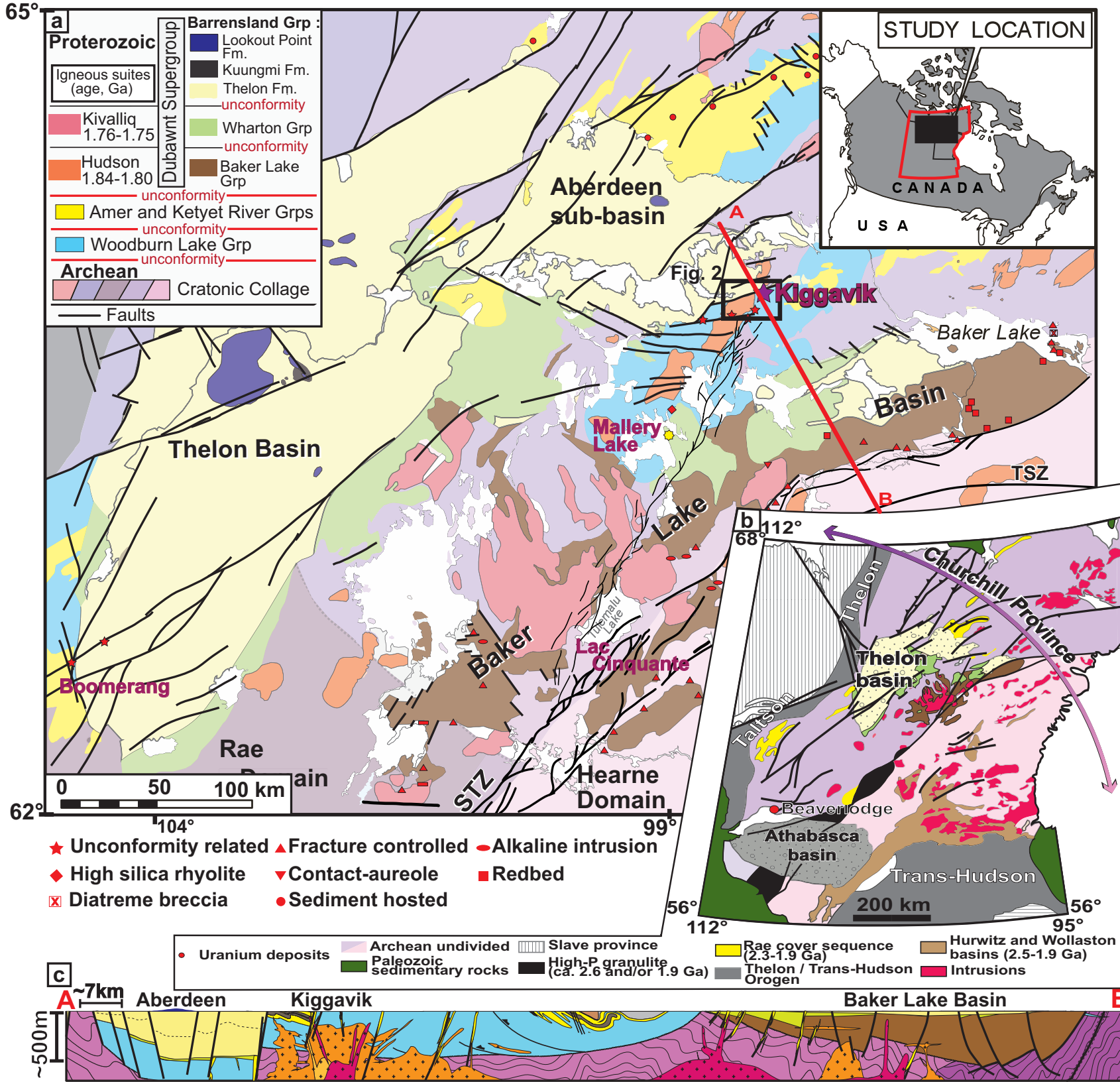


Figure 2

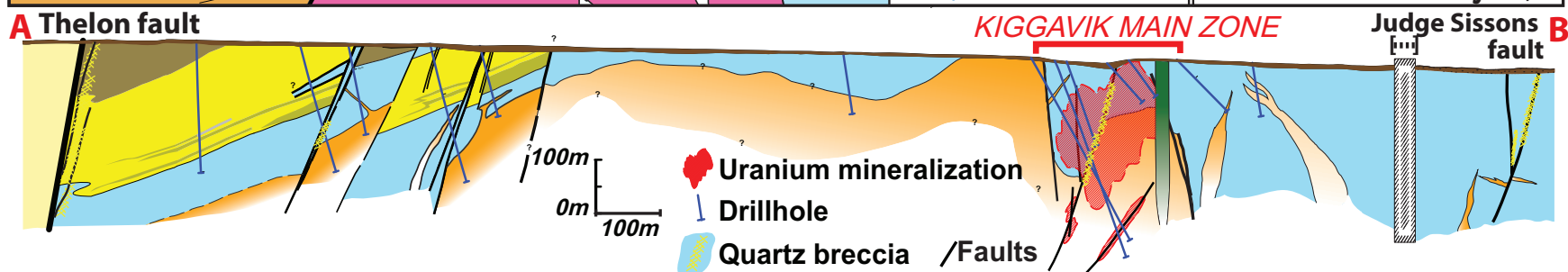
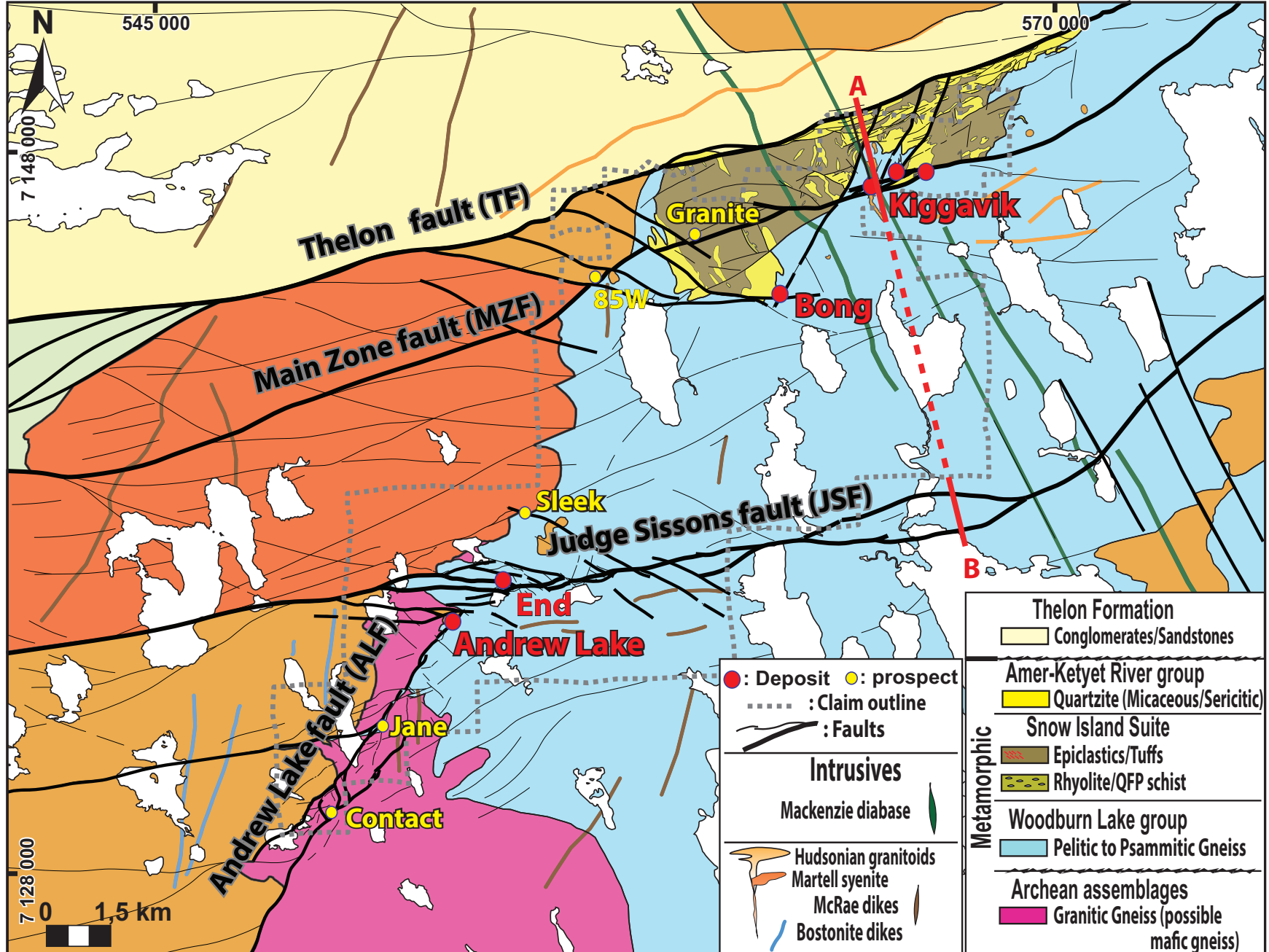
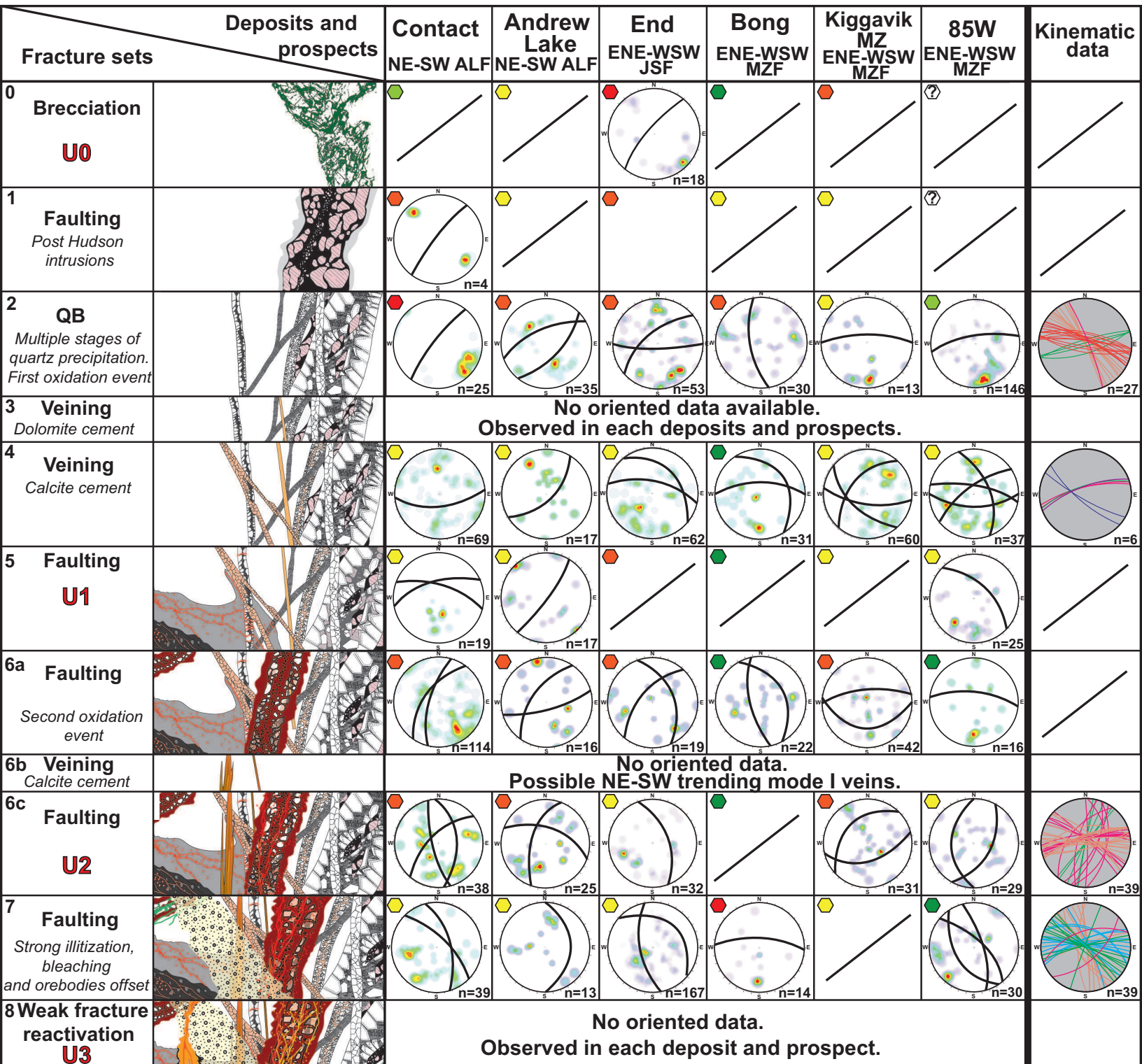


Figure 3



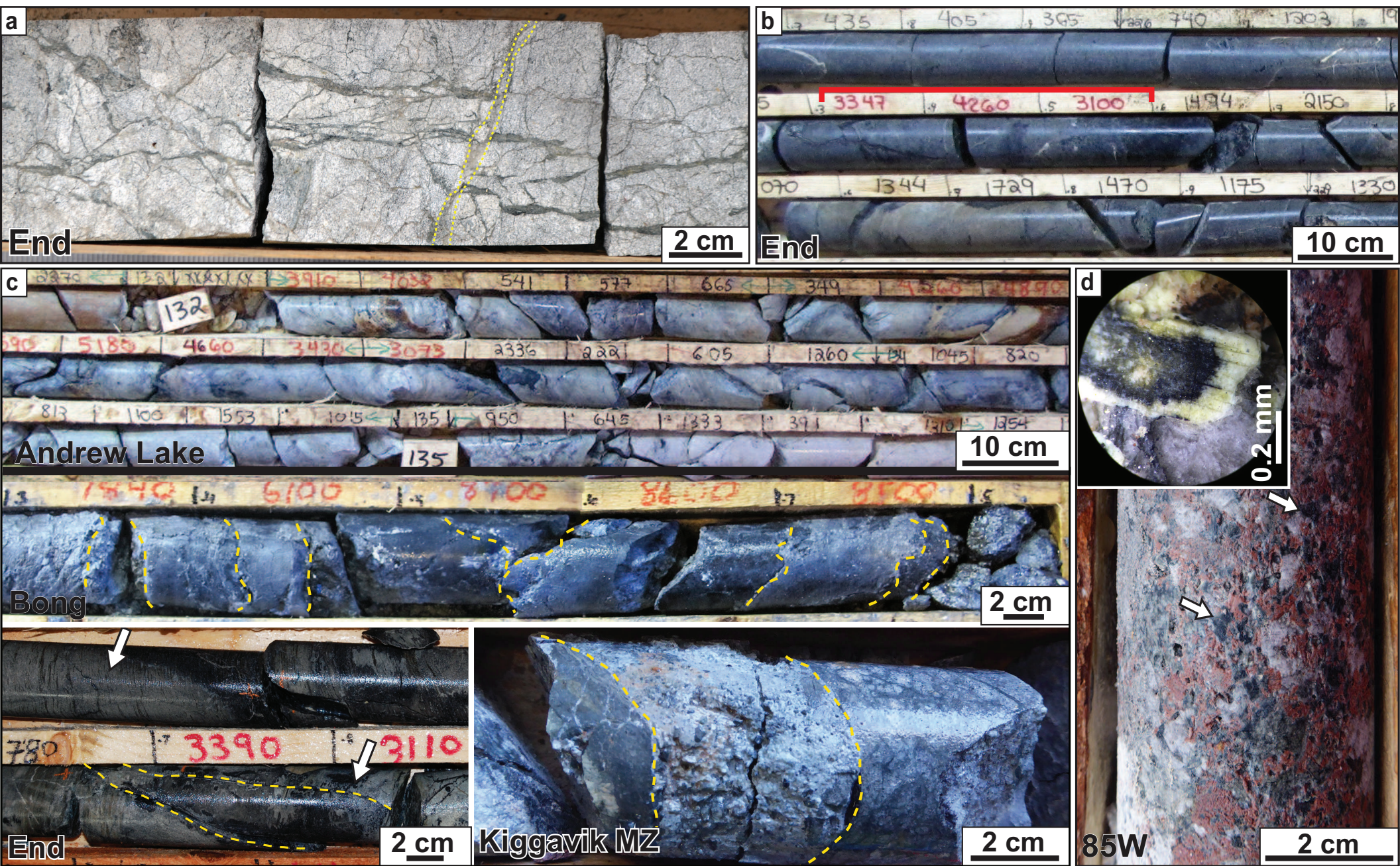
Presence of each fracturing stage:

- Less present/observed
- More present/observed
- More present/observed

Observed slip component:

- dextral
- dextral and normal
- dextral and reverse
- sinistral
- sinistral and normal
- sinistral and reverse
- normal
- reverse
- Mode I veins

Figure 4



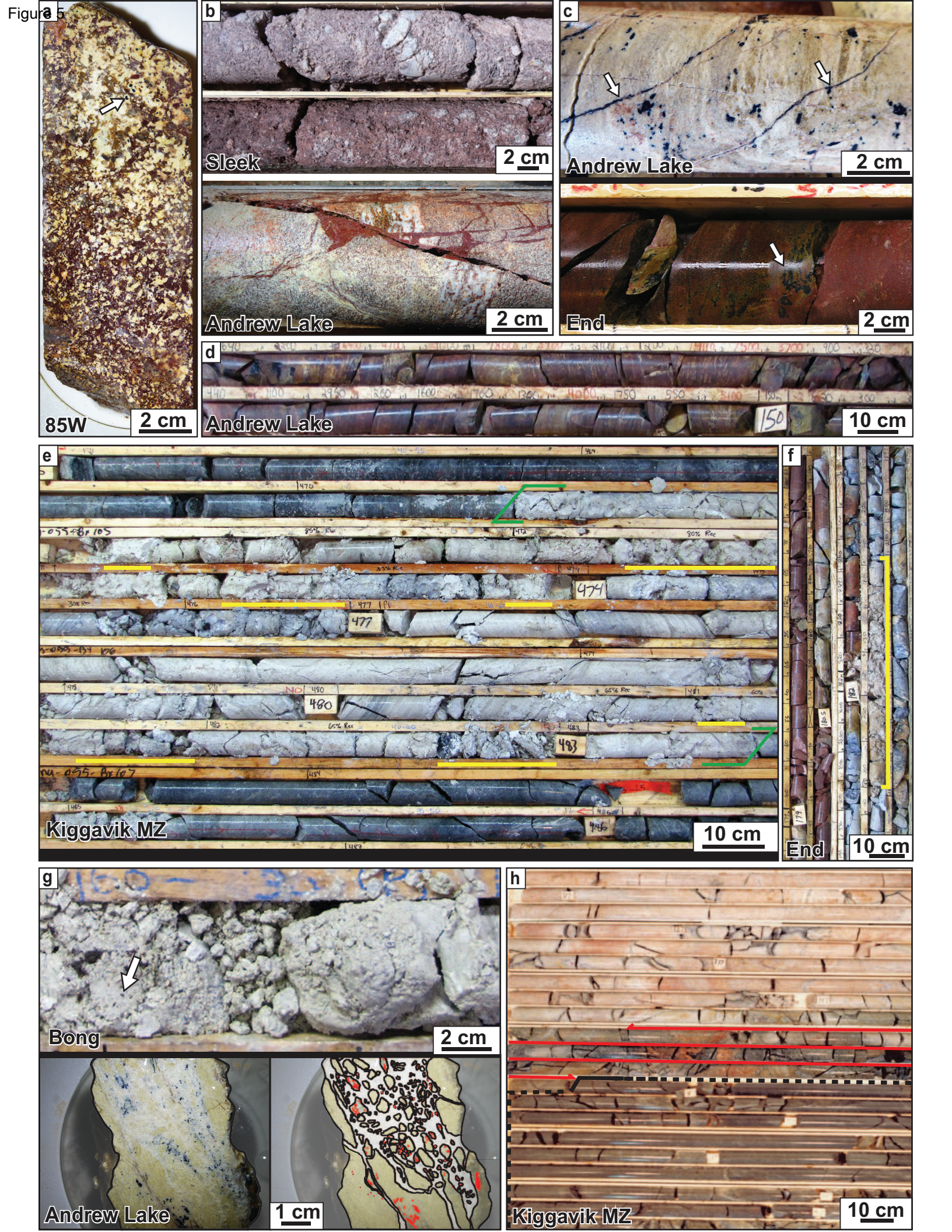


Figure 6

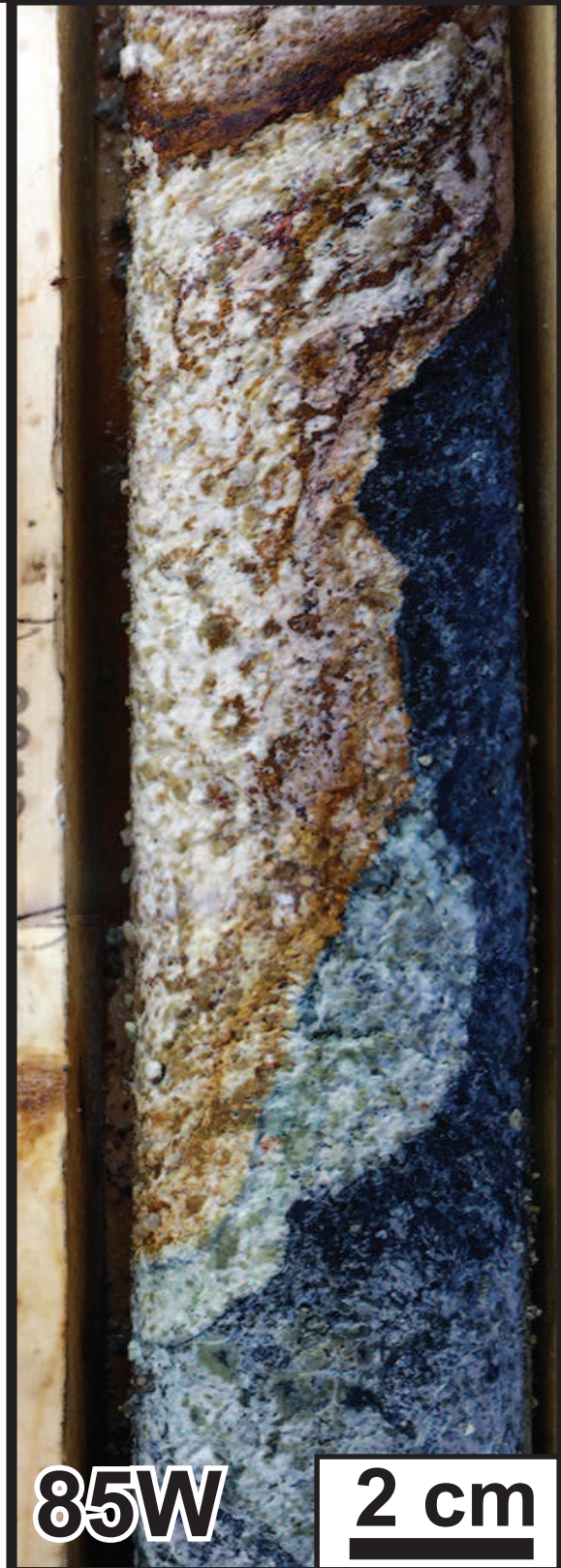


Figure 7

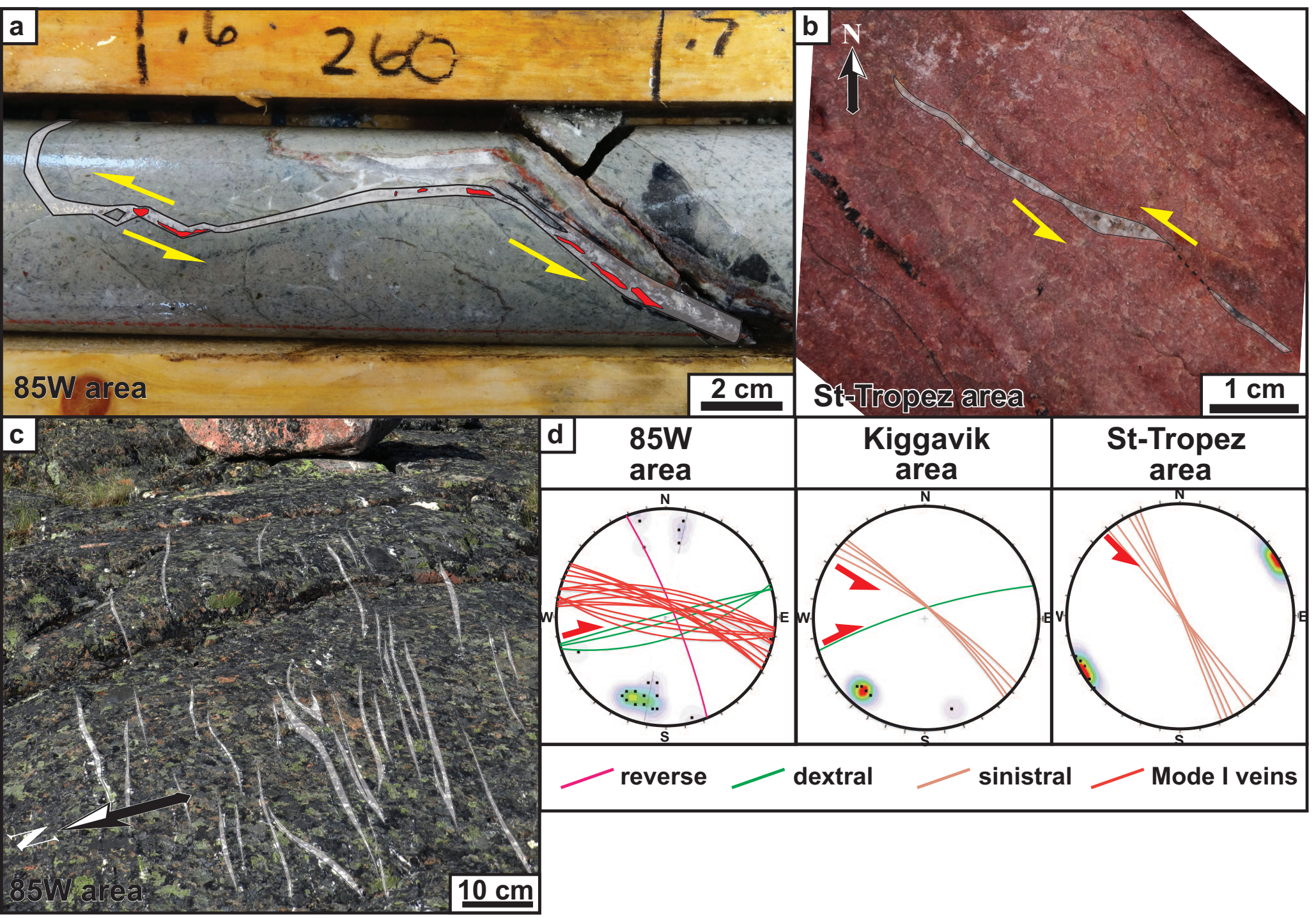


Figure 8

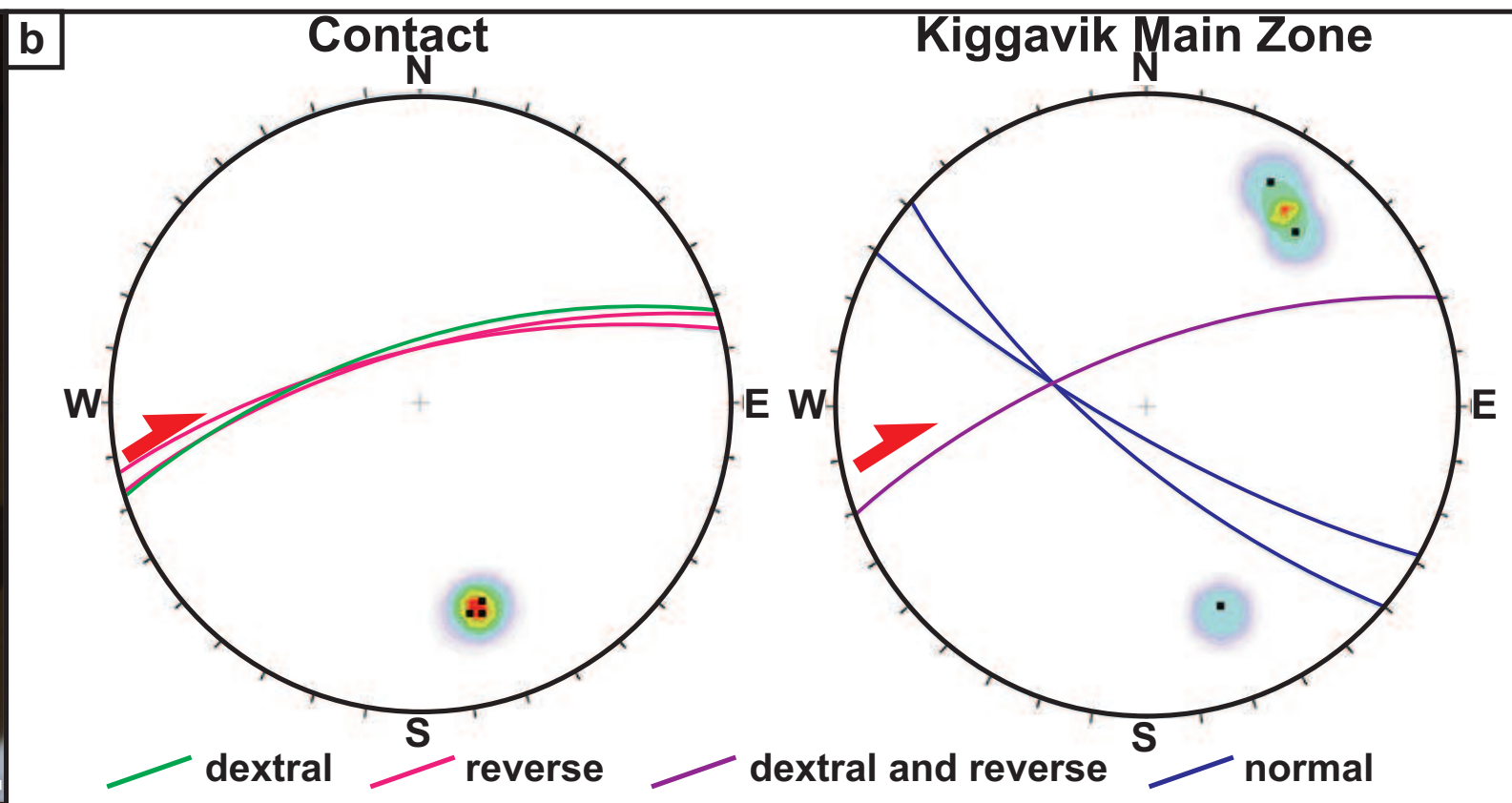


Figure 9

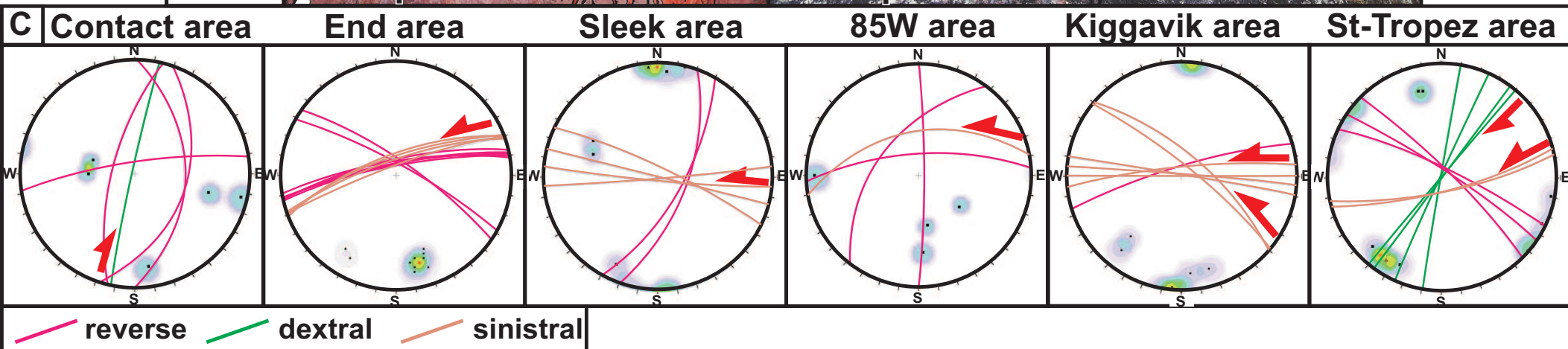
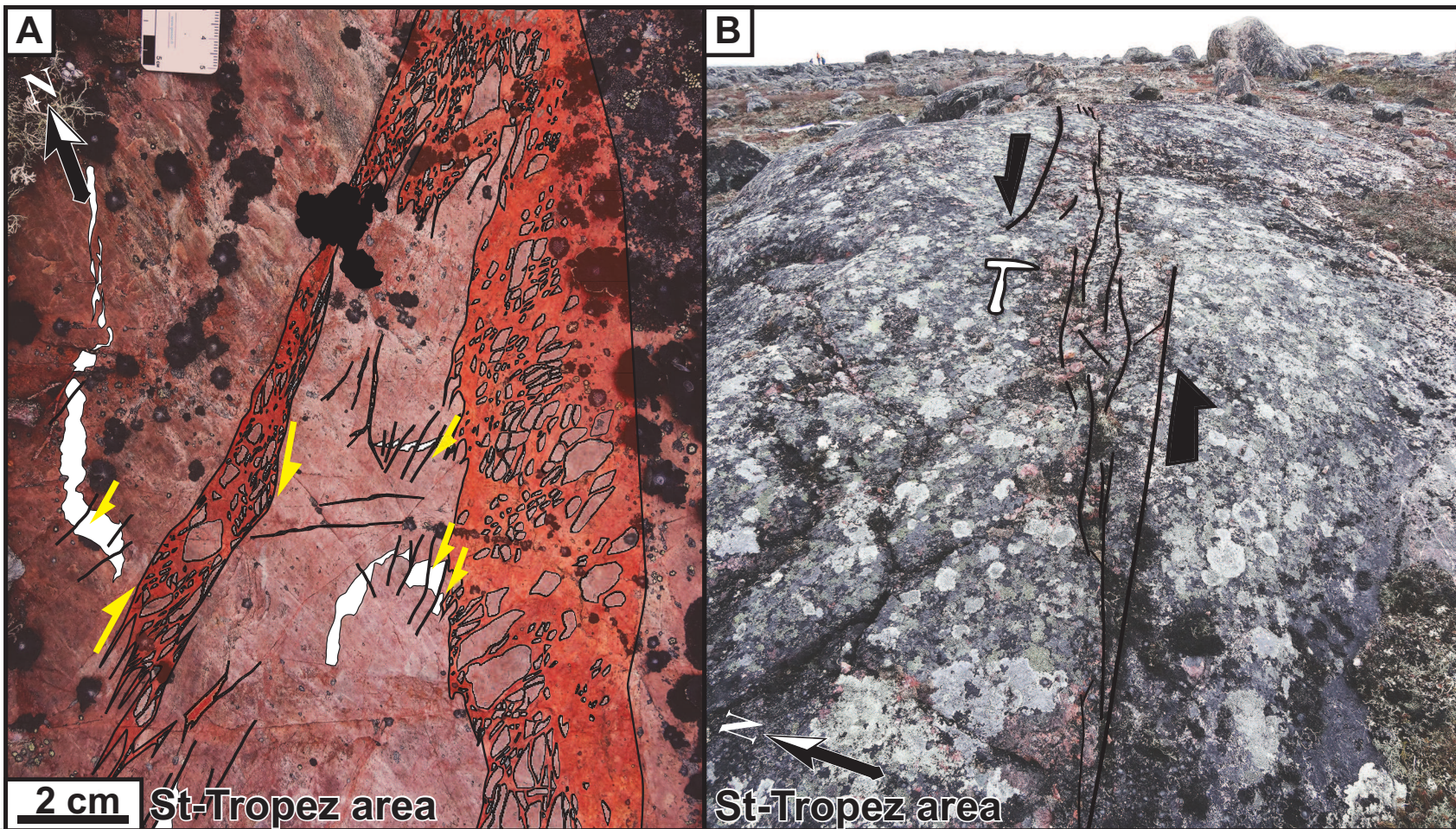


Figure 10

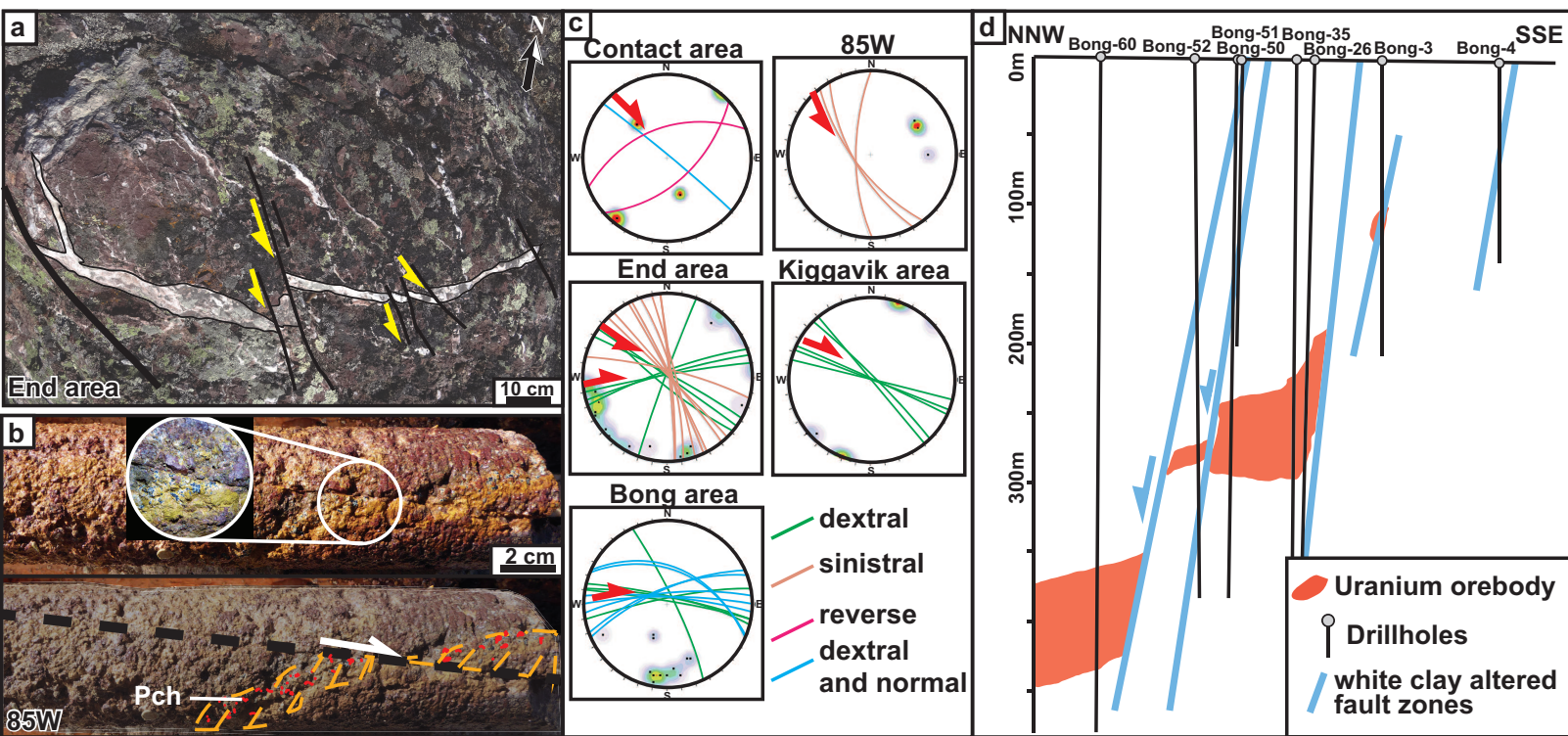


Figure 11

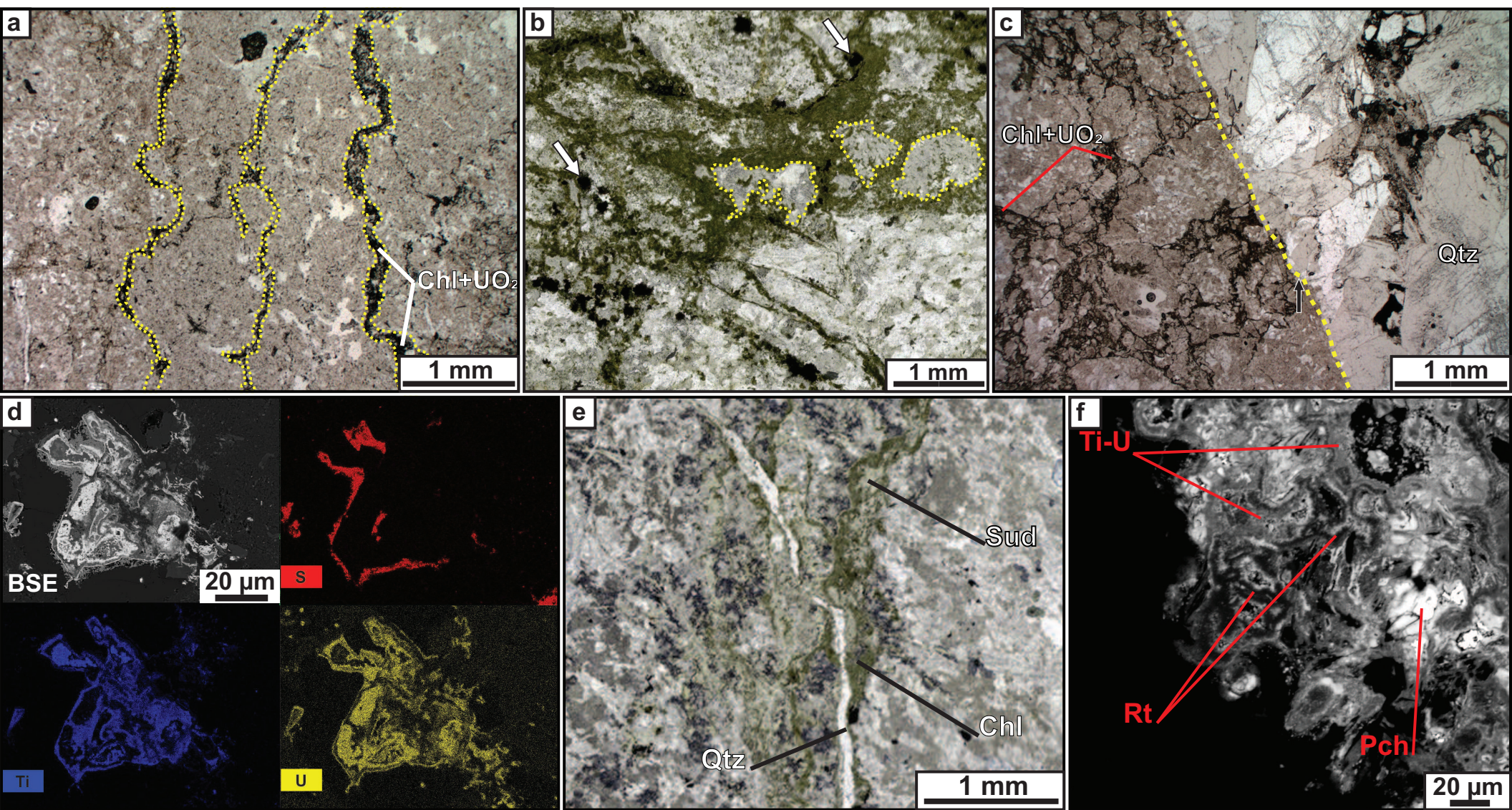


Figure 12

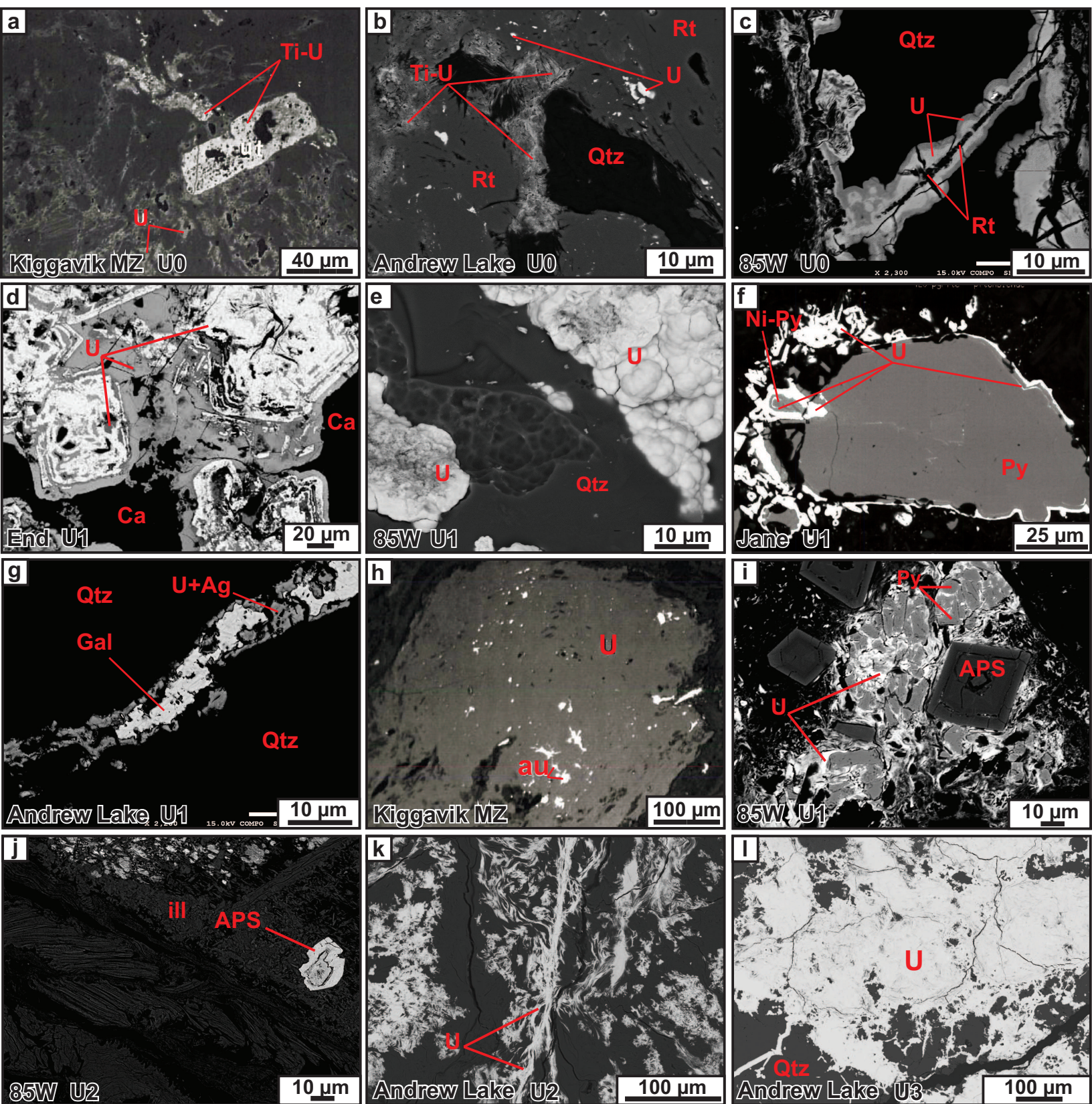


Figure 13

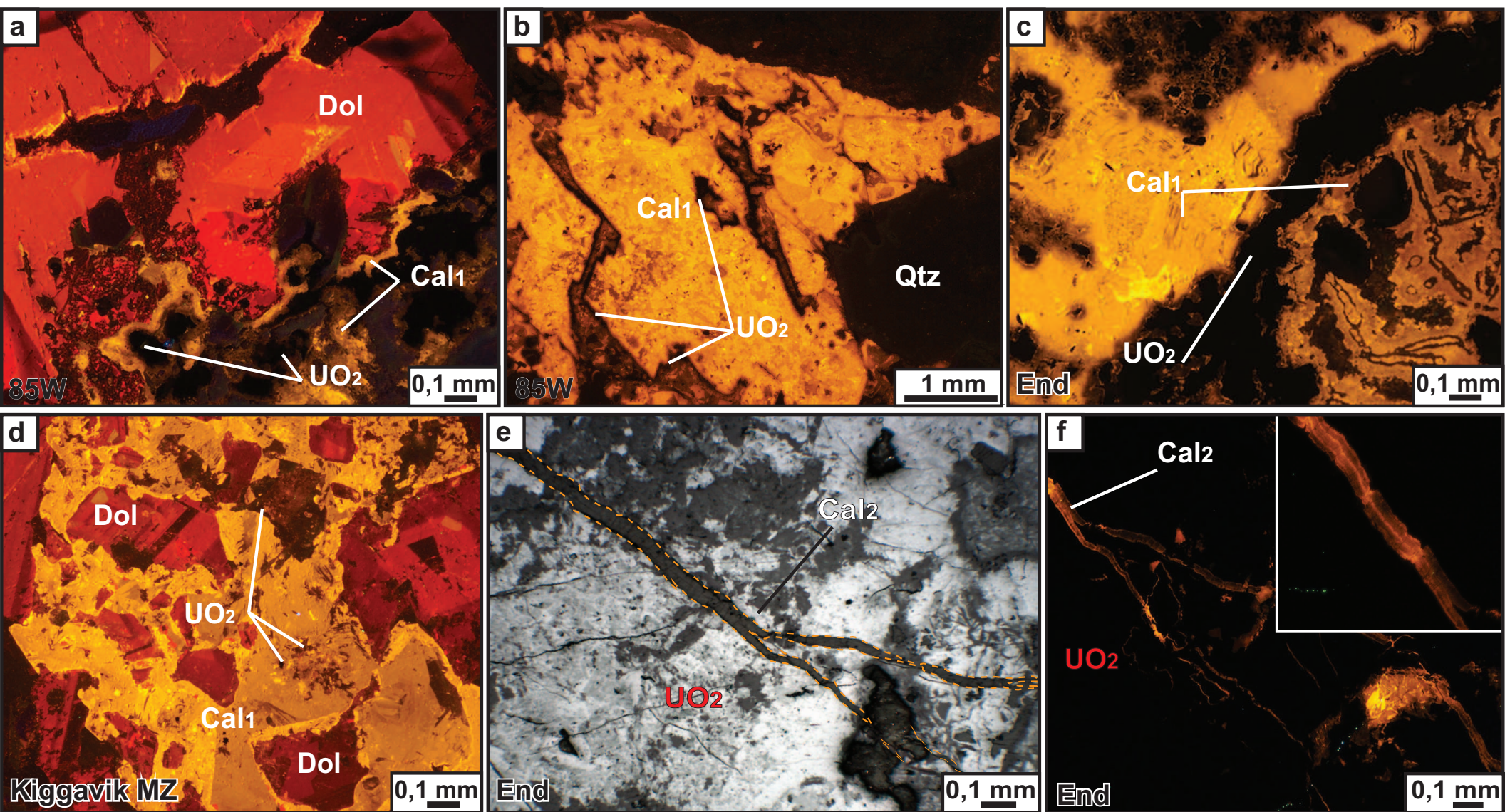
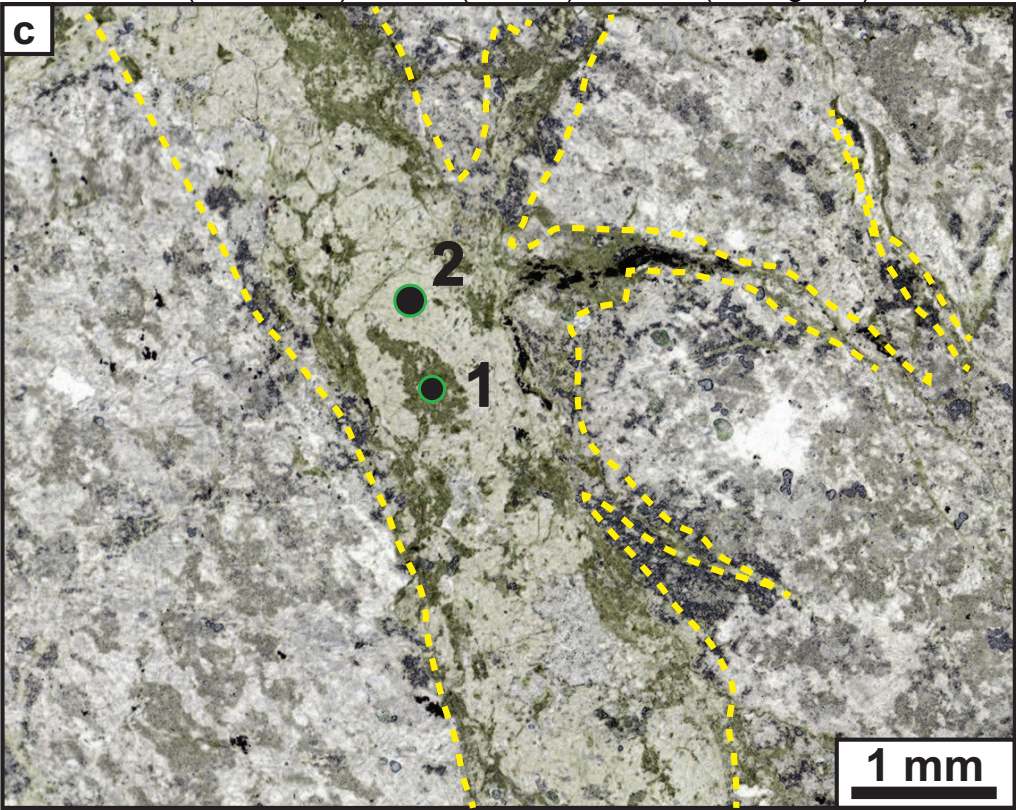
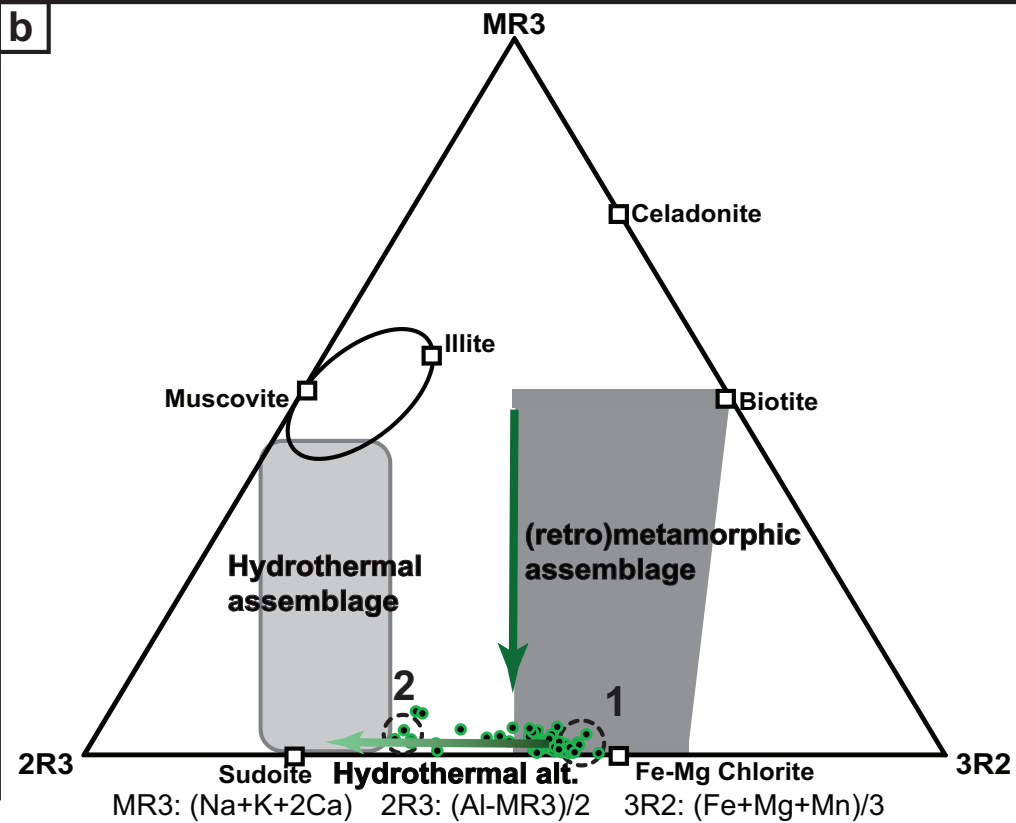
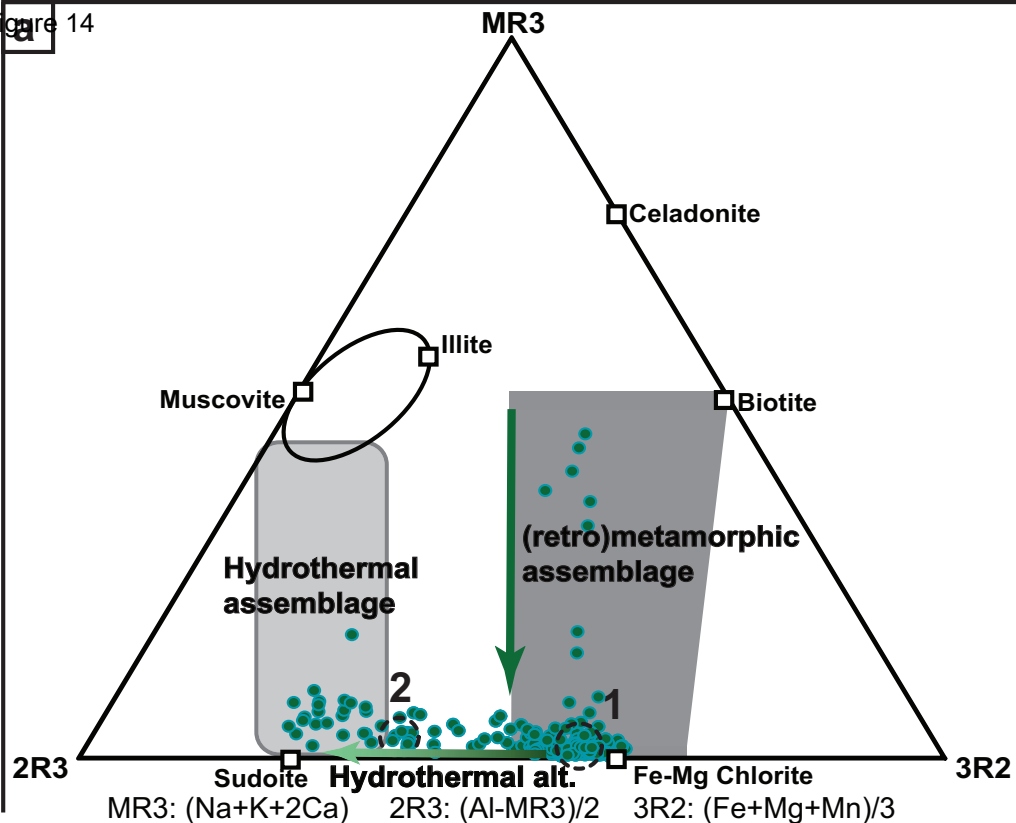


Figure 14



d

Unaltered (U0) chlorite

Sample	8561-9	8561-9	8561-9	8494-8	8548-14
Al_{total}	2,36	2,23	2,52	2,42	2,51
Al^{IV}	1,23	1,17	1,33	1,20	1,14
Al^{VI}	1,13	1,07	1,19	1,22	1,37
Mg	2,62	2,87	2,39	2,37	2,38
Fe	2,18	2,08	2,43	2,34	2,07
Occ	5,94	6,02	6,01	5,94	5,82
XFe:Fe/(Fe+Mg)	0,45	0,42	0,50	0,50	0,47
Calculated T°C of formation					
Cathelineau, 1988	333	314	366	324	306
Jowett, 1991	322	303	355	313	295
Kranidiotis, 1987	148	142	159	145	139
Zang & Fyfe, 1995	137	134	143	130	127

Figure 15

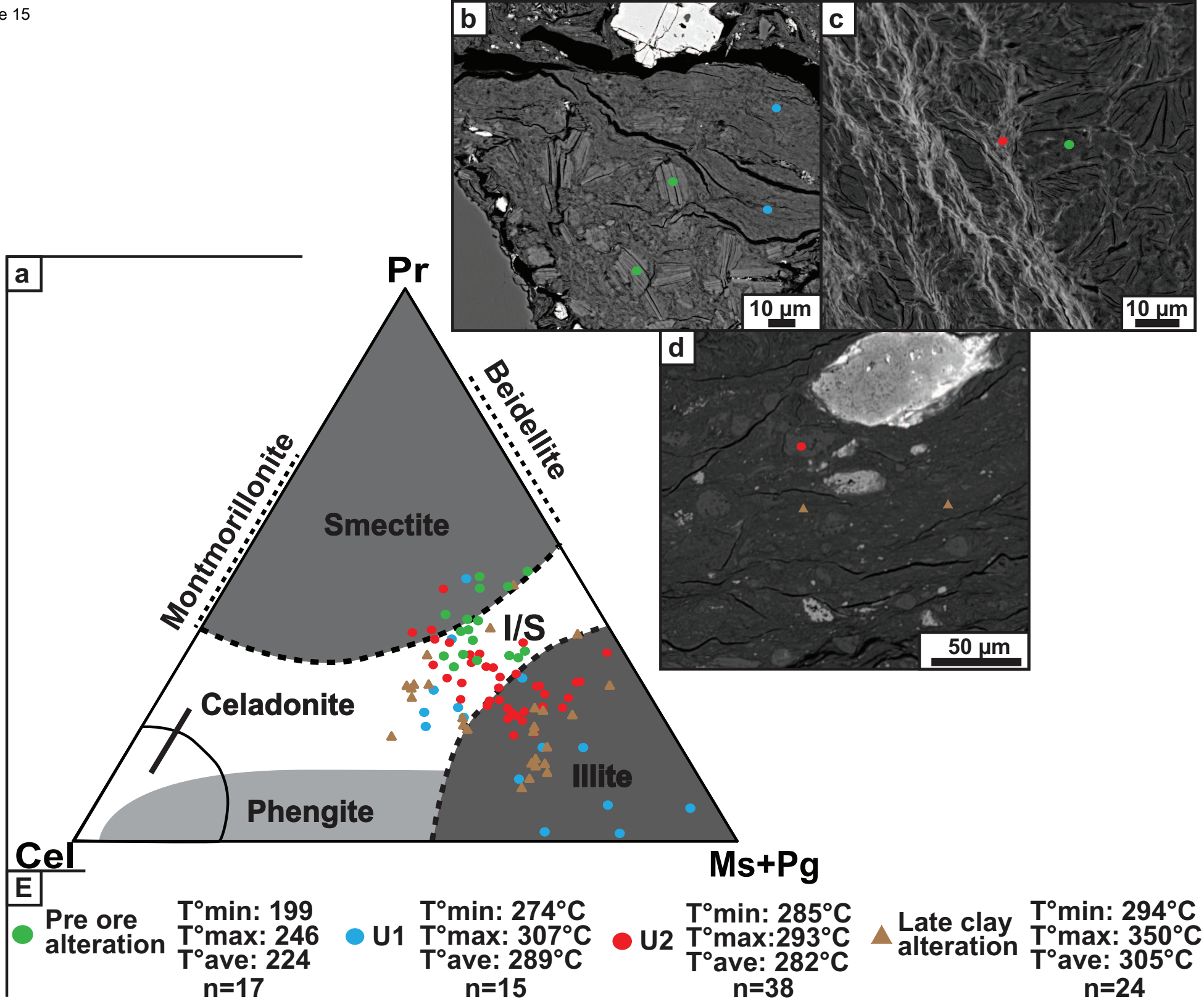
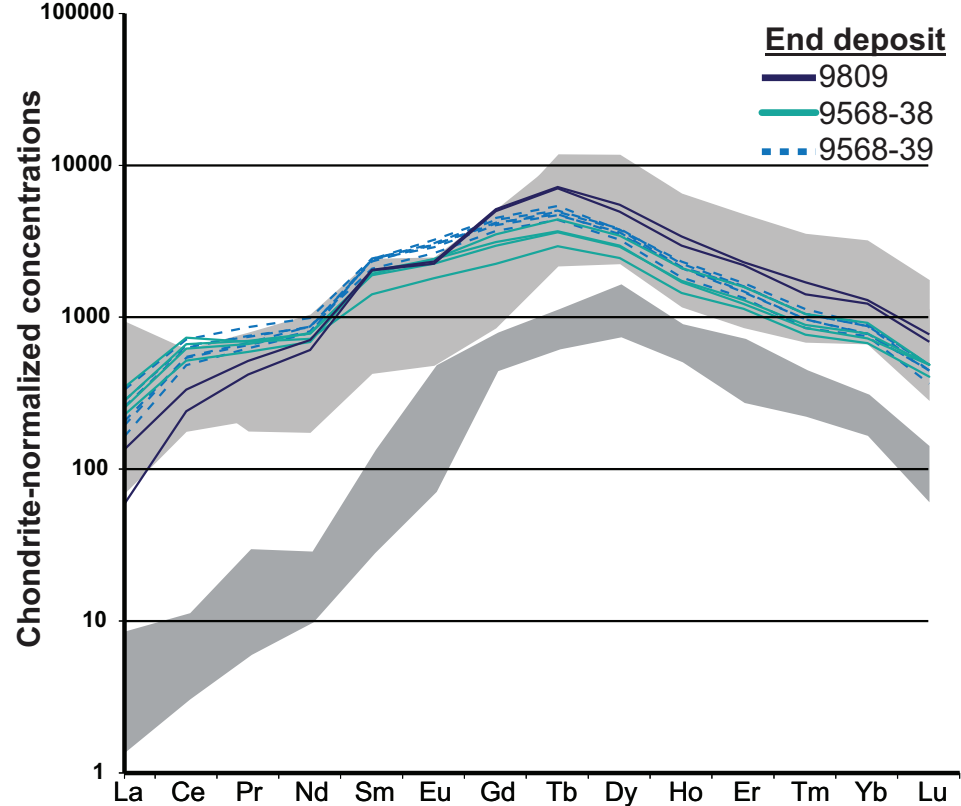
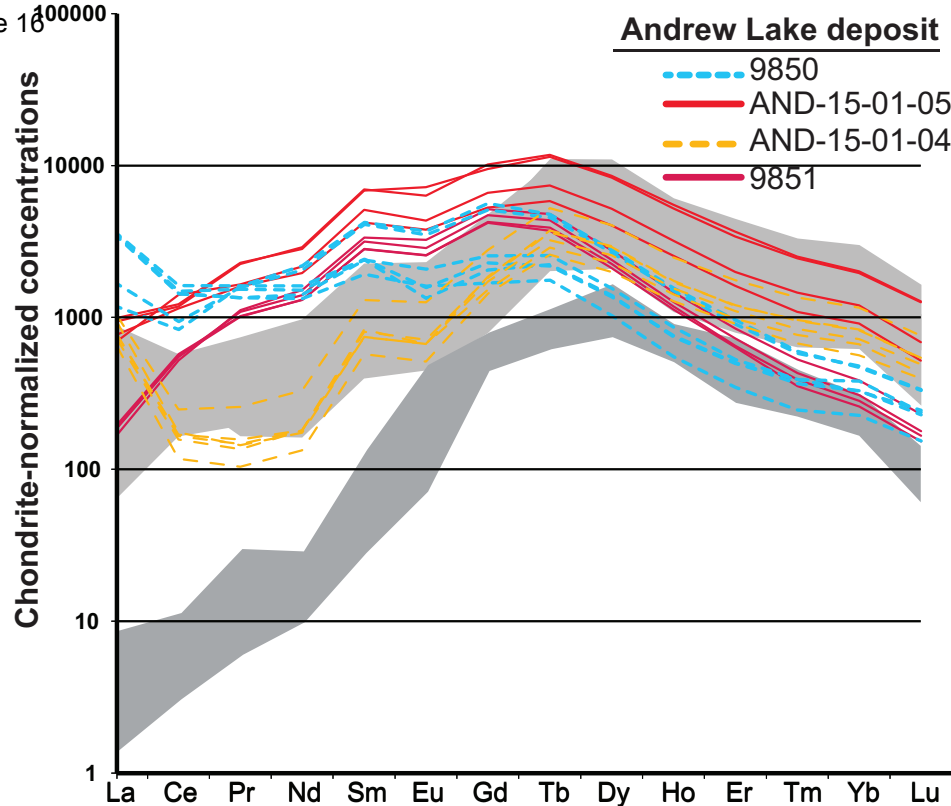


Figure 16

**Location and sample****Umin stage****Ages****Andrew Lake deposit**

9850	U1 (?)	354±47 Ma
AND-15-01-05	U2	565±38 Ma
AND-15-01-04	U3	547±13 Ma
9851	U2	345±19 Ma

End deposit

9809	U1	1239±75 Ma
9568-38	U1	1293±08 Ma
9568-39	U1	1187±20 Ma

85W prospect

85W-10-04	U?	1073±5.5 Ma
-----------	----	-------------

Centennial and Millenium

McArthur River and Sue

Kalongwe

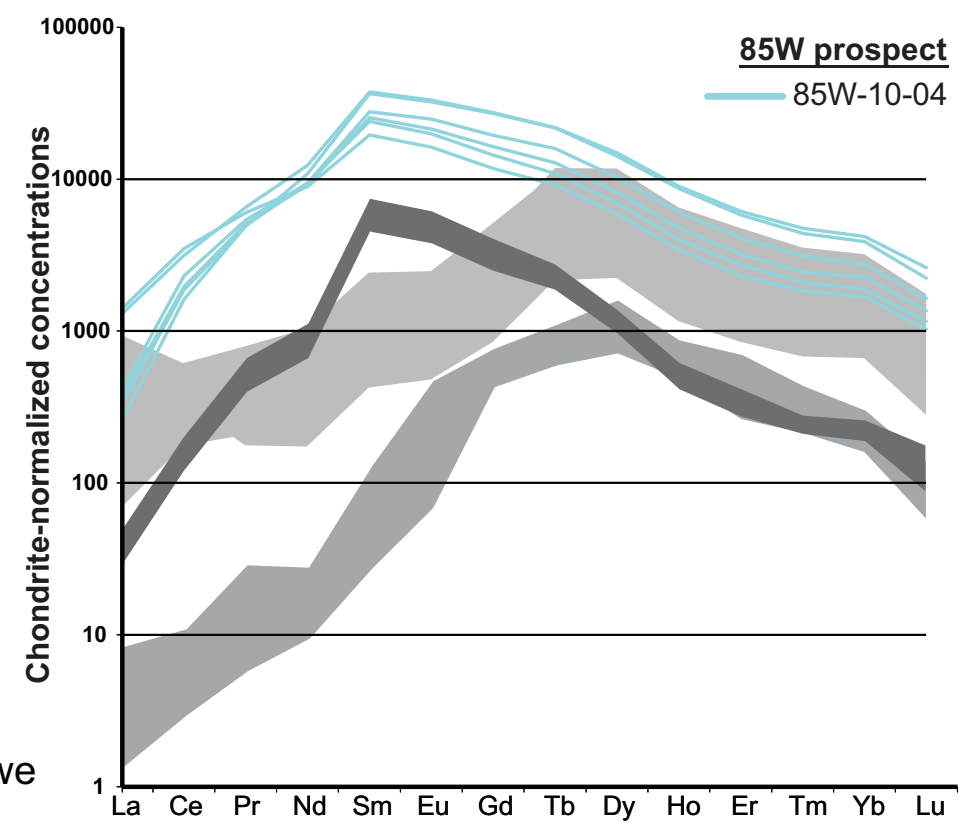


Figure 17

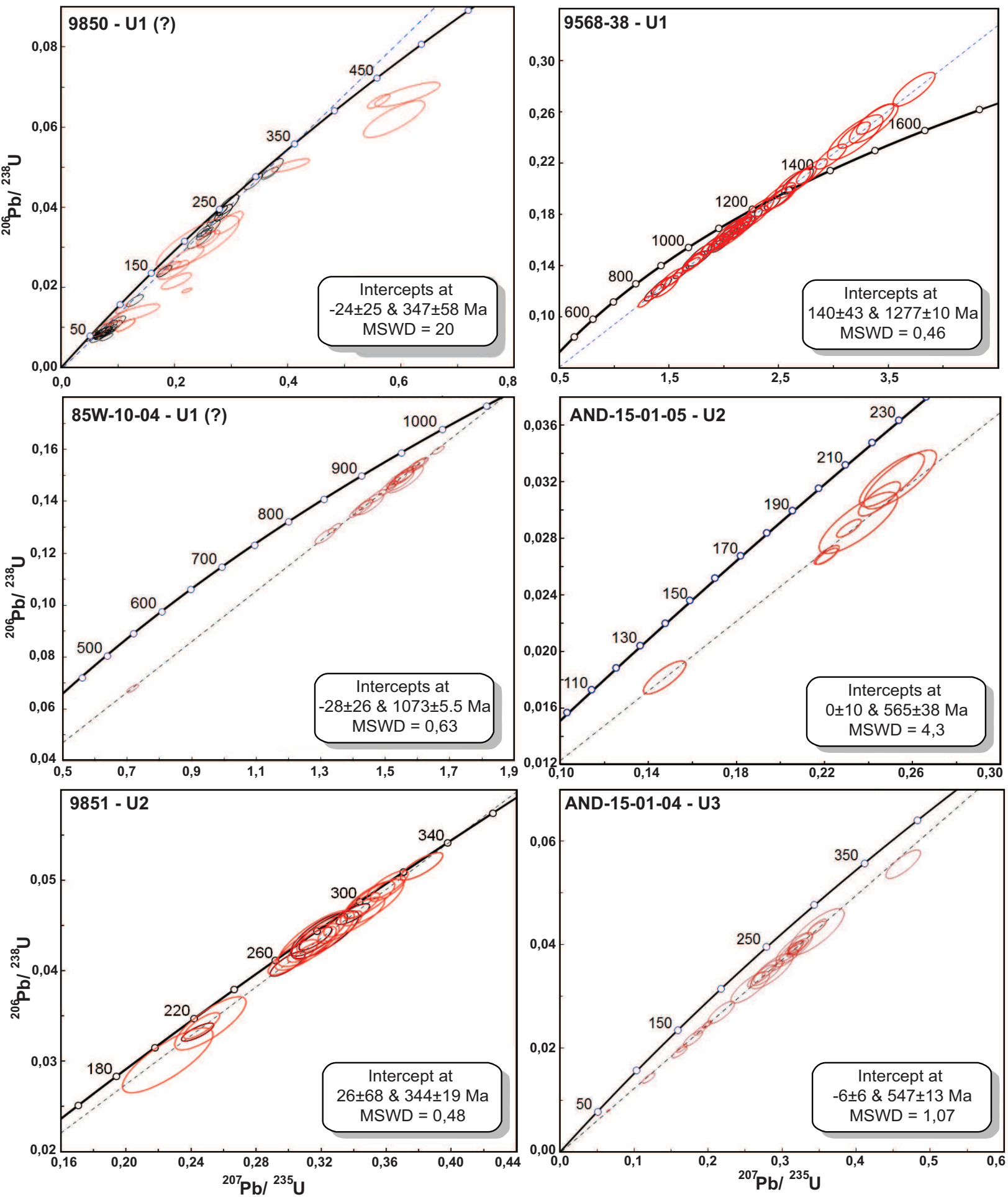
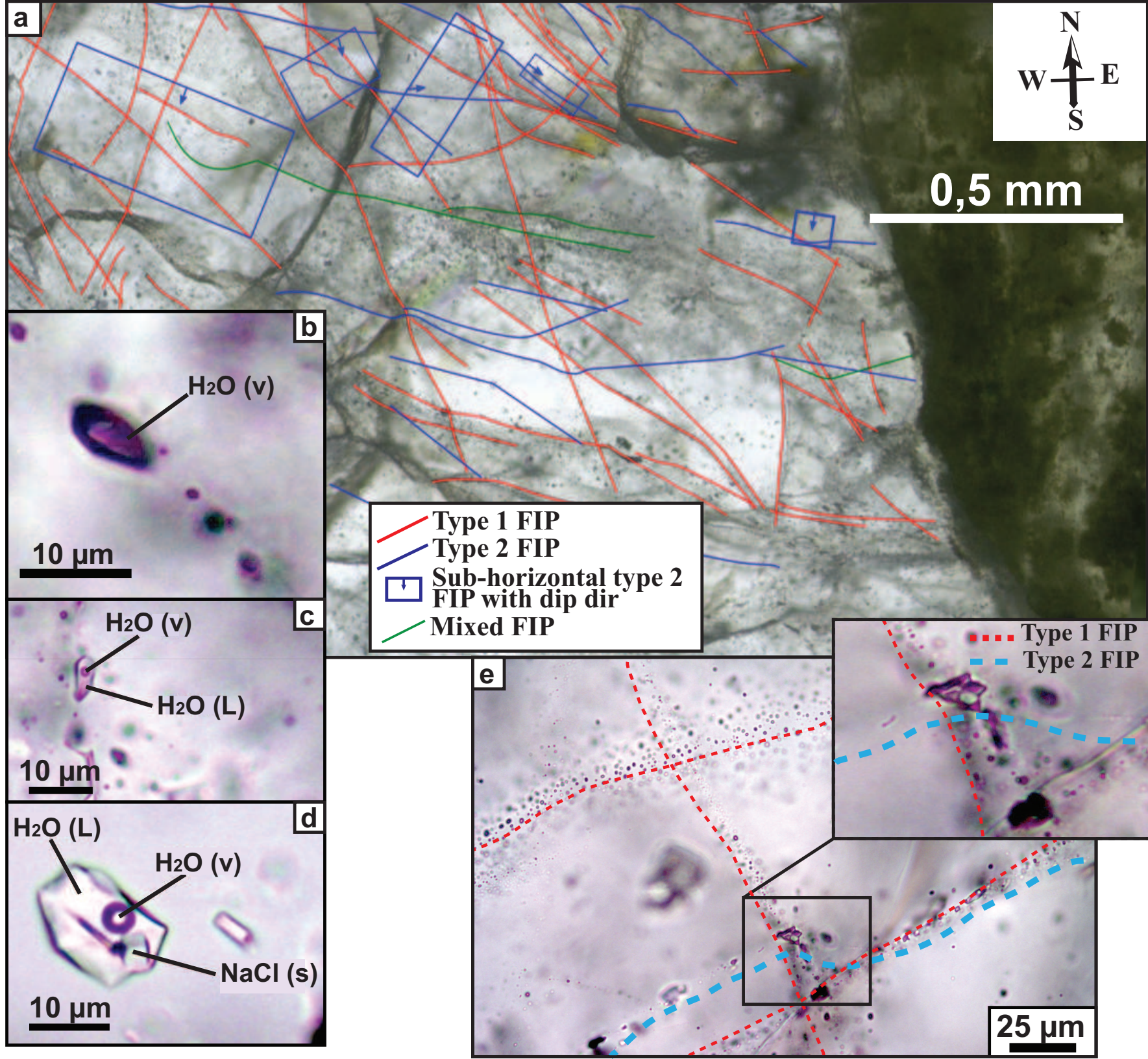


Figure 18



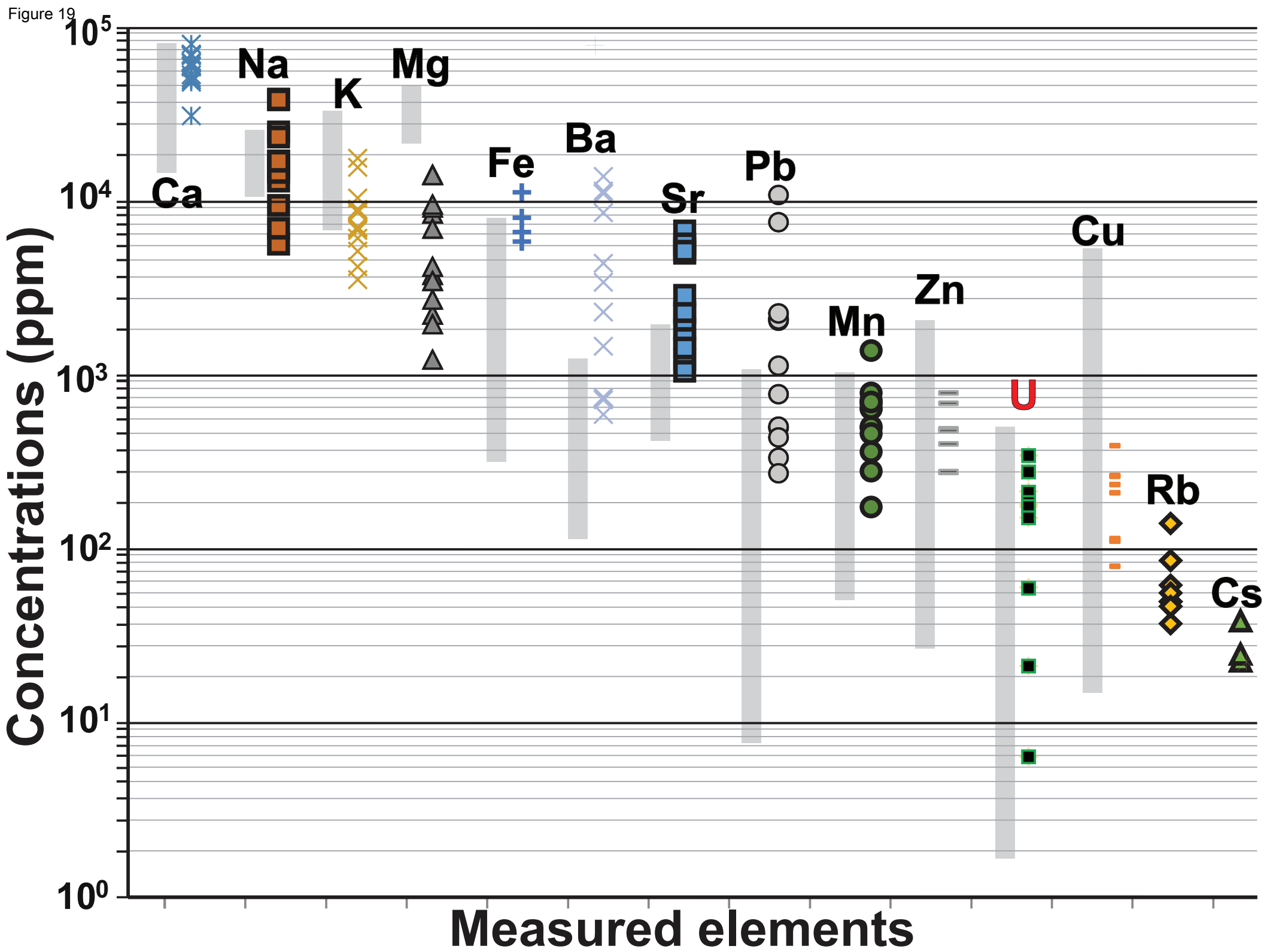


Figure 20

Type 1 FIPs

85W prospect

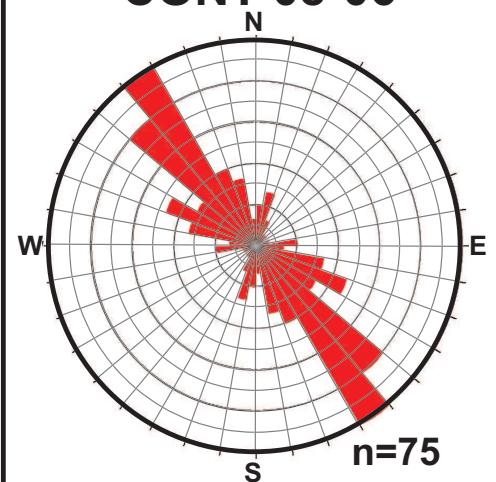
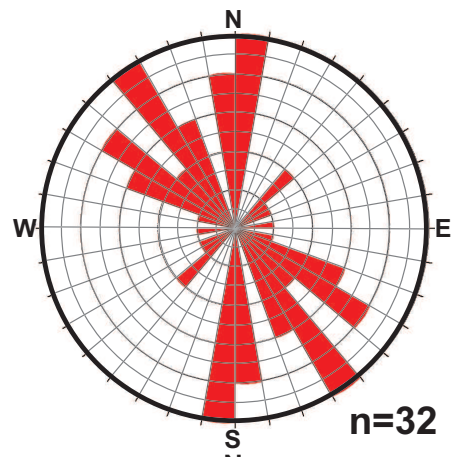
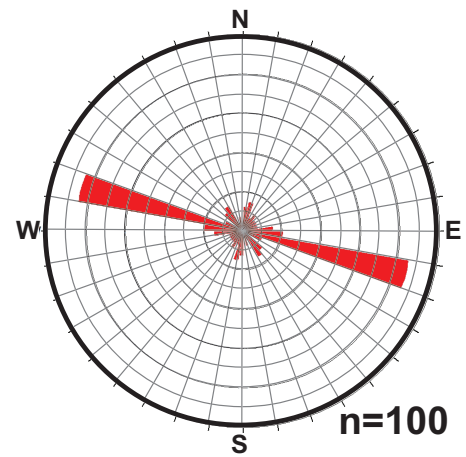
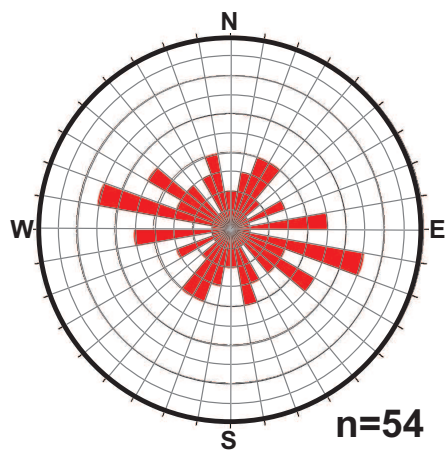
Contact prospect

85W-09-07

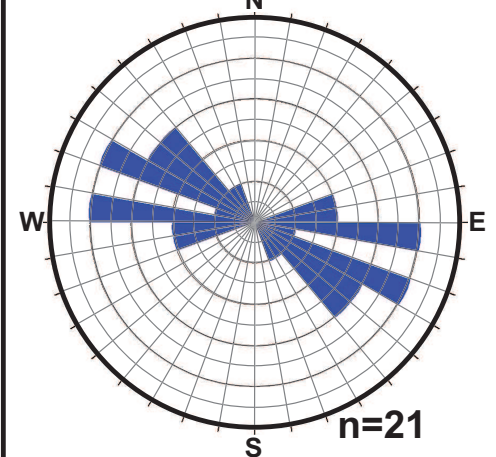
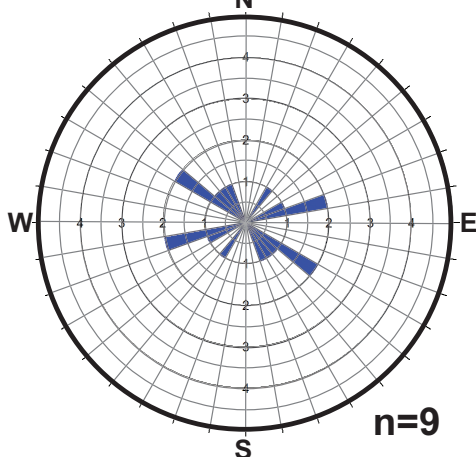
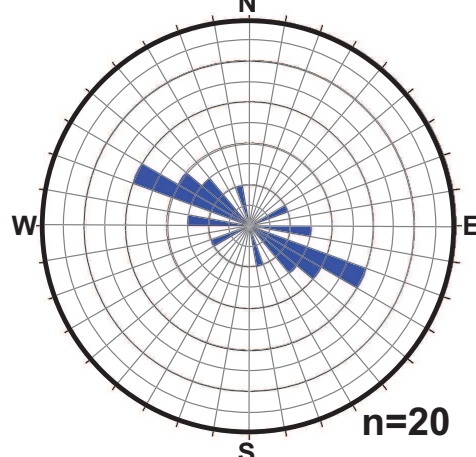
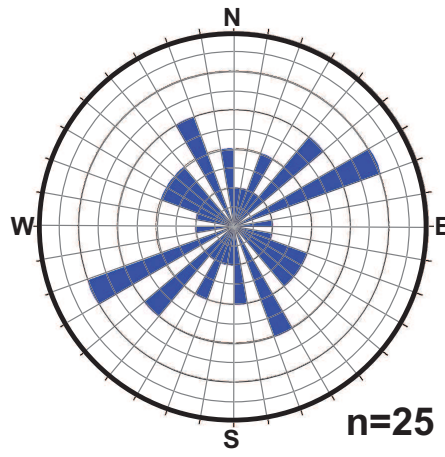
85W-09-04

85W-10-04B

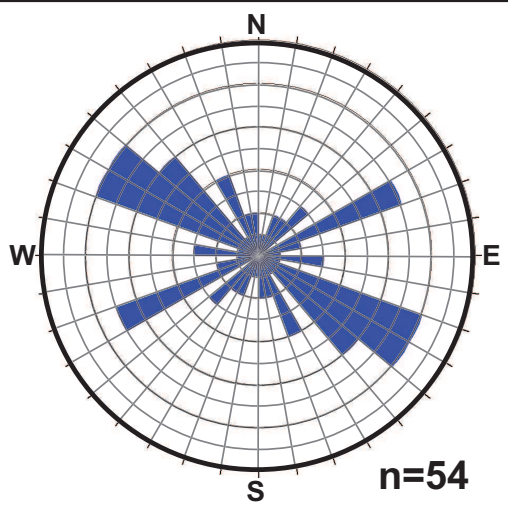
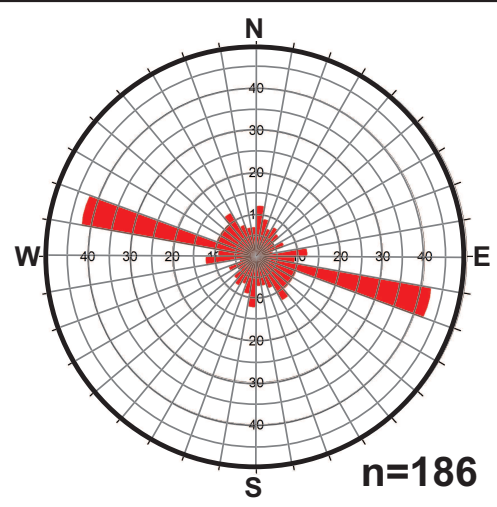
CONT-08-06



Type 2 FIPs



Combined measures for 85W



Gneiss foliation

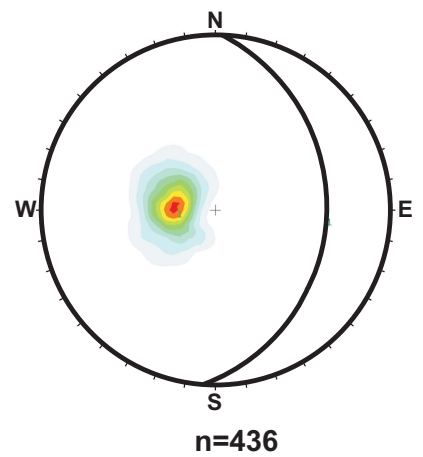


Figure 21

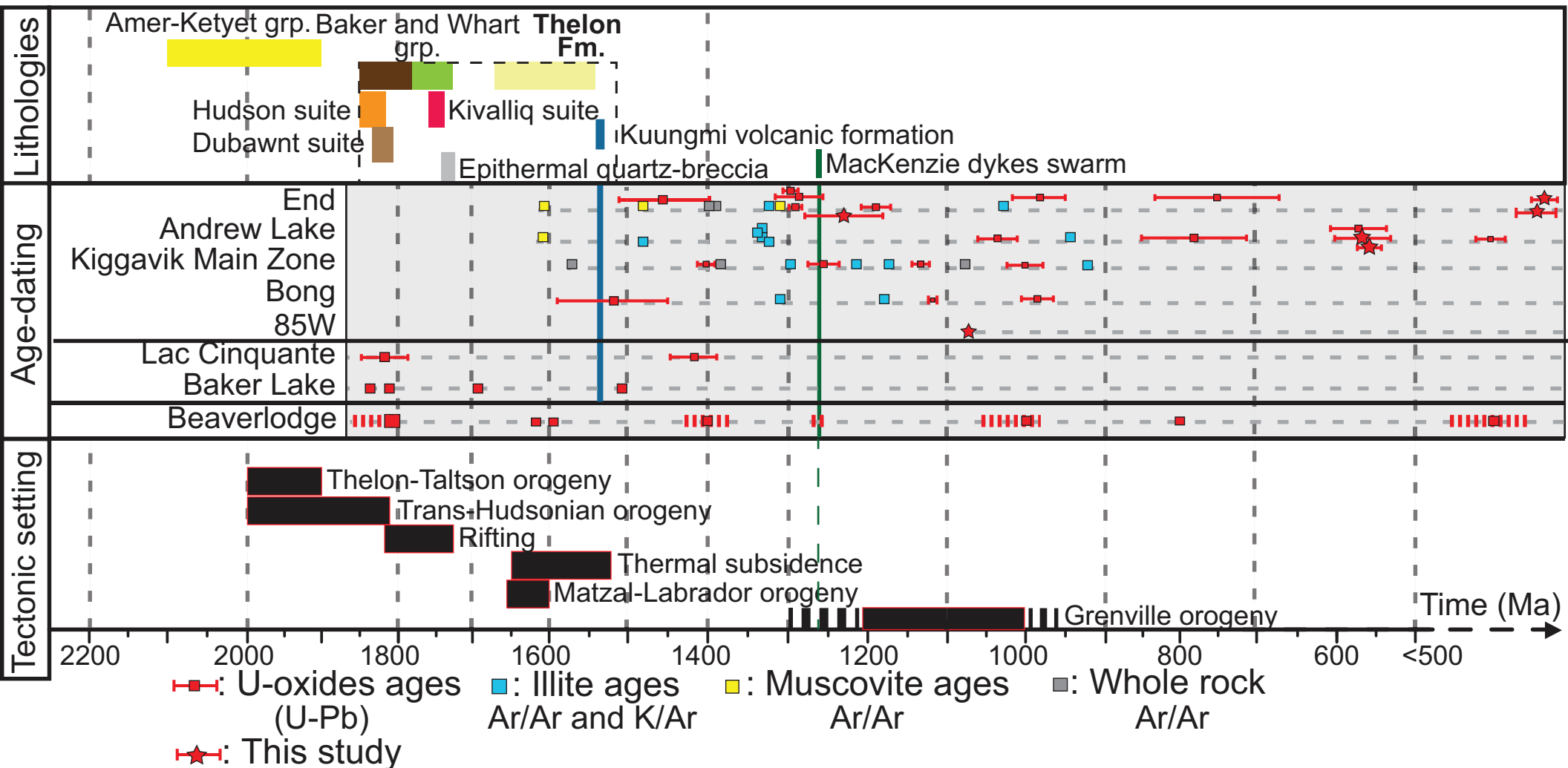


Figure 22

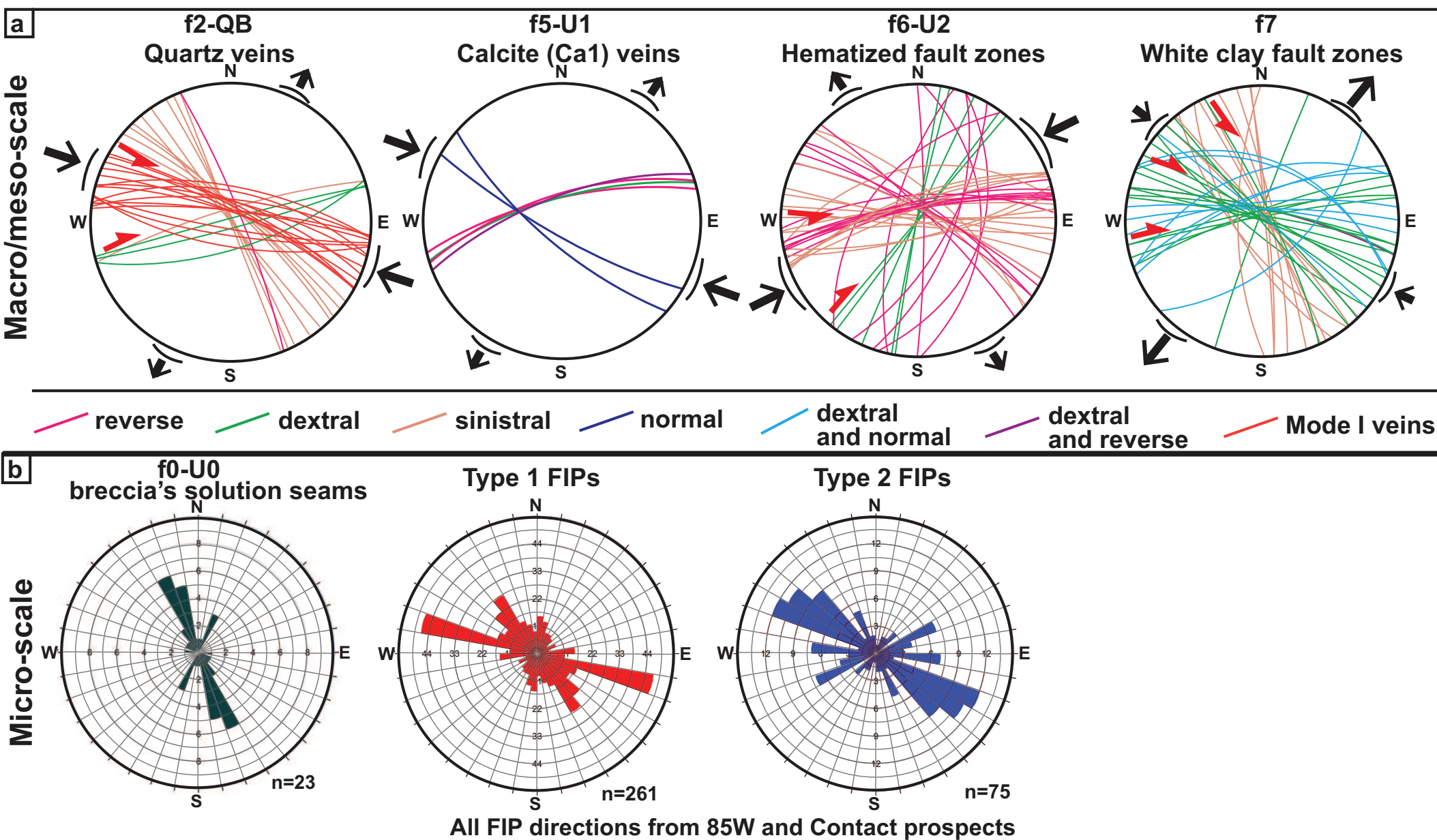
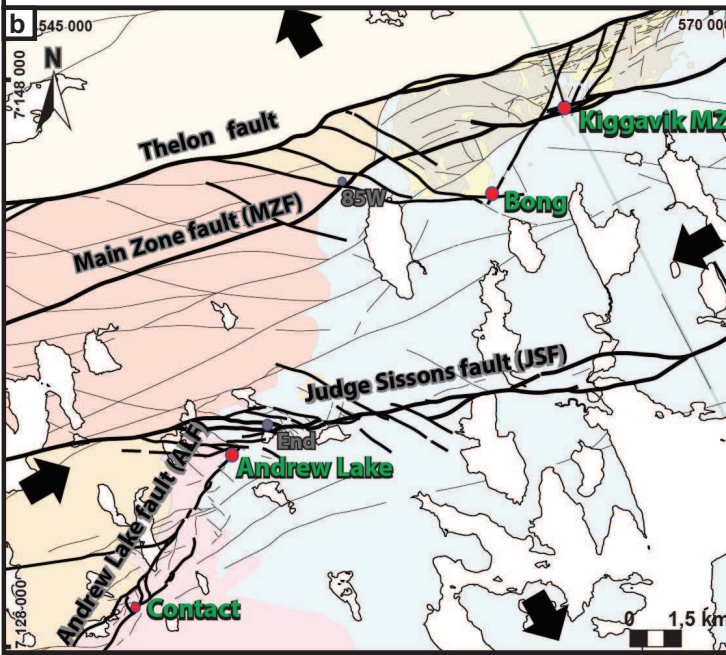
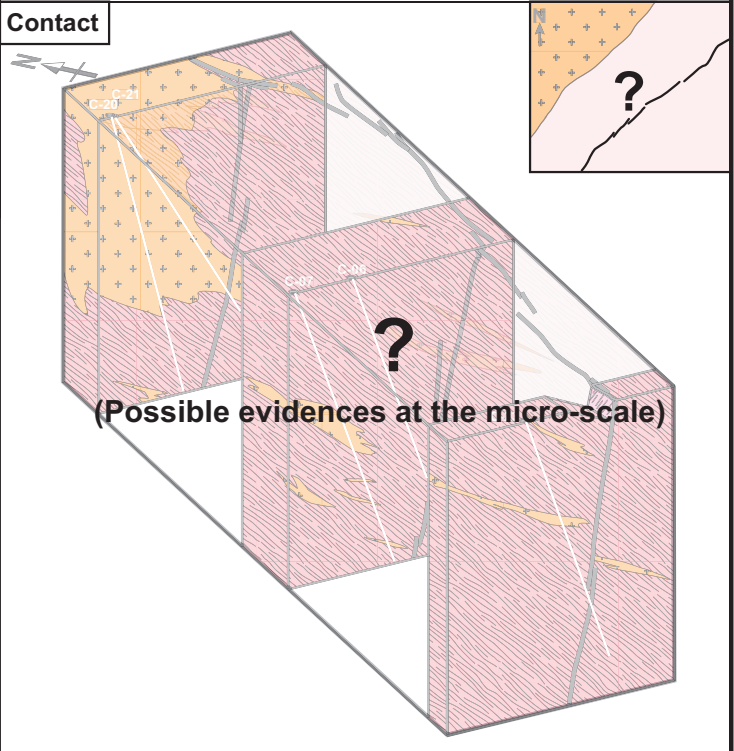
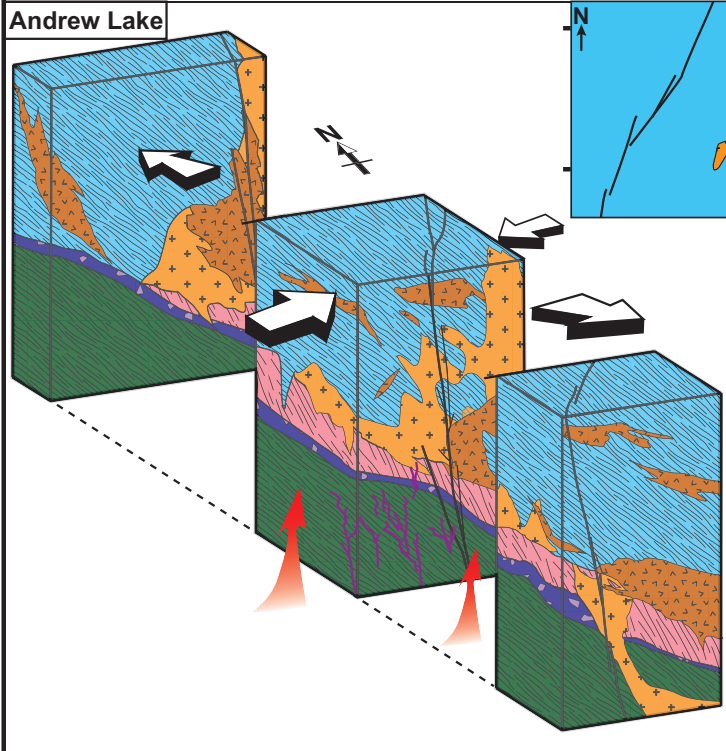
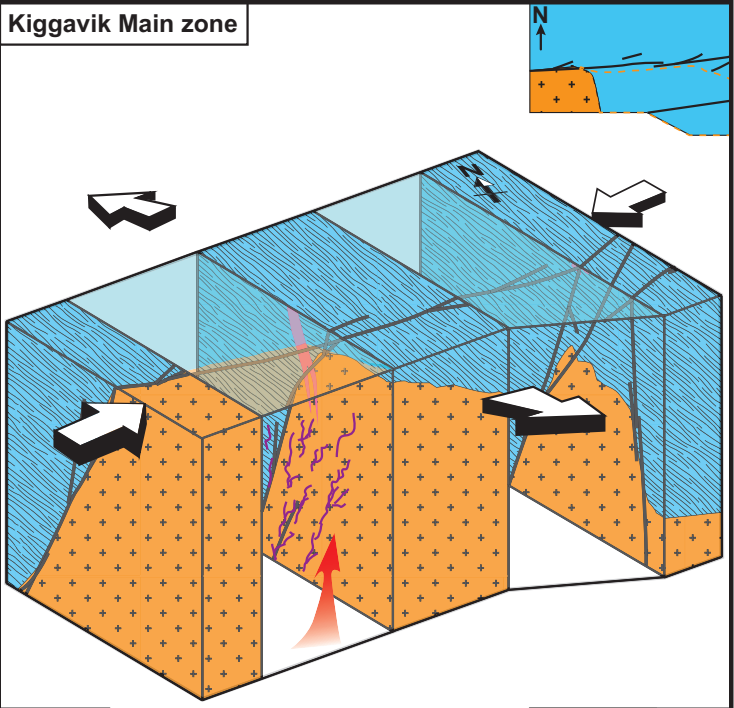
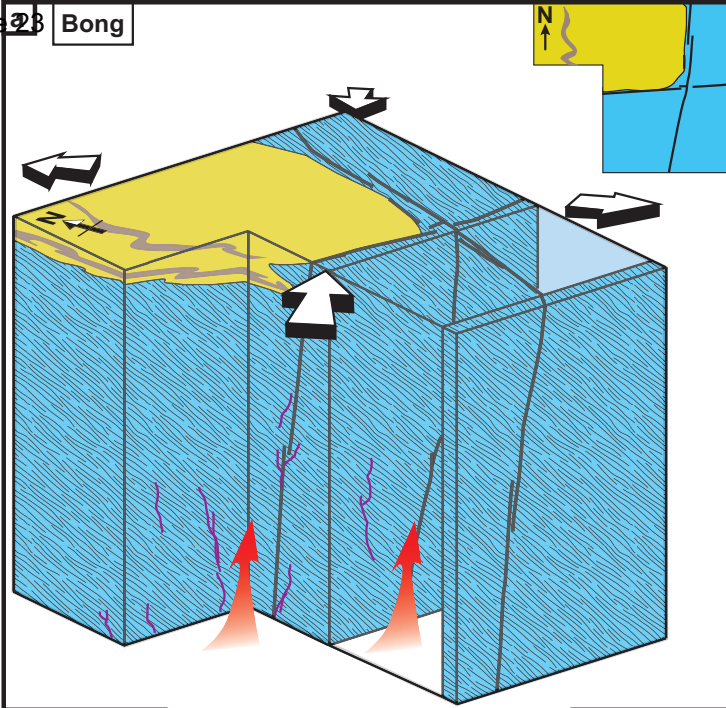


Figure 23 Bong



- Drillholes
 - Andrew Lake "basal breccia"
 - Woodburn Lake gneiss
 - Archean granitic/banded gneiss
 - Main faults pre QB
 - f0-U0
 - Nueltin granite
 - Syenite
 - Hudsonian granite
- ~N70 σ_1 , ~N150 σ_3
 - High temperature (>300 °C)
 - Link with magmatism of the Baker Lake Grp.
 - Pitchblende, brannerite (Th-rich), sulfides, rutiles, Fe-rich chlorite
 - weak to no clay alteration

Figure 24

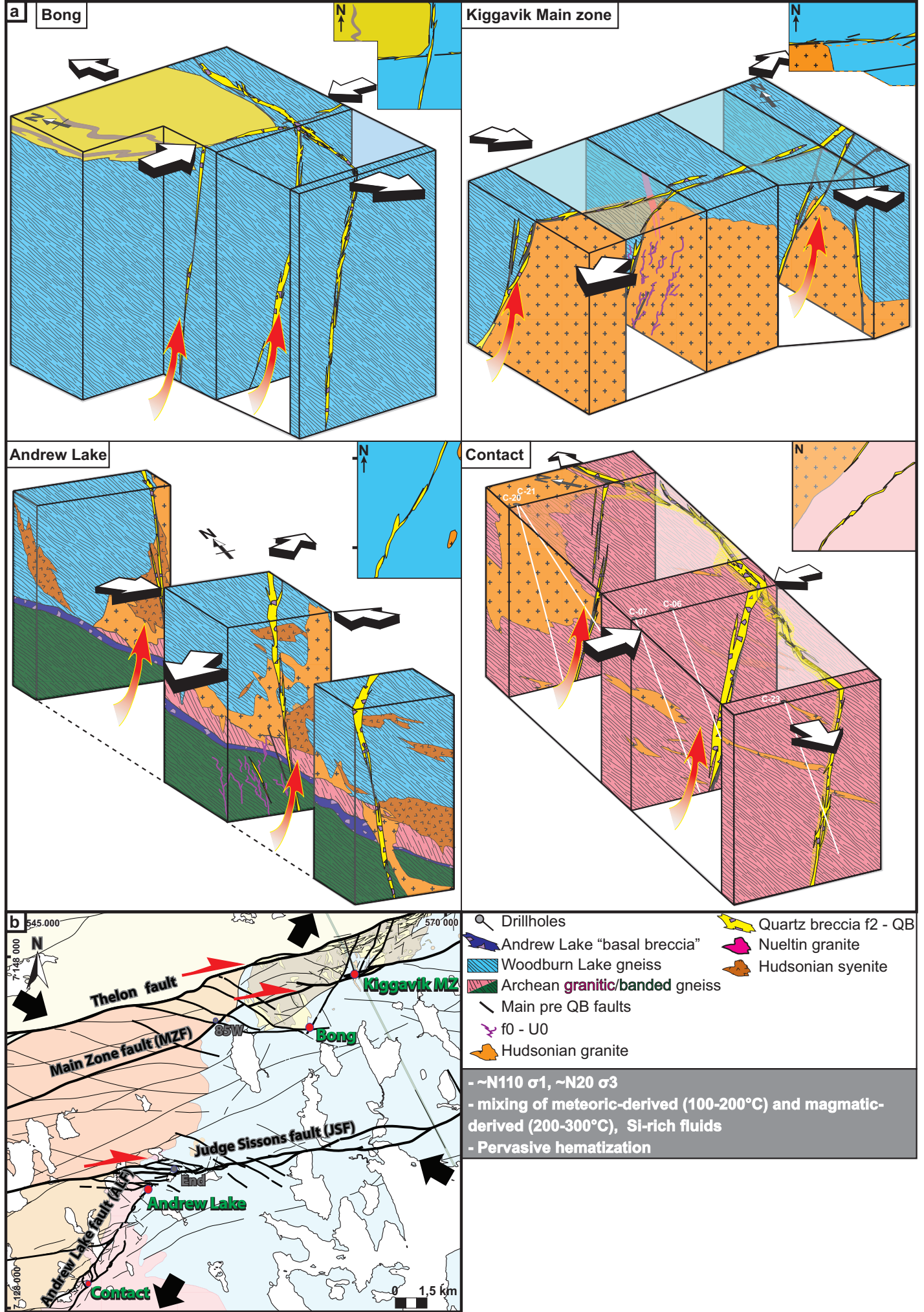


Figure 25

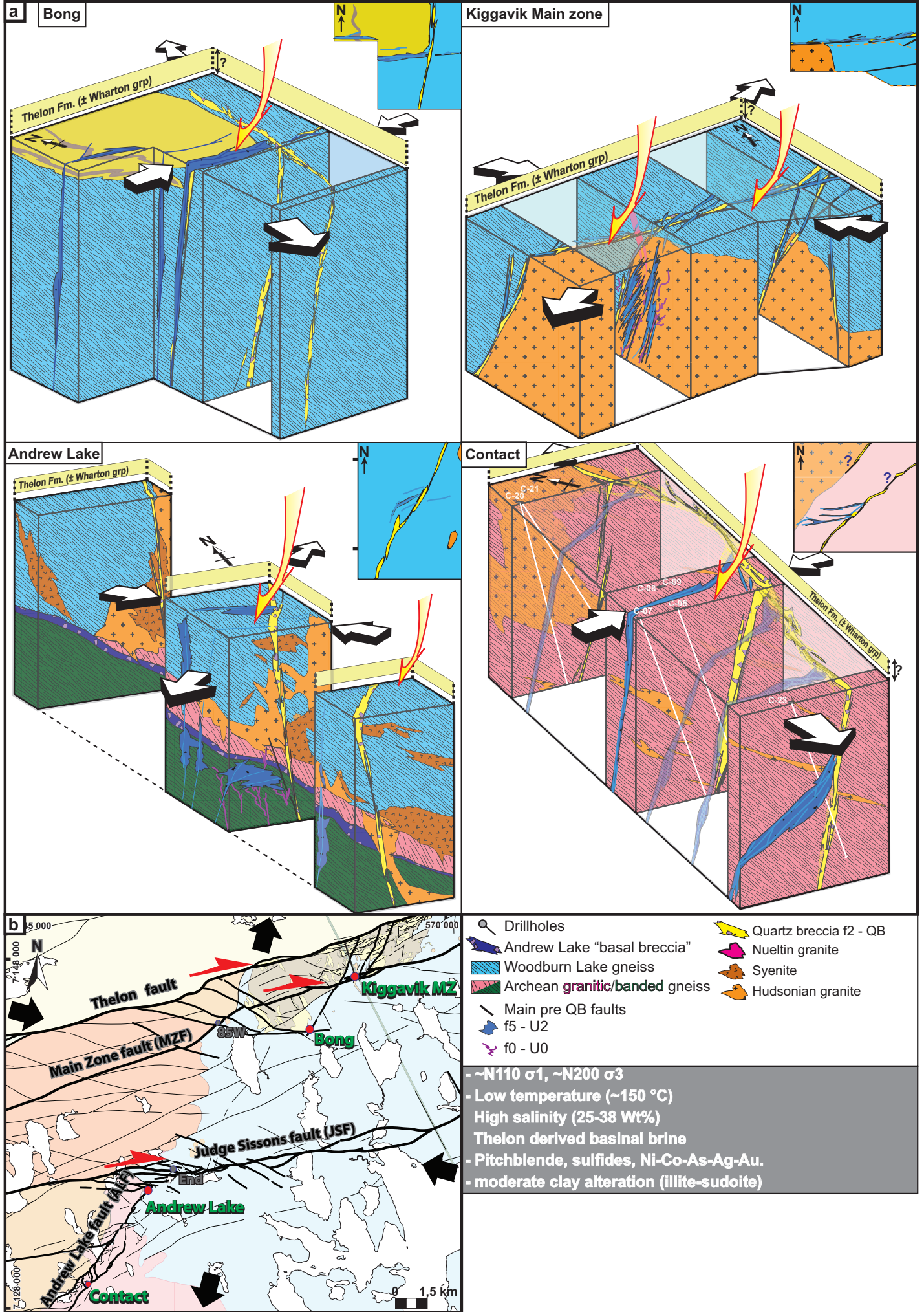


Figure 26

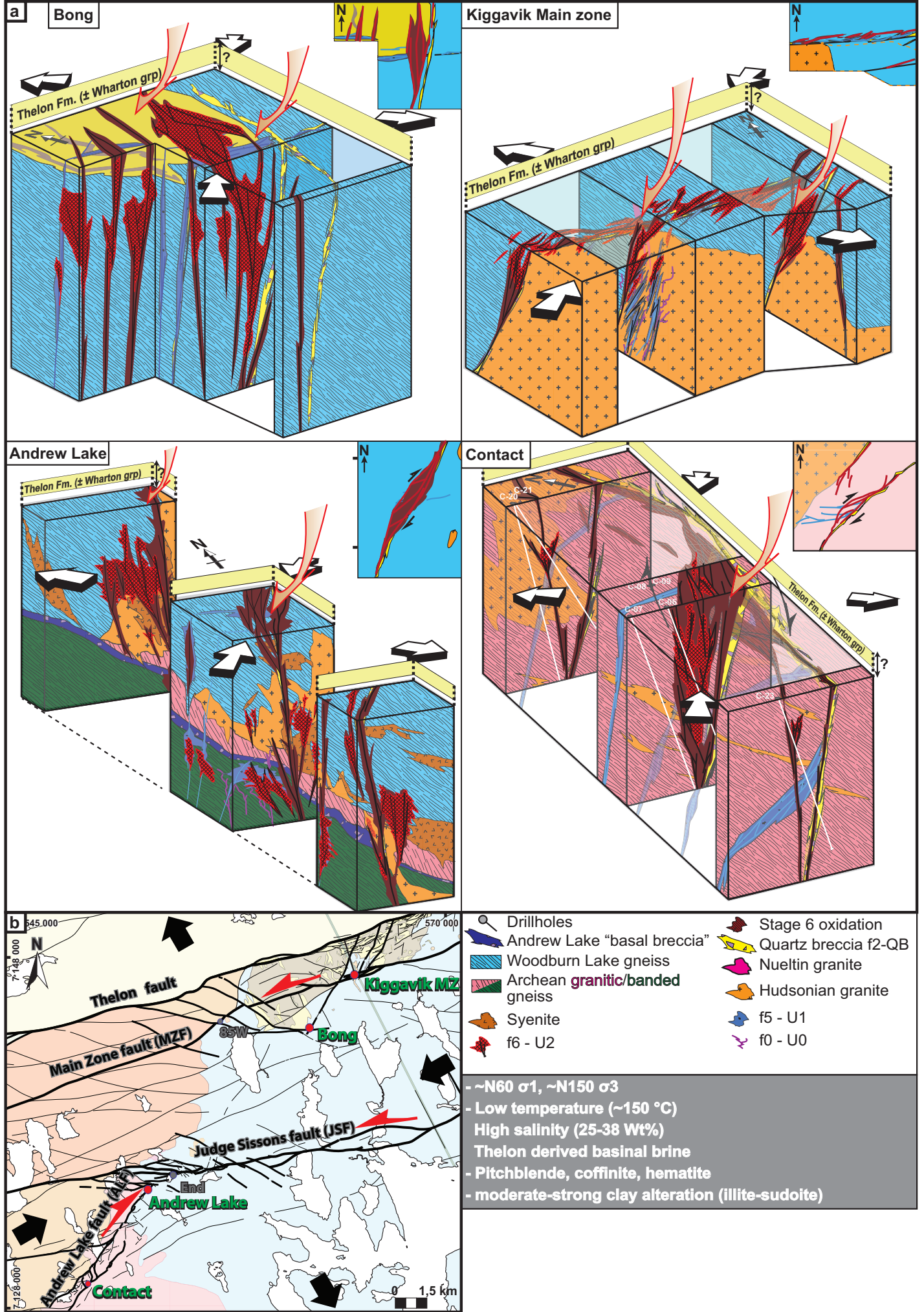
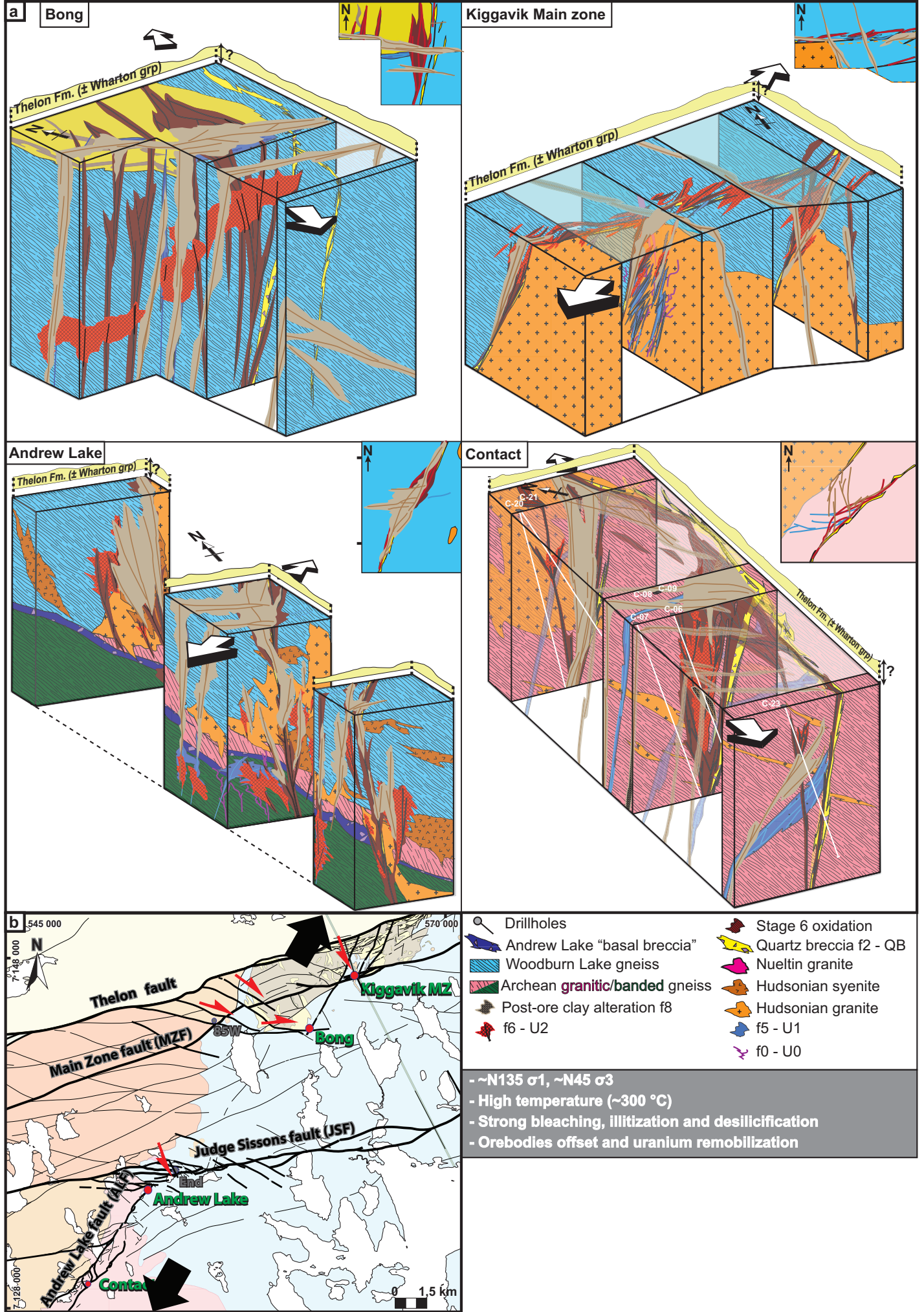
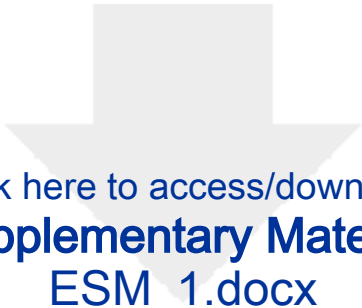



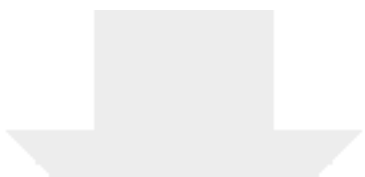
Figure 27





Click here to access/download
Supplementary Material
ESM_1.docx





Click here to access/download
Supplementary Material
ESM_2.docx

